学位論文

Supernova nucleosynthesis and chemical enrichment explored by X-ray observations of the hot gas in galaxies

(X線観測で探る銀河の超新星元素合成と化学進化)

2024年3月

福島 光太郎

DISSERTATION

Supernova nucleosynthesis and chemical enrichment explored by X-ray observations of the hot gas in galaxies

March 2024

Kotaro Fukushima

To my respected ones; while visible or invisible.

PREFACE

In the first part of this thesis, the author presents the results derived from a joint *Chandra* and *XMM-Newton* analysis with observational data, totalling over 500 kiloseconds, of the cool core within the Centaurus cluster (NGC 4696). This investigation uses CCD detectors to focus on the spatial distributions of several element abundances, including O, Mg, Si, S, Ar, Ca, Cr, Mn, Fe, and Ni. The N, O, Ne, Mg, Fe, and Ni distributions are also studied using the Reflection Grating Spectrometer (RGS). The observed trend indicates a significant decrease in the abundance within the central 18 arcsecond region although there are differences when using other detectors and atomic codes. The abundance ratios, including Ne/Fe with RGS, show uniform radial profiles. Here, challenges arise in accurately measuring absolute abundances in the innermost core, especially for the Fe-L lines, where discrepancies between the two latest atomic codes result in Fe abundance values of 0.5 and 1.4 solar, respectively. The results reveal potential systematic uncertainties in the atomic data and response matrices, which contribute at least partly to the observed abundance drop. Except for super-solar N/Fe and Ni/Fe, and sub-solar Ne/Fe and Mg/Fe, the abundance pattern is consistent with the solar composition, partially posing a challenge to current supernova nucleosynthesis models. The super-solar N/O and comparable Mg abundances to stellar metallicity profiles suggest the dominance of mass-loss winds in the gas enrichment around the brightest cluster galaxy. The solar Cr/Fe and Mn/Fe ratios imply substantial contributions from both near- and sub-Chandrasekhar mass explosions of Type Ia supernovae.

The second part of the dissertation focuses on analysing 14 early-type galaxies based on the *XMM-Newton* RGS spectroscopy. This chapter will extend the previous results with a larger sample. The extended sample includes some well-known brightest cluster galaxies, such as ones in the Perseus cluster (NGC 1275) and the Virgo cluster (M87). The study reveals the generally flat spatial variation of the O/Fe, Ne/Fe, and Mg/Fe ratios within the central 60 arcsecond regions of each object, regardless of whether a central Fe abundance drop has been reported previously. Typical flat

profiles between noble gas and normal metal elements indicate that the dust depletion process does not dominate these systems, raising the possibility that the observed abundance drops are due to factors such as systematic problems in atomic codes, for instance. This result is consistent with the situation in the Centaurus core described above. In particular, giant systems with high gas mass-to-luminosity ratios tend to exhibit hot gas (~ 2 keV) with the solar N/Fe, O/Fe, Ne/Fe, Mg/Fe, and Ni/Fe ratios. In contrast, less-massive systems at sub-kiloelectronvolt temperatures, such as isolated or group-centred galaxies, generally exhibit the super-solar N/Fe, Ni/Fe, Ne/O, and Mg/O ratios. A simply linear combination of the latest supernova nucleosynthesis models struggles to reproduce this super-solar abundance pattern.

The interstellar medium (ISM) in the starburst galaxy M82 will be studied in the third part. By measuring metal abundances in the ISM, one can study the chemical enrichment within the galaxy and the transport of metals into the ICM by powerful outflows. Spectral analysis of the X-ray emission from the M82 nucleus is carried out using the RGS to estimate metal abundances in the ISM accurately. Over 300 ks of RGS data observed at 14 position angles are analysed, setting a cross-dispersion width of 80 arcsec. Multi-temperature thermal plasma components are assumed to reproduce the observed spectra; each is in collisional ionization equilibrium (CIE) and subject to different spatial broadenings. The O VII band CCD image shows a broader distribution than the O VIII and Fe-L band ones. The O VIII line profiles show a prominent double-peaked structure, corresponding to the northward and southward outflows of M82. The O VII triplet feature shows marginal peaks and a single CIE component, convolved with the O VII band image, well explains the spectral shape. Likewise, the combination of a CIE model with a charge-exchange emission model also successfully reproduces the O VII line profiles. However, the ratio of these two components varies significantly with the position angles of each observation, which is physically unnatural. Spectral fitting of the broadband spectra suggests a multi-temperature phase in the ISM, approximated by three components at 0.1, 0.4, and 0.7 keV. In particular, the 0.1 keV component has a broader distribution than the 0.4 and 0.7 keV plasmas. The derived abundance pattern shows super-solar N/O, solar Ne/O and Mg/O, and half-solar Fe/O ratios. These results indicate that core-collapse supernovae efficiently enrich the starbursting core of M82.

Finally, the author revealed that the spatial distribution of noble gas Ne (and Ar) in early-type galaxies, including BCGs, aligns with standard metals, challenging the cold dust scenario often invoked based on the cooling-flow model. Abundance drops, if present, might result from active galactic nuclei feedback, removing central

metal-rich gas directly. The abundance ratios in M82 do not deviate significantly from supernova nucleosynthesis models, and there is little evidence supporting the effect of cold dust on these ratios. The observed abundance patterns in early-type galaxies and M82, reliable ratios not biased by cold dust effects, are compared to supernova nucleosynthesis models. The latest yields by supernovae can roughly reproduce solar abundance ratios of O/Fe, Ne/Fe, Mg/Fe, and Ni/Fe (with 20 per cent systematics) across different core-collapse supernova models. Different supernova nucleosynthesis models can determine the contribution fraction of both Type Ia and core-collapse supernova to chemical enrichment with at most 10 per cent differences. In addition, there is a suggestion for core-collapse supernovae that extremely massive progenitors might not explode.

Although the author is the last person that could be a monarch or a high official, first-person pronouns appear in the plural in most parts of this dissertation, excluding the unnumbered chapters. The spelling will follow the British style, adopting *-ize* for verbs that can be ended with either *-ize* or *-ise*.

Contents

List of Figures

List of Tables

Chapter 1

Introduction

Where did the numerous elements that are essential to human civilization come from? This is one of the most critical questions in modern physics. Theoretical studies in the last 100 years have shown that stars or supernovae synthesized these elements or metals in astronomical contexts. However, the explosion mechanisms of supernovae, the key players in the element synthetic process, especially the mass distribution of progenitor stars (parent stars of supernovae), remain elusive not only in Type Ia supernovae but also in core-collapse ones. For example, is the mass of a white dwarf that explodes as a Type Ia supernova close to the limit mass (known as Chandrasekhar mass, 1.4 times the solar mass), or not?; what is the progenitor mass range when a massive star directly collapses into a black hole without any explosions, and when it actually explodes as a core-collapse supernova? Many studies have estimated the progenitor mass of supernovae by X-ray observations of supernova remnants, i.e. X-ray-emitting gas containing supernova ejecta that remains after explosions. Unfortunately, little work has tried to calibrate their results: a severe situation as each researcher claims what they want to say. This is due to the large scatter in the individuality of each supernova remnant (shapes, ages, surrounding environments at the time of explosions, and so on), which makes systematic analysis of supernova remnants difficult.

In X-ray astronomy, it was discovered 50 years ago that galaxy clusters, the largest objects in the universe with megaparsec scales, are not only resided by visible stars but also filled with hot X-ray-emitting gas at tens of millions of kelvin. The X-ray spectra from such gas exhibit many characteristic emission lines of metals such as O, Si, and Fe, indicating that the hot gas contains a large amount of elements produced by stellar nucleosynthesis. Smaller systems than clusters, i.e. galaxies or groups of galaxies, also confine hot gas, which can be billions of years old. Since the hot gas retains many metals forged in supernovae, it is possible to calibrate the

supernova model roughly by comparing it with the observed elemental composition in the hot gas. For example, the mass distribution of white dwarfs to explode as Type Ia supernovae will be estimated by observing their remnants, as well as the hot gas in galaxies experiencing plenty of supernovae; thus, the two observational results can be cross-calibrated. Since Type Ia supernovae have white dwarfs as their origins, which takes hundreds of millions of years or more to be generated, the hot gas with a long evolutionary history, such as the atmosphere in early-type galaxies or brightest cluster galaxies, are suitable targets for this study. Indeed, gases with a long history must also contain information on core-collapse supernovae immediately after the star-formation epoch about 9 Gyr ago, where products like O, Ne, and Mg may now be trapped in less massive stars. A better approach to investigating these light metals directly synthesized and ejected by supernovae is observing the hot gas in starburst galaxies, generating many young stars quickly. Therefore, in this thesis, the element abundances (can be roughly described as chemical composition) are measured from X-ray observations of the hot gas in central regions of galaxies; then, supernova nucleosynthesis models will be evaluated by comparing them with the observed abundance patterns. The target objects are early-type galaxies, including cluster and group central gaalxies, for a study of the Type Ia supernovae and starburst galaxies for core-collapse ones. Then, another important question is whether the hot gases in these galaxies, they vary remarkably in their own shape and the age of member stars, have similar abundances to those observed in our Milky Way?

There are some concerns regarding the measurement of metal abundances of early-type galaxy centres. The hot gas in luminous early-type galaxy centres, such as cluster centres, was expected to become cool rapidly due to efficient X-ray emission, causing a cooling of the central region (known as the cooling-flow model). Note strongly that such enormous cooling has not been found in most early-type galaxies with very few exceptions, as reviewed in Chapter 2. Meanwhile, in some early-type galaxies, a decrease in element abundances, especially of Fe, towards the centre has been reported. It has been argued that this abundance drop is due to some elements being depleted onto cold interstellar dust, whose picture would fit well the cooling-flow model. If this dust scenario is correct, noble gas elements like Ne and Ar with low chemical reactivity would be less likely to be incorporated into the dust grains, leading to a different abundance than other normal metals, such as O and Fe. Herein, the observed abundance ratios must be biased, making the estimate of nucleosynthesis models harder. A similar process may bias the O, Ne, and Mg estimation in starburst galaxies wherein there are many cold matters triggering star formation. In Chapters 3

and 4, the X-ray bright Centaurus cluster centre (NGC 4696) and some early-type galaxies are analysed, whose spatial distribution of Ne (and to some extent Ar) will be used to put a question on the dust grains scenario. Then, reliable abundance ratios are obtained in the hot gases within these systems. In Chapter 5, the hot gas abundances are measured in a prototype starburst galaxy M82. Finally, in Chapter 6, the obtained abundance patterns will be compared with the chemical composition of our Milky Way galaxy. In addition, some supernova nucleosynthesis models, as well as their predictions about yields and progenitor masses, will be estimated by comparing the abundance ratios of early-type and starburst galaxies.

Chapter 2

Short Review for X-ray Studies on Matters in Hot Gases

This chapter briefly reviews the research history, physics, and observational instruments to help readers comprehend this thesis. At the beginning of each subsequent chapter, an introduction more specific to the contents of the same chapter will be provided.

2.1 Chemical Enrichment of the Universe

2.1.1 Early history

Our species has only revealed in recent decades the origin of the chemical elements and the history of their production, i.e. the chemical enrichment in the universe. After the basis of quantum mechanics had been established in the 1920s, Hans Bethe set the nucleosynthesis theories in stars: what is known today as the He production by the p-p chain and CNO cycle reactions (Bethe 1939). For heavier elements, two milestones are worth mentioning. One is the prediction of triple-α reaction — the C production from He — by Fred Hoyle (Hoyle 1946). Another is what is called the "$\alpha\beta\gamma$ paper" that correctly anticipates cosmic abundances in the early universe (Alpher, Bethe & Gamow 1948, a part of Ralph Alpher's PhD dissertation!). Following these works, Burbidge et al. (1957) completed the modern stellar nucleosynthesis theory. Namely, the Big Bang nucleosynthesis in a few tens of seconds after the creation of the universe produces H, He, and a few Li and Be. Most of the heavier metals ubiquitous in the present-day universe — such as O, Si, Ca, and Fe, which are matters that make up our bodies and/or resources indispensable for civilized lives — are forged in stellar cores and supernova explosions. Here, supernovae must be responsible not only

for producing metals but also for enriching interstellar space. The current standard enrichment models (e.g., Arnett et al. 1989; Nomoto et al. 2013) inherit almost the same philosophy of Burbidge et al. (1957).

2.1.2 Supernova nucleosynthesis

Supernova explosions occur at the end of stellar evolution through which stars die a spectacular death. A brief note of stellar evolution is as follows. Stars support their mass with the energy produced by internal nuclear fusion reactions, most of which are the He production from H-burning in the main-sequence phase as our sun. The produced He core at the centre of the main-sequence star contracts as it gains mass, and the outer layers expand as the temperature rises, where stars enter a phase known as the red giant branch. For example, a star with 1 and 15 $M_\odot$ [1] of mass spends ~ 11 Gyr and ~ 11 Myr on H-burning, respectively (Woosley et al. 2002); thus, it would take billions of years for our sun to reach this stage. The He-burning process generates the C and O nuclides in red giants. Then, subsequent evolution diverges according to stellar mass.

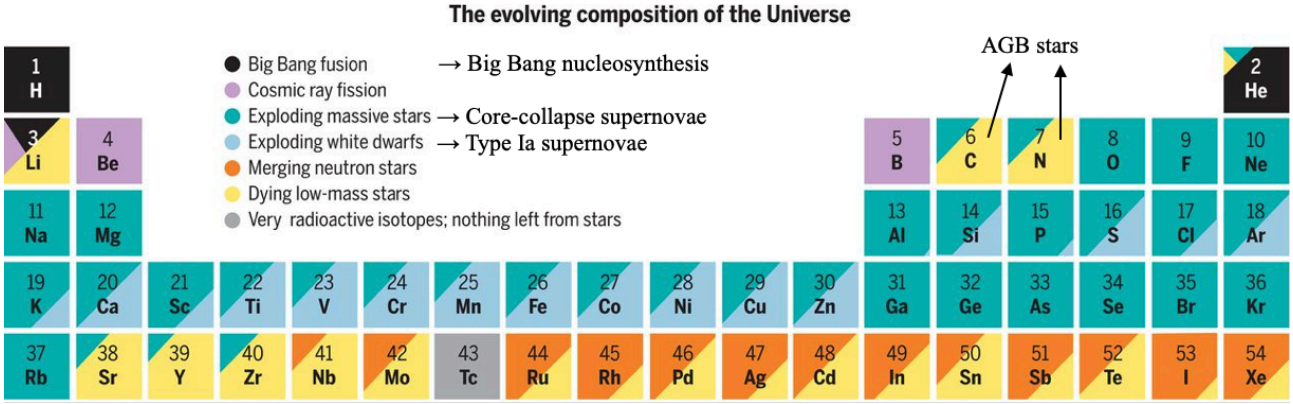

Figure 1: Origins of elements in our solar system. Colours on each element panel show the relative contribution of nucleosynthesis sources. This figure is retrieved from Johnson (2019); however, information on elements heavier than Xe is thinned out. Comments are added to three synthetic origins relating to this work the most.

Type Ia supernovae

After low-mass stars $\lesssim 8\,M_\odot$ exhaust fuel H and He taking over 100 Myr, a white dwarf comprising C and O is formed that is one of the compact objects supported by electron degeneracy pressure (Shapiro & Teukolsky 1983, a classical but comprehensive

[1] In astronomy, the solar mass ($\sim 2 \times 10^{33}$ g) is denoted by $M_\odot$. The common use of $\odot$ in present science writings is a rare case wherein obsolete astrological symbols appear.

textbook). What is important in the context of this thesis is that white dwarfs potentially lead to thermonuclear explosions, namely, Type Ia supernovae (SNe Ia). Standard models propose two mechanisms for such explosions. One insists that a white dwarf undergoing mass accretion from its companion star reaches a limit mass, i.e. Chandrasekhar mass ($M_{\rm Ch}$ $\sim 1.4\,{\rm M}_{\odot}$), and then, starts nuclear burning (e.g., Whelan & Iben 1973, near-$M_{\rm Ch}$ explosion). A merger of white dwarfs also causes SNe Ia, for instance, where each exploding white dwarf can be lighter than $M_{\rm Ch}$ (e.g. Webbink 1984, sub-$M_{\rm Ch}$ explosion) [2]. As mentioned above, white dwarfs are mainly composed of C and O; thus, these elements are used as fuel for the α process forging α-elements like Si, S, Ar, and Ca, as well as Fe-peak elements such as Cr, Fe, Mn, and Ni (Fig. 1). Importantly, a single SNe Ia generates $\sim 0.6\,{\rm M}_{\odot}$ of Fe for both mechanisms, which are the main source of Fe in the universe (e.g., Reddy et al. 2006; Sato et al. 2007). Additionally, in the case of near-$M_{\rm Ch}$, the core of exploding white dwarfs becomes denser ($\sim 10^9\,{\rm g\,cm^{-3}}$, e.g., Leung & Nomoto 2018) and achieves a neutronized environment in which the electron capture process (EC, $\rm p + e \rightarrow n$) can occur (e.g., Seitenzahl et al. 2013b; Blondin et al. 2022). Therein, neutron-rich isotopes decay into stable Fe-peak elements; for example, $^{55}{\rm Co} \xrightarrow{\rm EC} {}^{55}{\rm Fe} \xrightarrow{\rm EC} {}^{55}{\rm Mn}$ and $^{56}{\rm Ni} \xrightarrow{\rm +p} {}^{57}{\rm Cu} \xrightarrow{\rm EC} {}^{57}{\rm Ni} \xrightarrow{\rm EC} {}^{57}{\rm Co} \xrightarrow{\rm +p} {}^{58}{\rm Ni}$. Consequently, the Mn and Ni enhancement would be a powerful probe for distinguishing the sub- and near-$M_{\rm Ch}$ progenitors of SNe Ia.

In Fig. 2(a), the classical and latest predicted yields are provided for SN Ia nucleosynthesis models. The Mn and Ni production is significantly affected by progenitor masses and core density. Here, it should be noted that it is difficult to distinguish between the progenitor masses of SNe Ia from optical observations, whatever the companion star of a white dwarf. The luminosity curves and maximum luminosities of SNe Ia obtained from optical observations are uniform [3], where both progenitor mass models can reproduce these optical properties. This means that the most direct limit on the progenitor mass problem of SNe Ia is to determine the abundances of the Fe-peak elements by X-ray observations.

[2] In reality, it is a little more complicated as there is no one-to-one correspondence between the companion star of a white dwarf (white dwarf or star) and the mass of the exploding white dwarf.

[3] This characterless of SNe Ia makes them a standard candle of the universe.

Core-collapse supernovae

Massive stars $> 8\,M_\odot$ finish the H- and He-burning process in < 15 Myr. Thenceforce, the stellar core continues to forge metals along the α process (e.g., Burbidge et al. 1957): $^{16}O \rightarrow {}^{20}Ne \rightarrow {}^{24}Mg \rightarrow {}^{28}Si \rightarrow {}^{32}S \rightarrow {}^{36}Ar \rightarrow {}^{40}Ca \rightarrow {}^{44}Ti \rightarrow {}^{48}Cr \rightarrow {}^{52}Fe \rightarrow {}^{56}Ni$ (decays to ^{56}Fe soon). Notably, the time taken for each burning phase becomes shorter and shorter; for example, Ne-burning and Si-burning will last for 0.7 yr and 18 day in a $15\,M_\odot$ star (Woosley et al. 2002). A small amount of odd-numbered elements can also be produced via H-burning on α-elements and He-burning on products of previous burning (e.g., Burbidge et al. 1957). Since the binding energy of ^{56}Ni is greater than of ^{60}Zn, the nucleosynthesis chain in massive stars ends when an ^{56}Fe core is formed in the centre of the star. After stellar nuclear reactions are extinguished, the core pressure that has supported gravity drops rapidly, leading to a gravitational collapse of stars and a mass falling to the centre. The collapse stops when a proto-neutron star is formed at the centre; then, a shock wave generated on the surface of a proto-neutron star blows the entire star away, that is a core-collapse supernova (CCSN, e.g., Burrows & Vartanyan 2021, for a recent review). Typically, one CCSN explosion releases 10^{51} erg of energy [4], comparable to the total energy given by our sunlight over ten billion years. The central core of progenitors collapses into a neutron star or black hole. By such a splendid demise of stars, the light α-elements (O, Ne, and Mg) and the intermediate-mass α-elements (Si, S, Ar, and Ca) are strewed over interstellar space (Figs. 1 and 2(b)).

Figure 2 depicts that the prediction of O, Ne, and Mg yields would be indeterminate, which is possibly caused by uncertainties of the reaction rate in the O production from C. In metal enrichment models of the hot interstellar gas (see subsequent sections), astronomers usually assume that massive stars $> 30\,M_\odot$ (sometimes up to $120\,M_\odot$) can explode as CCSN. Here is an issue that the observational evidence for the presence of very massive CCSN progenitors is lacking so far (Smartt 2015, for a review). Massive stars with $\gtrsim 20\,M_\odot$ might cause a faint explosion supplying a small amount of metals or directly collapse into a black hole without a SN (Nomoto et al. 2013).

2.1.3 Other channels of nucleosynthesis

Metals have synthetic sources other than supernovae (see Fig. 1); for example, merging neutron stars and mass-loss winds from low-mass stars. Merging events in neutron

[4] A unit of energy 10^{51} erg is sometimes referred to as Bethe named after Hans Bethe.

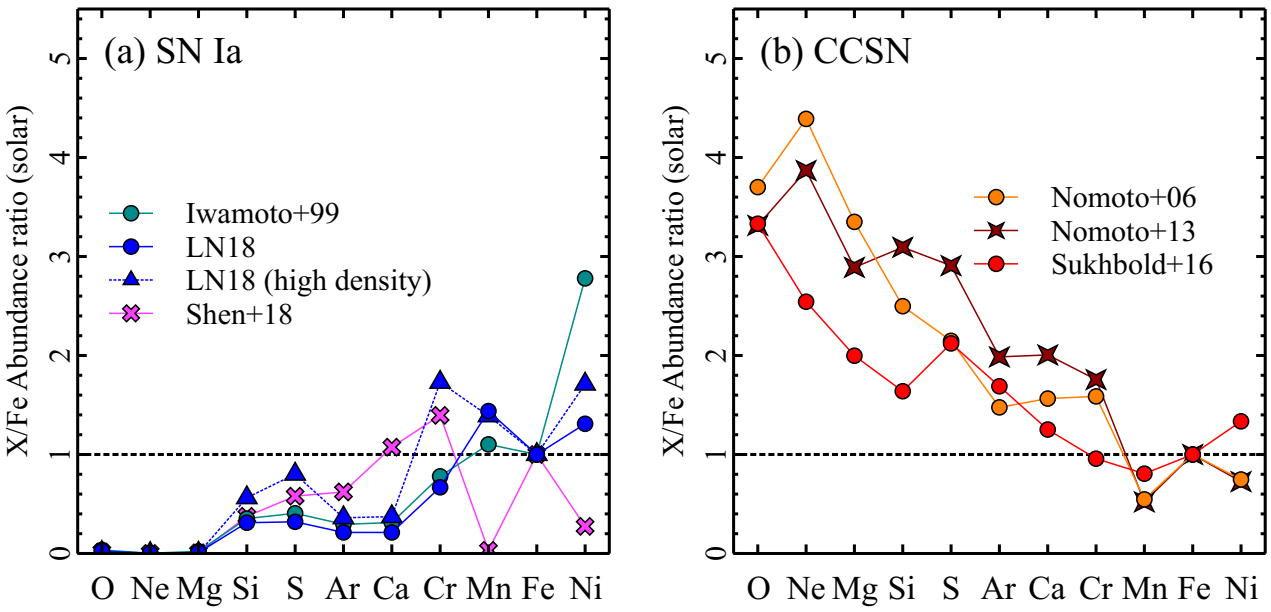

Figure 2: Predicted abundance ratio patterns (see the next section for details) for O/Fe, Ne/Fe, Mg/Fe, Si/Fe, S/Fe, Ar/Fe, Ca/Fe, Cr/Fe, Mn/Fe, and Ni/Fe of (a) SN Ia and (b) CCSN. (a) SN Ia models are from classical calculation of Iwamoto et al. (1999), normal and extremely high-density option of Leung & Nomoto (2018) for near-$M_{\rm Ch}$ progenitors; and from Shen et al. (2018) for sub-$M_{\rm Ch}$ progenitors. (b) CCSN yield calculations are taken from Nomoto et al. (2006), Nomoto et al. (2013), and Sukhbold et al. (2016), assuming solar metallicity progenitors. The initial mass function of Salpeter (1955) is used to integrate each yield with a certain progenitor mass (see the subsequent section).

star binary lead to the rapid neutron capture process (r-process) producing weighty elements such as Pt and Au, which is confirmed observationally in the 2017 event of GW170817 (Abbott et al. 2017; Chornock et al. 2017). A more critical channel in the context of this thesis is the contribution from less massive stars ~ 0.8–$8\,{\rm M}_\odot$. Such low-mass stars will experience the asymptotic giant branch (AGB) phase immediately before forming white dwarfs, which are also referred to as dying low-mass stars (Fig. 1). In the AGB phase, there is latitudinal convection in the outer star layers, transferring unburned elements from the core into the He-burning shell. Then, the proton capture reaction produces light elements [5] like Li and N (e.g., Karakas & Lattanzio 2014). Stars in the AGB phase usually eject their upper atmosphere by stronger stellar winds 10^{-8}–$10^{-5}\,{\rm M}_\odot\,{\rm yr}^{-1}$ (Höfner & Olofsson 2018) than does the sun ($10^{-14}\,{\rm M}_\odot\,{\rm yr}^{-1}$, e.g., Mishra et al. 2019). Thus, AGB stars supply light elements into interstellar space via mass-loss winds.

[5]The slow neutron capture process (s-process) can also occur in the atmosphere of AGB stars and supply some heavy elements (Käppeler et al. 2011, and see Fig. 1).

2.2 Galaxies and Clusters

2.2.1 Overview; as a cosmic scale reservoir of elements

Galaxies are celestial bodies composed of many stars, multi-temperature gases, dust, and dark matter, where there are about 2×10^{12} galaxies in the universe (e.g., Conselice et al. 2016). Two types of galaxies are presented here: spiral galaxies and early-type galaxies. A spiral galaxy has a clearly structured disc and a spiral arm thereon; for example, our Milky Way and the well-known neighbour M31 are classified as spiral galaxies. Ongoing star formation is exhibited in spiral galaxies ($\sim 2\,M_\odot\,yr^{-1}$ in our Milky Way, e.g., Licquia & Newman 2015). Some irregular examples like M82 or NGC 253 have more enhanced star formation at their centre, called starburst galaxies ($\sim$ 10–100 $M_\odot\,yr^{-1}$, e.g., Zhang 2018; Orlitova 2020). In contrast, early-type galaxies such as NGC 4636 and M87 show the elliptical distribution of stars and are generally characterized by a high proportion of old stars. An essential property of elliptical galaxies is the lack of cold interstellar matter, resulting in a low present star formation rate therein. Both types of galaxies confine hot X-ray-emitting interstellar medium (ISM). As noted in the previous section, metals produced by stellar or supernova nucleosynthesis are dispersed into the ISM via stellar mass-loss or supernovae (Mernier et al. 2018a; Werner & Mernier 2020). The elements supplied to the atmospheric gas of galaxies are confirmed by many X-ray observations (see subsequent sections for more detail).

Clusters of galaxies are the largest structures that are gravitationally bounded. The scale of clusters is over several Mpc across, and their mass is typically $\sim 10^{15}\,M_\odot$ (Sarazin 1988). The bulk of the cluster mass is accounted for by dark matter. The rest of the mass is from stars and hot gases with $\gtrsim 2$ keV (intracluster medium, ICM), where the stellar contribution is minimal compared to the cluster gas. Clusters of galaxies take 10 Gyr to assemble (Sarazin 1988). Galaxies belonging to clusters are mainly early-type galaxies such as NGC 4636 wherein old stars are resident with few present star formations. Metal transport and dissipation processes from the ISM to the ICM owe to, for example, relativistic jets engined by a supermassive black hole at cluster centres (Werner et al. 2019, for a review). Such an ejection process will disperse large amounts of metals in the central gas towards the outer region from kiloparsec to megaparsec scales (e.g., Simionescu et al. 2008; Kirkpatrick & McNamara 2015).

Other paths linking the ISM and the ICM are superbubbles and galactic winds,

more popular in spiral galaxies. A superbubble in our Milky Way can be formed around some star-forming regions, including a lot of massive stars, and shows diffuse X-ray emission (e.g., M17, Hyodo et al. 2008; Carina Nebula, Ezoe et al. 2019). In superbubbles, clustered CCSNe from massive stars boost the bubble expansion efficiently; then, bubbles blow out of the galactic disc as a galactic fountain, transporting interior metals into the circumgalactic space (Mac Low et al. 1989; Orr et al. 2022). A notable example of expanding superbubbles is the Orion-Eridanus superbubble [6] ~ 300 pc from our sun (e.g., Fuller et al. 2023). In starburst galaxies, metal diffusion is more energetic as shock waves generated by numerous CCSNe at the starburst core heat the surrounding ISM and make it an outflow or a galactic wind (Leroy et al. 2015; Zhang 2018). During continuous star formation, CCSN products will be transported into intergalactic space by galactic winds. Hence, superbubbles and galactic winds transport matter formed in galaxies to the outside and enrich intergalactic space.

2.2.2 Studies of enrichment

Cool cores and brightest cluster galaxies

Some clusters have a region of relatively low-temperature gas ~ 1 keV at their centres, which is called a cool core. The cool core of clusters is bright in X-ray, making it a good target for studying element abundances from X-ray spectra. In cluster cool cores, the most luminous galaxy in the systems is typically a large early-type galaxy (brightest cluster galaxies, BCGs). On entire core regions, Mernier et al. (2016) studied X-ray spectra of 44 early-type galaxies consisting of the cool core of 23 clusters, centres of groups (small clusters), and others. The metal abundance ratio to Fe in the hot gas observed in these systems matches the solar composition for O through Ca. Here, the abundance ratio to Fe is defined as the number ratio in the ISM, which is normalized by the corresponding value in the sun: $(n_{\rm Z}/n_{\rm Fe})/(n_{\rm Z}/n_{\rm Fe})_{\odot}$. The abundance ratios of Fe-peak elements are twice higher than the solar abundance ratios. This result suggested that the chemical enrichment histories, such as the relative contribution of supernova explosions in early-type galaxies, are different from normal spiral galaxies (e.g., de Plaa et al. 2007; Mernier et al. 2016). On the other hand, recent observations with high-resolution X-ray micro-calorimeter onboard *Hitomi* (Takahashi et al. 2018), a legacy of X-ray astronomy in Japan,

[6] About this object, submitted is a paper that is listed at the end of this thesis ([6] in List of Publications). However, the paper will not appear in subsequent chapters because its discussion is out of the main thrust of this dissertation.

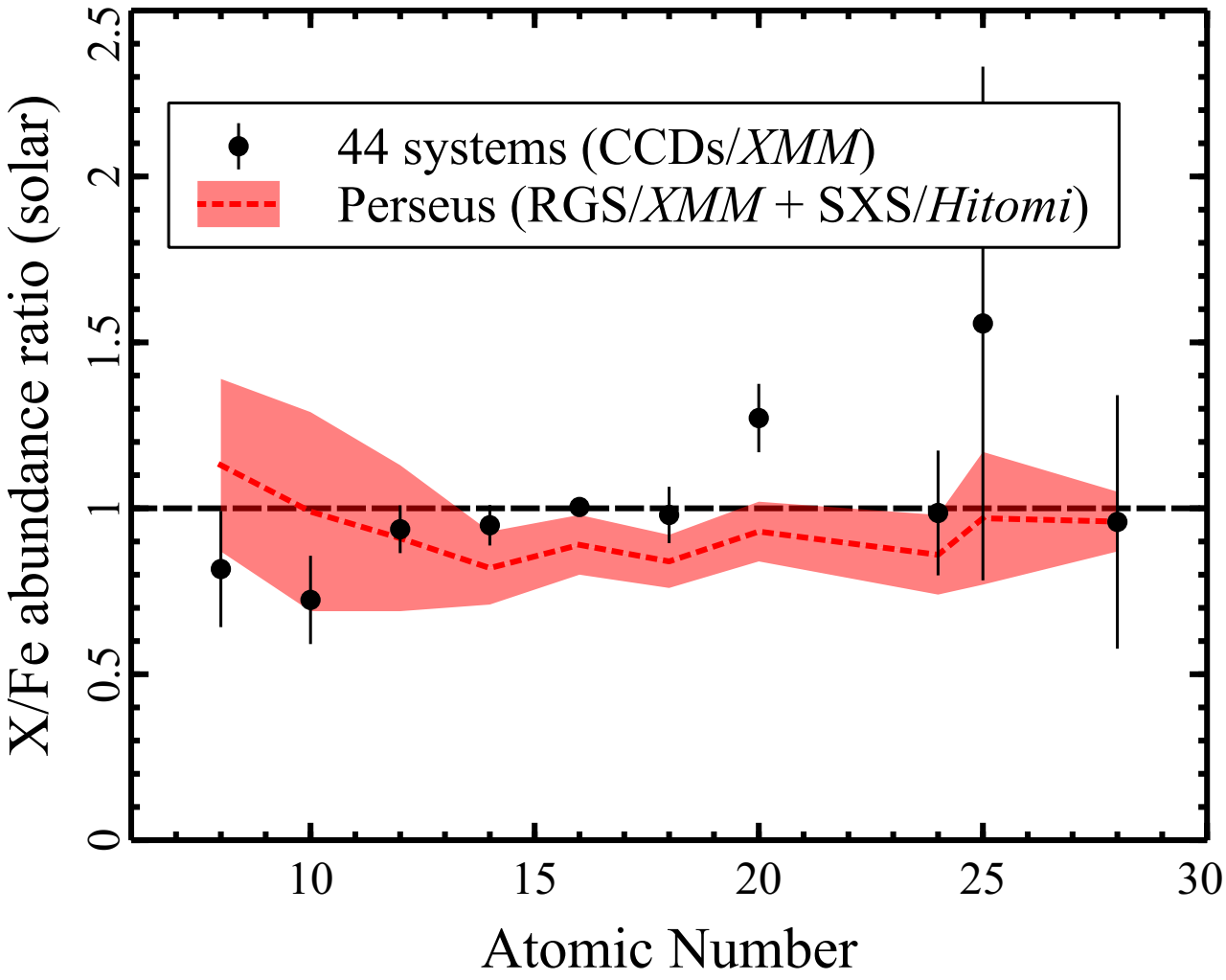

Figure 3: Observed abundance ratios of O/Fe, Ne/Fe, Mg/Fe, Si/Fe, S/Fe, Ar/Fe, Ca/Fe, Cr/Fe, Mn/Fe, and Ni/Fe in integrated on 44 systems (black points, Mernier et al. 2018c) and the Perseus core (red region, Simionescu et al. 2019). Mernier et al. (2018c) utilized the CCD data with *XMM-Newton*, and Simionescu et al. (2019) performed a joint analysis of *Hitomi* and *XMM-Newton*.

provide the solar abundance ratios of these metals in the core of the Perseus cluster (Hitomi Collaboration et al. 2017; Simionescu et al. 2019). After major updates on atomic codes, essential for spectral modelling, in response to *Hitomi* results (Hitomi Collaboration et al. 2018b), Mernier et al. (2018c) revisited the abundance of 44 systems and revealed the solar composition. Figure 3 shows these works that suggest a common chemical enrichment between ancient early-type galaxies and our Milky Way.

Astronomers will reproduce the observed abundance pattern by assuming predicted abundances in supernova nucleosynthesis models. The following equation easily

calculates the theoretical abundance ratios to Fe, for instance.

$$\frac{(n_{\rm Z}/n_{\rm Fe})}{(n_{\rm Z}/n_{\rm Fe})_\odot} = \frac{Y_{\rm Z}^{\rm CC} + r^{\rm Ia} Y_{\rm Z}^{\rm Ia}}{Y_{\rm Fe}^{\rm CC} + r^{\rm Ia} Y_{\rm Fe}^{\rm Ia}} \frac{A_{\rm Z}}{A_{\rm Fe}},$$

where Y is the model yield of each element and supernova (e.g., Nomoto et al. 2013 for CCSNe, Iwamoto et al. 1999 for SNe Ia), $r^{\rm Ia}$ is the number ratio of SNe Ia to CCSNe, and A is the atomic weight of each element. Note that the CCSN yields are averaged over various progenitor masses (e.g., 9–60 $\rm M_\odot$):

$$Y_{\rm Z}^{\rm CC} = \frac{\int_{9{\rm M}_\odot}^{60{\rm M}_\odot} M^{\rm s} Y_{\rm Z}^{\rm CC}(M) dM}{\int_{9{\rm M}_\odot}^{60{\rm M}_\odot} M^{\rm s} dM},$$

where M is a progenitor mass, and s is an index for initial mass functions that defines the stellar mass distribution in star formation [7]. The $r^{\rm Ia}$ parameter has been estimated using many cool cores, where SNe Ia account for 10–40 per cent of total SNe enriching the systems and are responsible for producing 60–70 per cent of observed Fe (e.g., de Plaa et al. 2007; Simionescu et al. 2015; Mernier et al. 2016; Erdim et al. 2021).

As suggested above, the metals in the hot gas are a mixture of all SN products over several Gyr and their composition will reflect the averaged nature of SN nucleosynthesis. Therefore, observing the abundance pattern in hot gases is a good way to study, for instance, the progenitor mass distribution of each type of SNe, which is difficult to determine from observations of individual SNe or SN remnants. Examples of the open question are as follows: which is a more plausible progenitor for SNe Ia, a near-$M_{\rm Ch}$ white dwaf or a sub-$M_{\rm Ch}$ one?; do extremely massive stars explode as CCSNe and contribute to the element supplies to the ISM? One important result is derived using the *Hitomi* data plotted in Fig. 3. The *Hitomi* observation of the Perseus core reveals that the abundances of Fe-peak elements require both contributions from sub- and near-$M_{\rm Ch}$ progenitors of SNe Ia (Hitomi Collaboration et al. 2017; Simionescu et al. 2019).

Metal distribution in the hot gas

On a larger scale, abundances of light elements like O and Mg are fairly uniform from the central galaxies to the outer regions up to ~ 100 kpc, and the Si and Fe abundances are higher towards the core (e.g., Böhringer et al. 2004). Therefore, the

[7] In a simple expression, the more massive stars are less likely to form. Generally, s = −2.35 is adopted from Salpeter (1955).

main source of light elements, i.e. CCSNe, might have a constant contribution to the chemical enrichment, and the SNe Ia contribution can become larger in the cluster centre region. However, there are counterarguments reported in recent works. In Mernier et al. (2017), the aforementioned 44 samples are examined for abundance variation in a broader region up to $\sim$ Mpc than in Mernier et al. (2016). They find that observed abundance ratios for O, Ne, Mg, Si, S, Ar, and Ca to Fe are flat around the solar value from the centre to the outskirts. Similar trends have been obtained in studies of some objects (e.g., Simionescu et al. 2015; Ezer et al. 2017; Erdim et al. 2021; Sarkar et al. 2022). Furthermore, such abundance flatness is a common trend independent of azimuthal direction (Werner et al. 2013; Simionescu et al. 2015). In these cases, the dominant faction of metals in the ICM at a large scale may be supplied by early-time enrichment (e.g., Werner & Mernier 2020).

In the innermost regions, a central few-kiloparsec core, there is sometimes an issue in the metal distribution. Johnstone et al. (2002) found a central Fe abundance depletion in the core of A2199. After this first report, some authors have proposed similar trends of abundance profiles, especially for the Fe abundance, in some cool-core systems (e.g., Sanders & Fabian 2002; Churazov et al. 2003; Panagoulia et al. 2015; Liu et al. 2019). Because the enhanced enrichment is expected from the central BCG, such decreasing trends of metal abundance are a conundrum. In some BCGs, hints of cold dust filaments are reported by optical and infrared observations (e.g., Crawford et al. 2005; Mittal et al. 2011, for the Centaurus cluster). Then, Panagoulia et al. (2015) proposed that these abundance declination originate from the depletion process of metals into cold dust grains. Meanwhile, according to a past prediction, the cooling time of the ICM in cool-core clusters is much shorter than the cluster age, leading to plenty of cold gas and star formation may be expected in the cluster cores (the cooling-flow model, e.g., Fabian 1994). Later X-ray studies of cool-core clusters disfavoured the presence of the gas by several times cooler than the surrounding region (e.g., McNamara & Nulsen 2012). The cooling-flow model also overestimates the star formation rates in cluster centres with some exceptions (e.g., Mittal et al. 2015). Nonetheless, some researchers have continued to discuss this model (e.g., Fabian et al. 2022, 2023a,b). Here, the cooling-flow model must support the abovementioned dust scenario. If the cooling-flow model — of course, the reason why the cold gas cannot be detected must be debated separately — is correct [8], the

[8]Recent works find that the Phoenix cluster of galaxies may have a strong cooling flow (Akahori et al. 2020; Timmerman et al. 2021). However, cooling flows are still not a property ubiquitous to other clusters.

efficient metal depletion into cold dust grains is naturally expected at cluster centres (and at centres of some cool-core systems). Recently, Lakhchaura et al. (2019) reported that the abundance of the noble gas element Ar in the Centaurus cluster shows a marginal central drop different from the abrupt drop of the Si, S, and Fe abundances. The different distribution of noble gases, which are hardly depleted into dust, and standard metals would provide a hint of the presence of the dust depletion process. However, spatial variation of the same noble gas Ne [9] is not studied in detail because it is hard to determine its abundance and distribution by usual X-ray analysis methods (see the subsequent sections).

These issues will be discussed in Chapters 3 and 4. If the dust storage scenario is questioned, it is implied that the currently observed element abundance in the ICM or ISM has not changed drastically from the initial composition. There is at least no difference in the changing trend between noble gases and ordinary metals, justifying the direct comparison between the SN yield models and the observed abundances. In addition, it may also raise an additive doubt about the validity of the cooling-flow model.

Galaxies

In smaller systems such as early-type galaxies, mineralogy is primarily the same as in clusters. Konami et al. (2014) has measured the abundance of 17 early-type galaxies distributed outside the cluster and group centres. The abundances are measured from the data observed by Japan's X-ray satellite *Suzaku* (Mitsuda et al. 2007). They report that the Fe abundance is about 0.8 solar, and that the O/Fe, Mg/Fe, and Si/Fe ratios are consistent with the solar composition. This trend is expected for all early-type galaxies in their sample. While the stellar content in early-type galaxies can possibly account for the bulk of observed Fe abundance, they also estimated the SNe Ia contribution to Fe as ~ 70 per cent. These results are globally consistent with the mineralogy in cluster or group cores. In the analysis of Chapters 3 and 4, all BCGs, group central galaxies, and other early-type galaxies may be treated simply as early-type galaxies despite differences in size and brightness.

The situation is significantly different in starburst galaxies. Based on the above-mentioned picture of starburst systems, it is naturally expected that the CCSN con-

[9] Although Ar may form interstellar molecules (ArH^+), there have been no reports of dust formation by Ne (McGuire 2022). Hence, the Ne distribution measurement will provide more conclusive results in testing the dust scenario.

tribution dominates the SN Ia in ISM enrichment. Indeed, this illustration has been confirmed by many X-ray studies of outflows from starburst galaxy cores. The outflow and/or core regions of these systems show abundance patterns of O, Ne, Mg, and Si close to those of CCSN yields (Yamasaki et al. 2009; Konami et al. 2011; Mitsuishi et al. 2013; Lopez et al. 2020; Mao et al. 2021). In a prototype starburst object M82, however, there remains an issue with high abundance ratios of Ne/O and Mg/O $>$ 1.5 solar (e.g., Tsuru et al. 1997; Ranalli et al. 2008; Konami et al. 2011; Zhang et al. 2014), which are even higher than the predicted values of present CCSN nucleosynthesis models. Recently, Okon et al. (2024) also reported the super-solar Ne/O and solar Fe/O ratios. They discuss the possibility of the dust depletion of O, which may more likely occur in starburst galaxies with active star formation than in early-type galaxies. They also argue the unnaturalness of the fact that other elements must also be depleted to dust to the same extent as O, inconsistent with solar Fe/O. Chapter 5 will challenge this high abundance problem in the ISM of M82.

2.2.3 X-ray emission from ISM

The ISM or ICM is classified as collisional ionization equilibrium plasma in which the gas dissociation and recombination are balanced at a high ionized state. Since the ISM are very tenuous (10^{-5}–10^{-1} cm^{-3}), they are transparent to X-ray radiation consisting of continuum and line components (Böhringer & Werner 2010). These radiative processes in the ISM are significantly different from cases in stars whose atmospheres are so dense and opaque that cause blackbody radiation.

When a free electron in thermal plasma is diffracted by positive ions (free-free), part of the kinetic energy of an electron will be radiated via electromagnetic waves, generating the continuum component of spectra. In the thermal bremsstrahlung process [10], the electron velocities follow a Maxwell-Boltzmann distribution. Thus, the emissivity (or luminosity, brightness, and so on) of thermal continuum X-ray from cosmic plasma is provided as

$$F_{\rm continuum} = \Gamma T^{1/2} n_{\rm H}^2,$$

where Γ, T, and $n_{\rm H}$ are a factor, the temperature of gas, and proton density, respectively (Tucker 2019, and references therein). Another important emission component in the ISM is emission lines (bound-bound). In this process, X-ray photons corresponding

[10]Minor origins of continuum spectra in very low-temperature plasma ($\lesssim$ 0.1 keV) are electron recombining radiation (free-bound) and two-photon radiation (bound-bound), for instance. However, these processes are not apparently related to the major part of this work.

to the difference in energy levels are emitted from excited ions; thus, the emission line spectra show a sharp peak at a specific energy. For example, in H-like ions in collisional ionization plasma, the emissivity of any line emissions for an element Z is expressed as

$$F_{\rm line} = \epsilon(T, Z) n_Z^2,$$

where ϵ is a constant determined by the type of atom, its charge state, plasma temperature, and so on (Tucker 2019, and references therein). In summary, to observe the continuum spectra of cosmic plasma corresponds to measurements of its temperature and density, and that centroid energies and intensities of an emission line provide the type of atom, its ionic state, and the number of elements, respectively.

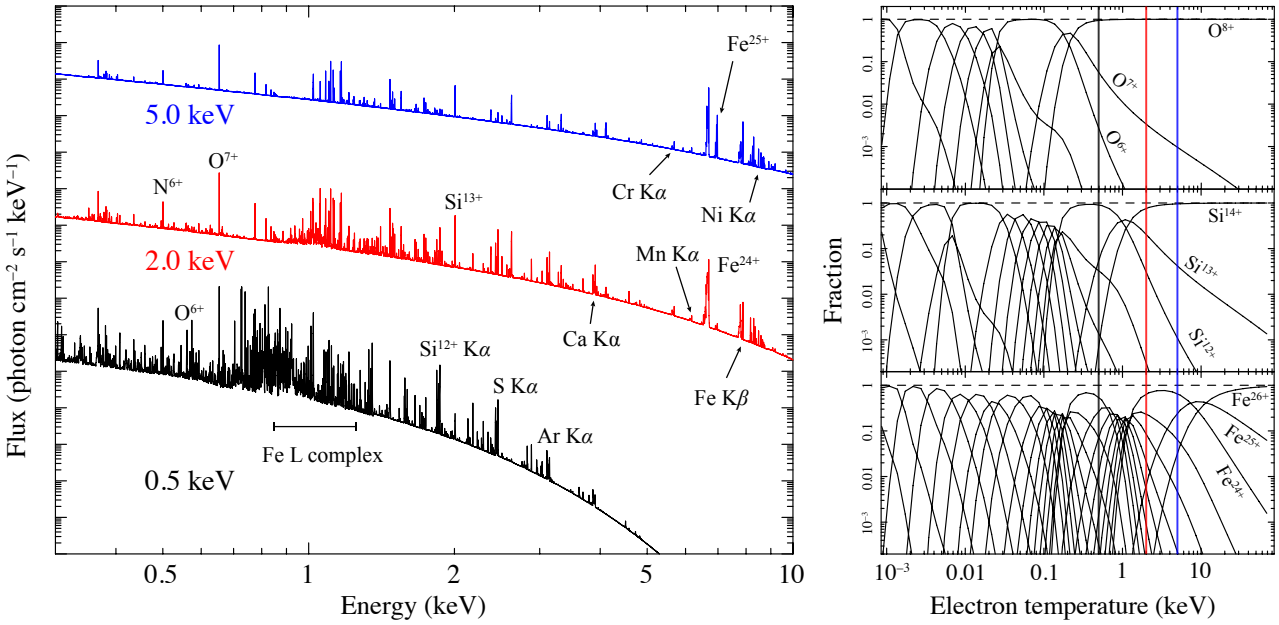

Figure 4: X-ray emission models and ion fraction in collisional ionization equilibrium plasmas. Left: Model X-ray spectra from plasmas at three temperatures 0.5 keV, 2 keV, and 5 keV. The brightness of the radiation is scaled for viewing purposes. The elemental composition of the plasma is assumed to be the proto-solar composition of Lodders et al. (2009). Right: The O, Si, and Fe ion fraction in collisional ionisation equilibrium plasmas calculated by Bryans et al. (2009).

Figure 4 shows model X-ray spectra from collisional ionization equilibrium plasmas with 0.5, 2, and 5 keV, assuming the plasma code of Foster et al. (2012). In Fig. 4, the emission lines at higher energies become stronger as the temperature increases. For example, as the 0.5 keV plasma is heated to 2 keV, the position of the K-shell emission line [11] of Si is shifted from ~ 1.8 keV to ~ 2 keV. This difference in the line centroid energy is due to changes in ionization, that is, the dominant charge state of Si is altered from H-like (Si^{+12} or Si XIII) to He-like (Si^{+13} or Si XIV). The ionization fraction in gases at specific temperatures is given in the right-hand panels of Fig. 4.

[11] The K-shell emission line is radiated during the de-excitation of an electron to the K shell ($n = 1$).

Clearly, the typical ISM temperature at galaxy centres (0.5–5 keV) result in highly ionized plasmas with He- and H-like ions. The characteristic structure apparent at ~ 1 keV is called the Fe L complex or the Fe L bump (Gastaldello et al. 2021). In particular, Fe L emission lines emit many emission lines around ~ 1 keV and share the same energy band with the Ne K-shell lines (0.9–1 keV), sometimes leading to uncontrolled uncertainties in spectral analysis.

2.3 X-RAY OBSERVATORY

Because almost all of the X-rays from extraterrestrial sources are absorbed by the Earth's atmosphere, space-based observations have been required for X-ray astronomy. For example, the Fe emission lines from clusters were first detected in the Perseus and Virgo clusters by the British X-ray astronomy satellite Ariel 5 and the US solar observing satellite OSO-8, marking the dawn of X-ray study of the ICM (Mitchell et al. 1976; Serlemitsos et al. 1977). Today, X-ray observations are usually carried out by putting satellites in orbit. Two X-ray missions related to this dissertation are *Chandra* (Fig.5(a)) and especially *XMM-Newton* (Fig.5(b)).

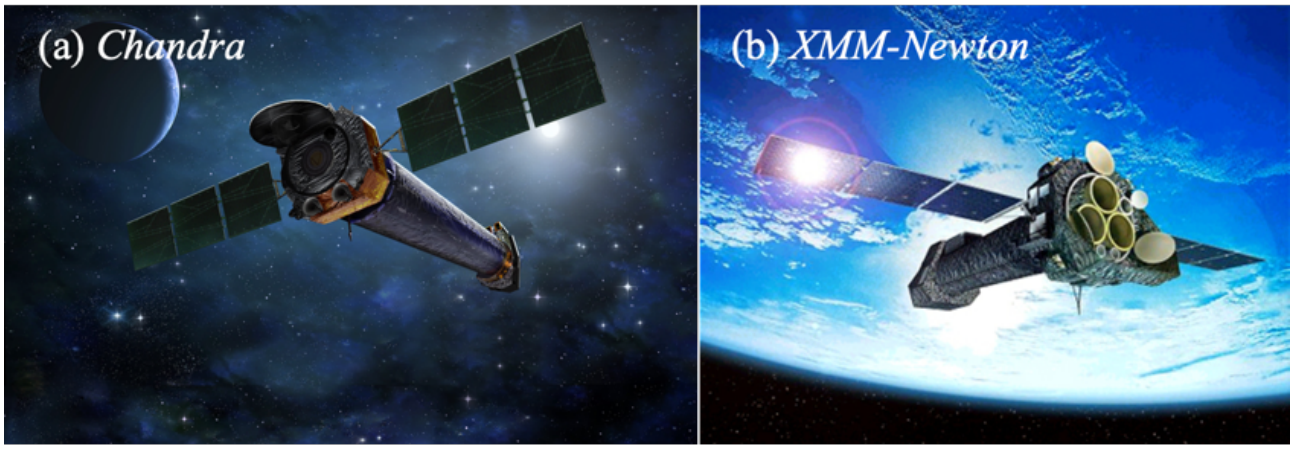

Figure 5: Two great legacies in X-ray astronomy; while still active. (a) Chandra X-ray Observatory (*Chandra*, © NASA, CXC, SAO, and Vaughan) and (b) *XMM-Newton* satellite (© ESA).

2.3.1 *Chandra*

Chandra is a US X-ray astronomy satellite launched in 1999 as part of the Great Observatories program [12] and has been operated by NASA[13] and others[14, 15]. The orbit takes a long elliptical shape with a perigee of 10,000 km and an apogee of 140,000 km, with a period of 65 hours. *Chandra* equips a large telescope with an aperture of 1.2 m and a focal length of 10 m, where the Advanced CCD Imaging Spectrometer (ACIS) is installed at the focus (Weisskopf et al. 2002). Each CCD chip has a field of view of $8' \times 8'$ and an astonishing angular resolution $\sim 0''.5$, the most significant resolution among all current X-ray missions. Generally, ACIS CCDs are available for the X-rays within the 0.3–10 keV band, with energy resolution $E/\Delta E \sim 17$ and 40 at 1.5 and 5.9 keV, respectively. Despite the modest spectral resolution, *Chandra* will access valuable information on temperature and metal distribution in the ISM.

2.3.2 *XMM-Newton*

XMM-Newton is an X-ray astronomy satellite that has been in operation since 1999 to date by ESA[16]. It runs once for 48 hours in a long elliptical orbit with a perigee of 6000 km and an apogee of 115,000 km. Figure 6 illustrates the open view of the spacecraft. *XMM-Newton* is equipped with three X-ray telescopes with an aperture of 70 cm and a focal length of 7.5 m. The X-ray telescope (at the bottom-left corner of the open view) has an effective area of 1500 cm^2 for 2 keV X-ray (Jansen et al. 2001), the largest of any current X-ray observatory, and its high light-gathering capacity achieves good photon statistics. Each of them has an X-ray CCD detector (at the top-right corner of the open view), the European Photon Imaging Camera (EPIC), on its focal plane: two MOS (MOS1 and MOS2, Turner et al. 2001) and one pn (Strüder et al. 2001). The field of view is $33' \times 33'$ for MOS and $27' \times 26'$ for pn. The angular resolution combined with each X-ray telescope is $\sim 6''$, which is modest compared to that of *Chandra*. Both CCDs are sensitive to X-rays of 0.2–12 keV, and the energy resolution at 1.0 keV and 6.4 keV is $E/\Delta E \sim 15$ and 45, respectively.

About half of the photons focused on the MOS are provided to the optical system of another important instrument Reflection Grating Spectrometer (RGS, den Herder

[12] The others are the Hubble Space Telescope (1990 to date), the Compton Gamma Ray Observatory (1991–2000), and the Spitzer Space Telescope (2003–2020).

[13] https://www.nasa.gov/

[14] https://www.cfa.harvard.edu/

[15] https://cxc.harvard.edu/

[16] http://www.esa.int/

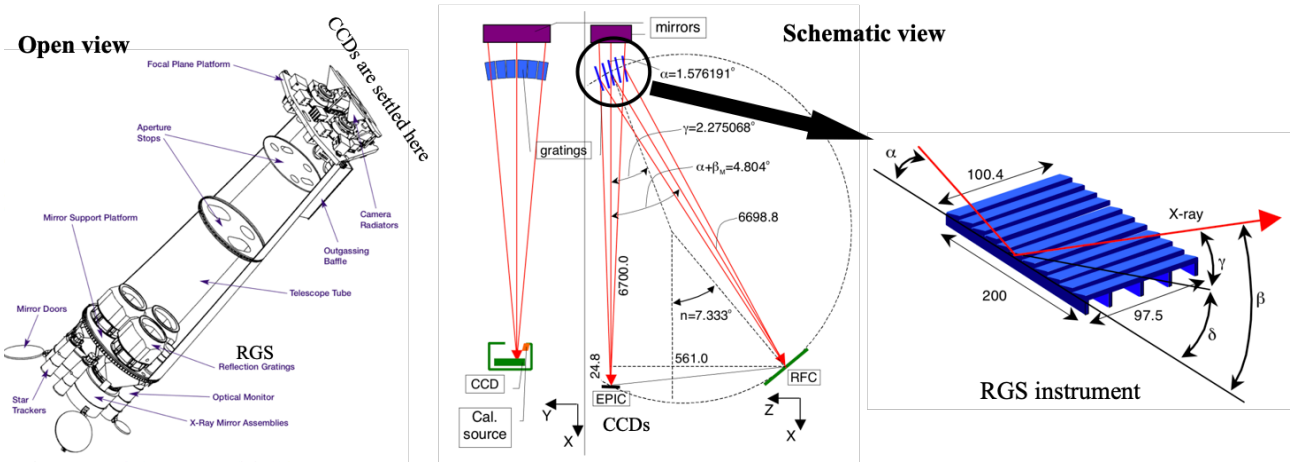

Figure 6: Open and schematic views of the optical system of *XMM-Newton*. The open view is retrieved from Barré et al. (1999), and the schematic ones are from den Herder et al. (2001). Some comments and labels are added.

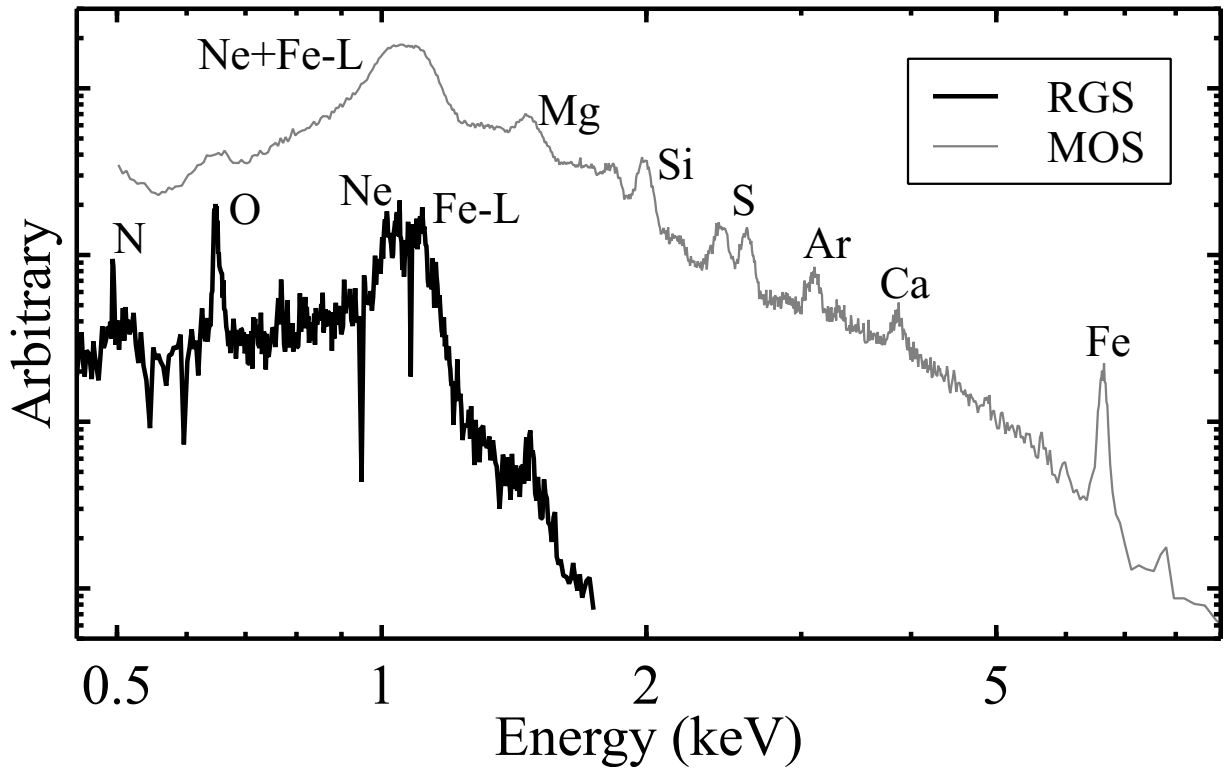

Figure 7: Comparison of the RGS and MOS spectra. Each spectrum is derived from the Centaurus cluster.

et al. 2001). Following a mechanism of diffraction grating spectroscopy, the RGS instrument disperses the incident light in a certain direction, which is illustrated in a schematic view of Fig. 6. As situations in a transmission grating, the dispersion relation is $m\Delta\lambda = d(\cos\beta - \cos\alpha)$, where m is the spectral order, d is the spacing, and α and β are the incident and dispersed angles, respectively. Dispersed X-ray photons will be detected at specific positions on the detector depending on energy;

thus, RGS does not have the imaging capability of a CCD detector. It is cautious that spatial information on source emission along the RGS dispersion direction is hard to obtain, *but along cross-dispersion direction though*. For X-rays in the 0.35–2 keV band, including N, O, Ne, Mg, and Fe-L lines, RGS has high spectral resolution $E/\Delta E \sim 100$–500, which even surpasses the X-ray micro-calorimeter on *XRISM* ($E/\Delta E \sim 50$–300, XRISM Science Team 2020). Figure 7 compares the RGS and MOS spectra around the Fe L complex, where the CCD cannot resolve the Fe L bump. For instance, the RGS data provide a powerful probe for estimating the Ne abundance in the ISM.

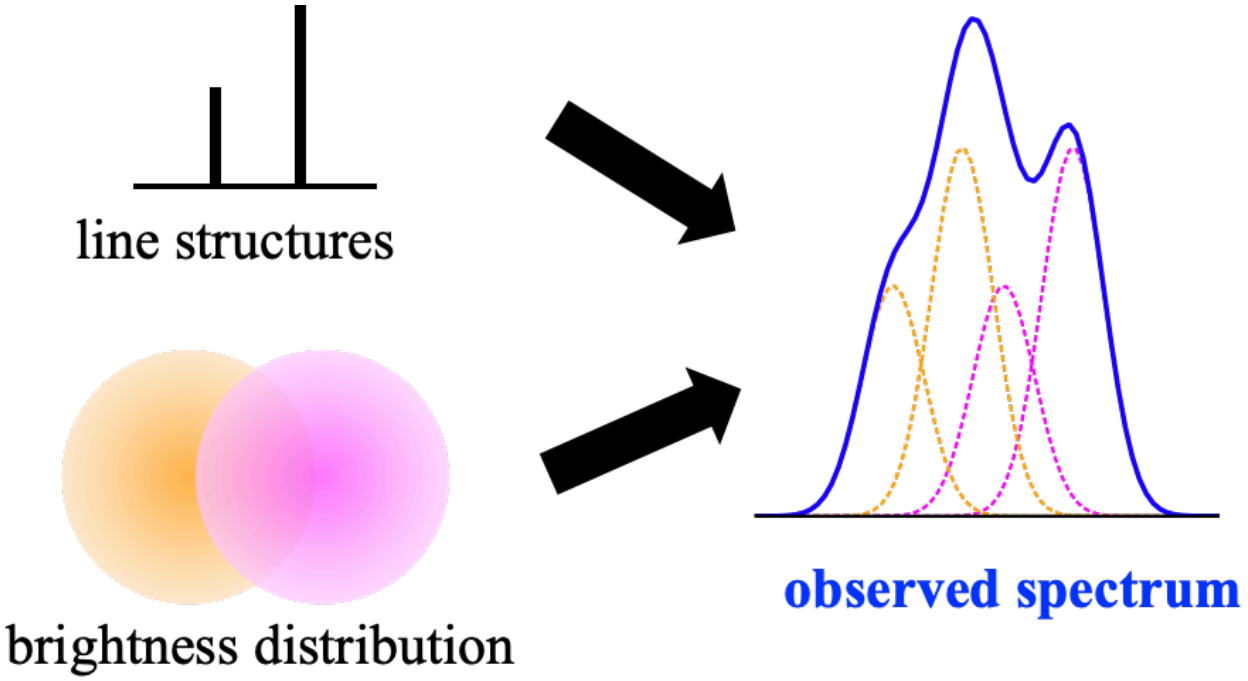

Figure 8: Schematic image of the line broadening of RGS spectra.

While RGS has a great resolving power on soft X-rays, careful treatments are needed to analyse extended emissions. The RGS instrument was initially intended to observe point-like sources with less diffuse emission structures, such as black holes. Any source extension larger than ~ 0.8 arcmin results in a line-broadening effect as $\Delta\lambda = 0.138\Delta\theta$ (in first-order spectra), where $\Delta\lambda$ is a line broadening in units of 10^{-8} cm and $\Delta\theta$ is an extension in units of arcmin (e.g., Mao et al. 2023). Globally uniform emission sources like the central ISM of early-type galaxies broaden each line, which would rarely affect the abundance or temperature estimate [17]. When observing sources with complex brightness distribution, the situation is more serious. Assuming two emission lines from a double-peaked source, if this

[17] Of course, the spectral resolution will be decreased.

structure is distributed along the dispersion direction of RGS, information of original line structures and the double-peaked feature easily degenerates as depicted in Fig. 8. In these cases, to model the observed spectrum, i.e. estimating abundances and temperatures, is more difficult unless the spatial distribution of emission is fully known. One may approximate the brightness distribution using X-ray CCD images and convolve the model with the images to reduce any line-broadening contamination (e.g., Tamura & Ohta 2004). This method will be used in RGS analyses in Chapters 3, 4, and 5, especially with more careful handling in Chapter 5.

Chapter 3

Chemical Enrichment in the Centaurus Cluster Core

3.0 Statement

This chapter is from a published paper *"Chemical enrichment in the cool core of the Centaurus cluster of galaxies"* authored by **K. Fukushima**, S. B. Kobayashi, and K. Matsushita (Monthly Notices of the Royal Astronomical Society, Volume 514, Issue 3, Pages 4222–4238). Embargoes of the published version of this article have been lifted. Note that moderate corrections are made to incomprehensible parts and typos in the arXived version.

A statement in accordance with the self-archiving policy of the Oxford University Press: *This is a pre-copyedited, author-produced version of an article accepted for publication in Monthly Notices of the Royal Astronomical Society following peer review. The version of record mentioned above is available online at:* https://doi.org/10.1093/mnras/stac1590.

3.1 Introduction

Metal abundances in stars and hot gas in galaxies provide reasonable constraints on the formation and evolutionary history of the universe. Apart from primordial ones such as H, He, and Li, other heavier chemical elements were synthesized in stars and expelled into the interstellar space by supernova (SN) explosions. Light α-elements (O, Ne, Mg) dominantly originate from core-collapse SNe (CCSNe), and heavy Fe-peak ones (Cr, Mn, Fe, Ni) are, on the other hand, forged by thermonuclear explosions of Type Ia SNe (SNe Ia). The intermediate-mass elements (IMEs), i.e. Si, S, Ar, and Ca, are synthesized by both SNe Ia and CCSNe (e.g., Nomoto et al.

2013, and references therein). Different from these metals, N is mainly synthesized in low- or intermediate-mass stars and dispersed into the interstellar medium (ISM) through stellar mass loss (e.g., Nomoto et al. 2013).

The intracluster medium (ICM), hot X-ray emitting plasma pervading the galaxy clusters, retains a dominant fraction of heavy elements (e.g., N, O, Ne, Mg, Si, S, Ar, Ca, Cr, Mn, Fe, and Ni) synthesized by stars and SN explosions in member galaxies. The abundance of these elements can be reasonably constrained from the intensity of their K-shell emission lines within the X-ray band (e.g., Mernier et al. 2018a, for a recent review). Therefore, X-ray spectroscopy of the ICM is one of the most reliable ways to investigate the chemical enrichment history in clusters (e.g., de Plaa et al. 2007; Sato et al. 2007; Mernier et al. 2018b). In the last few decades, spatially resolved spectra of the ICM observed with modern X-ray observatories like *Chandra*, *XMM-Newton* and *Suzaku* have allowed us to study the spatial distribution of metals in the ICM. Outside the core regions, flat and azimuthally uniform Fe distributions towards the outskirts have been reported (e.g., Matsushita 2011; Matsushita et al. 2013a; Werner et al. 2013; Simionescu et al. 2015; Urban et al. 2017). This remarkably extended Fe distribution requires the early enrichment of the ICM before the cluster formation, i.e. ten billion years ago, also supported by cosmological simulations (e.g., Biffi et al. 2018).

X-ray luminous clusters with a prominent surface brightness peak at the centre, i.e. cool-core clusters, are ideal targets for studying the ongoing enrichment process in the brightest cluster galaxies (BCGs). Most of them are classified as early-type galaxies and located in the X-ray peak of the cool cores. Observational studies of the metal abundances in cool cores provide a powerful probe for where and when metals were dispersed into the ICM. A central Fe abundance excess within the ICM was first reported in the Centaurus cluster by *ROSAT* and *ASCA* (Allen & Fabian 1994; Fukazawa et al. 1994). Many other cool-core clusters exhibit similar trends for element abundances (e.g., De Grandi & Molendi 2001; Million et al. 2011; Mernier et al. 2017). Aiming to explain the central Fe abundance peaks, Böhringer et al. (2004) proposed an enrichment by SNe Ia over a relatively long time (> 5 Gyr). In addition, the enhanced metal enrichment by CCSNe at the active star-forming era of cluster galaxies has been discussed based on central peaks of α-elements (e.g., de Plaa et al. 2006; Simionescu et al. 2009; Mernier et al. 2017; Erdim et al. 2021). Recent observation in the Perseus cluster core by *Hitomi* raised counter discussion that the O/Fe, Ne/Fe, Mg/Fe, Si/Fe, S/Fe, Ar/Fe, Ca/Fe, Cr/Fe, Mn/Fe, and Ni/Fe abundance ratios in the ICM are entirely consistent with the solar composition, and

therefore our Milky Way (Hitomi Collaboration et al. 2017; Simionescu et al. 2019). This solar chemical composition in the Perseus core requires not only CCSN but also near- and sub-Chandrasekhar mass ($M_{\rm Ch}$) SN Ia contribution to the enrichment of the ICM. Although the abundance ratio pattern could not be reproduced sufficiently by the latest SN nucleosynthesis models, the study of the Perseus core provided an important clue to chemical enrichment in the cluster centre and possibly BCG.

Within a central few-kiloparsec, the situation is more puzzling and fascinating in the innermost core. Since the first discovery in A2199 (Johnstone et al. 2002), central abundance drops are reported especially for Fe in some cool-core clusters wherein the enhanced enrichment is expected from the central BCG (e.g., Churazov et al. 2003; Panagoulia et al. 2015; Liu et al. 2019). The central abundance drop in the Centaurus cluster was first discovered by Sanders & Fabian (2002) with a remarkable depletion from ~ 2 to ~ 0.5 solar towards the centre. With optical and infrared observations, cold dust filaments are detected in BCGs (e.g., Crawford et al. 2005; Mittal et al. 2011, for the Centaurus cluster), and Panagoulia et al. (2015) proposed that these abundance drops would be caused by depletion of metals into the cool dust grains in the BCG. Lakhchaura et al. (2019) reported that the abundance of the "non-reactive" element Ar shows a relatively slight central drop, while Si and S show a remarkable abundance drop as Fe. The abundance drops may originate from the feedback of active galactic nuclei which would dissipate a fraction of central metal-rich gas towards the outer radius (e.g., Sanders et al. 2016; Liu et al. 2019).

The Centaurus cluster, also known as A3526, is a well-known cool-core cluster, within which NGC 4696 resides as the BCG. Because being a nearby and X-ray luminous galaxy cluster, the Centaurus cluster is one of the most interesting examples, as well as the Perseus cluster for studies of the metal abundance in the ICM. It has been reported that the abundance in a few-arcmin core of the Centaurus cluster shows super-solar (~ 1.5–2 solar) value for IMEs and Fe by X-ray missions like *Chandra*, *XMM-Newton*, and *Suzaku* (e.g., Matsushita et al. 2007; Takahashi et al. 2009; Sakuma et al. 2011; Sanders et al. 2016). The Fe abundance in other cluster cores, on the other hand, is typically sub-solar (~ 0.8 solar), which is close to those of groups and early-type galaxies (e.g., Konami et al. 2014; Mernier et al. 2018c). Then, the Centaurus cluster core do be the specific but ideal target for a comprehensive study of the SN Ia contribution to the enrichment due to the high Fe abundance.

In this part, we analyse the deepest CCD data with *Chandra* and *XMM-Newton* to date of the cool core of the Centaurus cluster and NGC 4696. We study the spatial distributions of metal abundances of O, Mg, IMEs, and Fe-peak elements, including

Cr, Mn, and Ni, in order to constrain the metal enrichment history by the BCG. In addition, we analyse grating data with *XMM-Newton* for investigating the spatial distribution of Ne and N. Due to its non-chemical reactivity, the radial distribution of the Ne abundance would be crucial to restrict the mechanism of abundance drops at the cluster centre. We also make a comparison between the latest versions of two different atomic codes, the atomic database (AtomDB, Foster et al. 2012) and the SPEX Atomic Code and Tables (SPEXACT, Kaastra et al. 1996), which have been updated after the *Hitomi* observation (Hitomi Collaboration et al. 2018b). This chapter is organized as follows. In Sect. 3.2, we describe details of our *Chandra* and *XMM-Newton* observations and data reduction. In Sect. 3.3, we present our spectral analysis. We discuss the results in Sect. 3.4. In this chapter, we assume cosmological parameters as $H_0 = 70\,\mathrm{km\,s^{-1}\,Mpc^{-1}}$, $\Omega_m = 0.3$ and $\Omega_\Lambda = 0.7$, for which 1 arcsec corresponds to ~ 0.2 kpc at the redshift of 0.0114 for NGC 4696 (Struble & Rood 1999). All abundances in this work are relative to the proto-solar values of Lodders et al. (2009). The errors are at 1σ confidence range unless otherwise stated.

3.2 Observations and Data Reduction

We used the publicly archival observation data of the core region of the Centaurus cluster with the *Chandra* Advanced CCD Imaging Spectrometer (ACIS, Weisskopf et al. 2002), the European Photon Imaging Camera (EPIC, Turner et al. 2001; Strüder et al. 2001), and Reflecting Grating Spectrometer (RGS, den Herder et al. 2001) on-board *XMM-Newton*. Table 1 lists the observations analysed in this chapter.

3.2.1 Chandra

We used *Chandra* Interactive Analysis of Observations (CIAO) version 4.12 (Fruscione et al. 2006) and calibration database (CALDB) version 4.8.4.1 for the following data reduction. We reprocessed the data with `chandra_repro` tool, keeping the standard procedure by *Chandra* team, and removed strong background flares using `deflare` script in the CIAO package. The cleaned exposure of ACIS is 640 ks after the deflaring procedures stated above. We also searched for faint point sources using the `wavdetect` algorithm in the 0.5–7.0 keV window, assuming the encircled counts fraction = 0.9 and the threshold significance = 10^{-6}. The sources detected at the cluster centre and the surrounding ICM were left un-excluded (e.g., plume-like structure, Sanders et al. 2016). We extracted ACIS spectra from the annular regions

Table 1: List of observations used in this work

Obs. ID	Instrument	Cleaned Exposure (ks)	Offset[a] (arcmin)	Date
		Chandra		
504	ACIS-S	20.85	0.13	2000 May 22
505	ACIS-S	8.97	0.13	2000 Jun 08
4190	ACIS-S	30.52	3.79	2003 Apr 18
4191	ACIS-S	30.20	4.23	2003 Apr 18
4954	ACIS-S	73.73	0.10	2004 Apr 01
4955	ACIS-S	36.33	0.10	2004 Apr 02
5310	ACIS-S	40.60	0.10	2004 Apr 04
16223	ACIS-S	144.72	0.10	2014 May 26
16224	ACIS-S	29.40	0.10	2014 Apr 09
16225	ACIS-S	28.32	0.10	2014 Apr 26
16534	ACIS-S	47.17	0.10	2014 Jun 05
16607	ACIS-S	39.92	0.10	2014 Apr 12
16608	ACIS-S	23.09	0.10	2014 Apr 07
16609	ACIS-S	71.97	0.10	2014 May 04
16610	ACIS-S	16.43	0.10	2014 Apr 27
		XMM-Newton		
0046340101	MOS1	43.26	0.002	2002 Jan 03
	MOS2	43.55		
	pn	30.46		
	RGS1	44.83		
	RGS2	43.51		
0406200101	MOS1	100.91	0.11	2007 Aug 22
	MOS2	103.69		
	pn	71.88		
	RGS1	101.58		
	RGS2	101.58		
0823580101	MOS1	102.26	10.7	2018 Jul 03
	MOS2	104.39		
	pn	104.39		
0823580201	MOS1	100.77	11.6	2018 Aug 09
	MOS2	102.79		
	pn	76.06		
0823580501	MOS1	96.85	10.3	2018 Jul 20
	MOS2	98.37		
	pn	72.65		
0823580601	MOS1	99.88	11.3	2018 Jul 30
	MOS2	99.78		
	pn	74.25		

[a] The angular distance from NGC 4696 to the target coordinates of each observation.

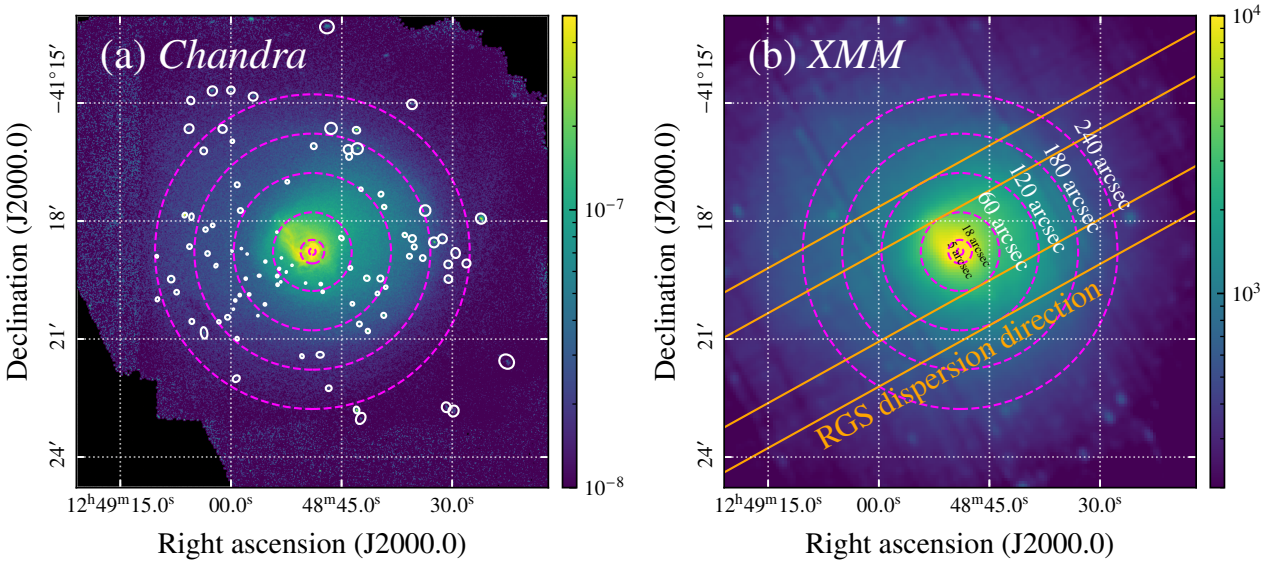

Figure 9: Images of the Centaurus cluster core in the 0.5–7.0 keV band. (a) Vignetting corrected image with the *Chandra* ACIS-S, where the colour bar indicates photon flux in $\mathrm{cm}^{-2}\,\mathrm{s}^{-1}$. The magenta dashed annuli represent 5, 18, 60, 120, 180, and 240 arcsec spectrum extraction regions. The white ellipses show the detected point sources (see Sect. 3.2.1 for details). (b) A mosaiced count image with the *XMM-Newton* EPIC MOS and pn. The extraction region for RGS spectra (60–120 arcsec width on both sides, for instance) is shown with the orange lines, where the cross-dispersion width of RGS is between 60 and 120 arcsec lines.

shown in Fig. 9(a) and generated redistribution matrix files (RMFs) and ancillary response files (ARFs) for each ObsID. The outermost radius of our extracting regions (240 arcsec) is about three times the effective radius (R_e) of NGC 4696 ($\sim$ 85 arcsec, Carollo et al. 1993), indicating that most of the stars in NGC 4696 are within our extraction regions. In addition, this aperture is close to a radius at which the ICM temperature starts to decline towards the centre (Sanders et al. 2016). The spectra and response files taken in the same observation years were co-added to improve the photon statistics. Background spectra were extracted from all fields of view of the ACIS-S3 chip out of 3 arcmin core centred on the cluster centre.

3.2.2 XMM-Newton

3.2.2.1 EPIC

The reduction procedure for the data sets of *XMM-Newton* was performed using the *XMM-Newton* Science Analysis System (SAS) version 18.0.0. We reprocessed and filtered all the EPIC data using `emchain` and `epchain` for the MOS and pn, respectively. The excluding sources are taken from the *Chandra* ACIS detection (Fig. 9(a)) at the same position and radius. All reprocess procedures are in accordance

with the standard reduction criteria by SAS. After the reprocessing procedure, the total exposure times are 550 ks (MOS) and 380 ks (pn). For each observation, we extracted EPIC spectra from the same annular regions as *Chandra* (Fig. 9(b)) and generated RMFs and ARFs for each ObsID, but did not merge them because the aim points of each observation are significantly shifted. We fit the spectra of MOS1 and MOS2 jointly with the same spectral parameters. The background spectra were extracted from the 7.5–11.7 arcmin annular region.

3.2.2.2 RGS

The RGS spectra provide us spatial information of extended emission over a 5 arcmin width along the cross-dispersion direction when the X-ray peak of the target is close to the pointing position (e.g., Chen et al. 2018; Zhang et al. 2019). Therefore, we used only two datasets in 2002 and 2007 that have much smaller offsets than the others (see Table 1). The RGS data were processed with the `rgsproc` task. After removing flared events as well as the EPIC data, the remaining total exposure time is 140 ks. As done by Chen et al. (2018), we extracted first- and second-order RGS spectra centred on the emission peak along the dispersion direction instead of using the `xpsfincl` that is generally used. For each annular region within 120 arcsec for the CCD spectra, we selected events by the cross-dispersion width and extracted spectra over two wide regions on either side. For example, the two broad regions for 60–120 arcsec are plotted in Fig. 9(b). The first- and second-order spectra are fitted together, combining the RGS1 and RGS2 spectra of each order.

3.3 Analysis and Results

3.3.1 Spectral fitting

3.3.1.1 CCD spectra

Here, we analyse X-ray spectra extracted from the annular regions shown in Fig. 9 using XSPEC package version 12.10.1f (Arnaud 1996). We use the latest AtomDB [18] version 3.0.9 to calculate collisional ionization equilibrium (CIE) plasma models. We model and fit the background spectra simultaneously with the source spectra, instead of subtracting them from the source data. The detector background model consists of a broken power-law with Gaussian lines for the instrumental fluorescence

[18] http://www.atomdb.org

lines of Al-K, Si-K, and Cu-K (e.g., Leccardi & Molendi 2008; Mernier et al. 2015). We also take the celestial background emissions into account with a power-law (1.4 photon index) for the cosmic X-ray background and two CIE plasma components with solar metallicity for the local hot bubble (LHB) and the Galactic thermal emission (e.g., Yoshino et al. 2009; Sugiyama et al. 2023). These background components, except for the LHB, are modified by the Galactic absorption and the temperature of the LHB is fixed to 0.1 keV. The derived temperature of the Galactic thermal emission is 0.94 ± 0.02 keV, indicating that the Centaurus cluster is located in a high-temperature region of the Galactic emission (Yoshino et al. 2009; Nakashima et al. 2018; Ueda et al. 2022; Sugiyama et al. 2023). Because the ICM of the Centaurus cluster is extended over several degrees, the emission component from the ICM is also included in the spectral fitting model for the background region. In the following spectral analysis, we fit all spectra using the C-statistics (Cash 1979), to estimate the model parameters and their error ranges without bias (Kaastra 2017). The spectra are re-binned to have a minimum of 1 count in each spectral bin. The stacked spectra of the central 240 arcsec region are shown in the upper panel of Fig. 10. Emission lines of O, Ne+Fe-L, Mg, Si, S, Ar, Ca, Fe, and Ni+Fe are prominent in the spectra. In addition, there are some hints of the Cr and Mn lines in the pn spectrum.

Systematic uncertainties in the response matrices and atomic codes would bias the measurements of line and continuum temperatures. Following the arguments of Hitomi Collaboration et al. (2018a), we adopt the `bvvtapec` model, allowing different line and continuum temperatures. The ICM emissions are modelled with a triple `bvvtapec` component to consider the multi-phase structure of the cool core, assuming that the three thermal plasmas share the same metal abundances. The Galactic extinction is modelled using the `phabs` model with the photoelectric absorption cross-sections retrieved from Verner et al. (1996). We let the absorption column density $N_{\rm H}$ and elemental abundance of O, Ne, Mg, Si, S, Ar, Ca, Cr, Mn, Fe, and Ni vary freely. The abundances of elements lighter than O are fixed to solar. The other metal abundances are tied to those of the nearest lower atomic number elements that are allowed to vary. For example, the F abundance is linked to the free one of O. The line and continuum temperatures for the middle- and coolest-temperature components cannot be constrained independently; and thus, they are set to be half and quarter values of the hottest ones, respectively. We also let the volume emission measure (VEM) be a free parameter. The VEM parameter is defined as $\int n_e n_{\rm H} dV/(4\pi D^2)$, where n_e and $n_{\rm H}$ is electron and proton density, V and D are the volume of the emission region and the distance to the emitting source, respectively.

This model gives good fits to the spectra of the individual annular regions, yielding C-stat/dof $\sim$ 1–1.3 as summarized in Table 2 and Fig. 10. Since the differences between line and continuum temperatures are small (< 0.3 keV), we hereafter report only the continuum temperature as representative. As shown in Fig. 11, the different CCD detectors provide consistent VEM-weighted average temperatures (denoted by kT) for each annular region. This profile shows a peak temperature of ~ 3 keV and a remarkable drop at the centre, which is consistent with the more extended temperature variation proposed by Sanders et al. (2016). As expected in Sect. 3.2.1, our extracting regions must encompass important parts of the cool core of the Centaurus cluster.

Next, we re-fit the spectra within local energy bands centred on the K-shell emission lines of each element, so that we minimize the biases due to the response uncertainty on the abundance measurements; namely, we perform local or narrow-band fits (e.g., Lakhchaura et al. 2019; Simionescu et al. 2019). The ratios of each VEM are fixed to the value obtained from the global fit, leaving the abundance of a considered metal to vary freely and tying all other parameters to the global fit results in Table 2. The bandpasses of our local fits are 0.51–0.77 keV for O, 0.75–1.25 keV for Ne, 1.36–1.59 keV for Mg, 1.65–2.26 keV for Si, 2.37–4.44 keV for other IMEs, i.e. S, Ar, and Ca, 5.01–6.59 keV for Cr and Mn, 6.25–7.25 keV for Fe, and 7.24–8.02 keV for Ni. Here, we use the two pn observations towards the cluster centre for the local fits around the Ni lines, avoiding contaminations from the strong instrumental Cu line. The representative spectrum and the best-fitting residuals around each prominent line are plotted in the lower panels of Fig. 10. The obtained elemental abundances with the local fits are shown in Table 3 and 4. In Fig. 12, we compare the derived abundances from the global and local fits. The abundance values and the residual structure around each K-shell emission line with two fitting methods are globally similar to each other, except for the Cr abundances. The Ne abundances with the two methods are largely consistent, apart from the results with pn that offers a lower spectral resolution than that of MOS. However, the Ne K-shell emission lines are blended in the Fe-L bump, and thus, our Ne abundance estimate from the CCD spectra would be affected by some systematic uncertainties. The Mg abundances with pn and ACIS show a relatively large scatter, whose K-shell emission lines are also blended in the Fe-L bump. At the same time, those with MOS, possibly the most reliable instrument among the three, are consistent except for only one point. We suspect that the moderate spectral resolution and/or sensitivity of the pn and ACIS instruments mainly causes these different Mg abundances. The local fits around the Fe-K lines mostly give results consistent with those from the global fits. The exceptions are the three regions within

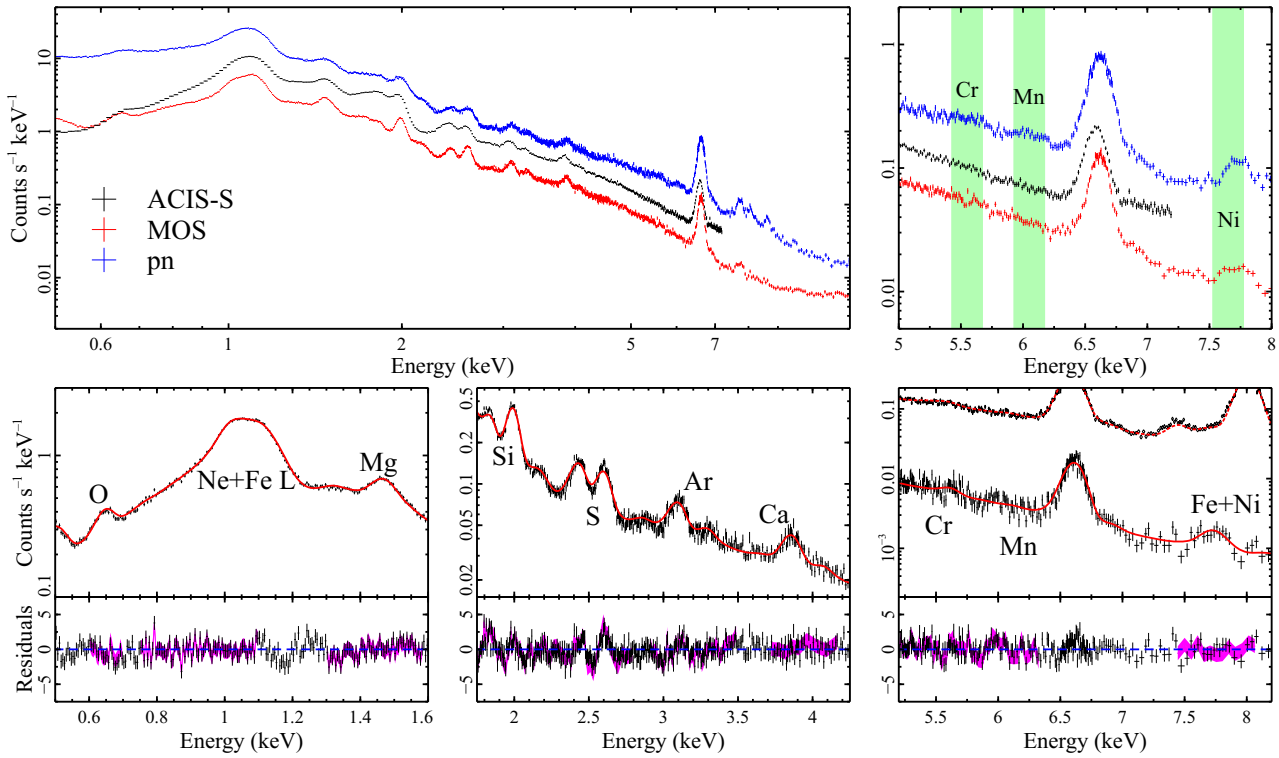

Figure 10: Upper: The stacked spectra of the central 240 arcsec region for each CCD camera, all of which are folded through the spectral response of each detector. The black, red, and blue data represent ACIS-S, MOS, and pn spectra, respectively. We also plot narrow-band spectra to show the emission lines of the Fe-peak elements. Lower: The representative spectra extracted from 18–60 arcsec annular region for MOS and best-fitting models enlarging on prominent K-shell emission lines. The black and magenta residuals represent the global and local fit results, respectively (see Sect. 3.3.1.1 for detail). The pn spectrum is also plotted with diamonds for the Fe-peak elements. Emission lines for some elements are marked.

60 arcsec with *Chandra* and the innermost region with pn, where the local fits give even lower Fe abundances than the global fits. Hereafter, we use the results of the global fits for the Fe abundance, and those of the local fits for the other elements.

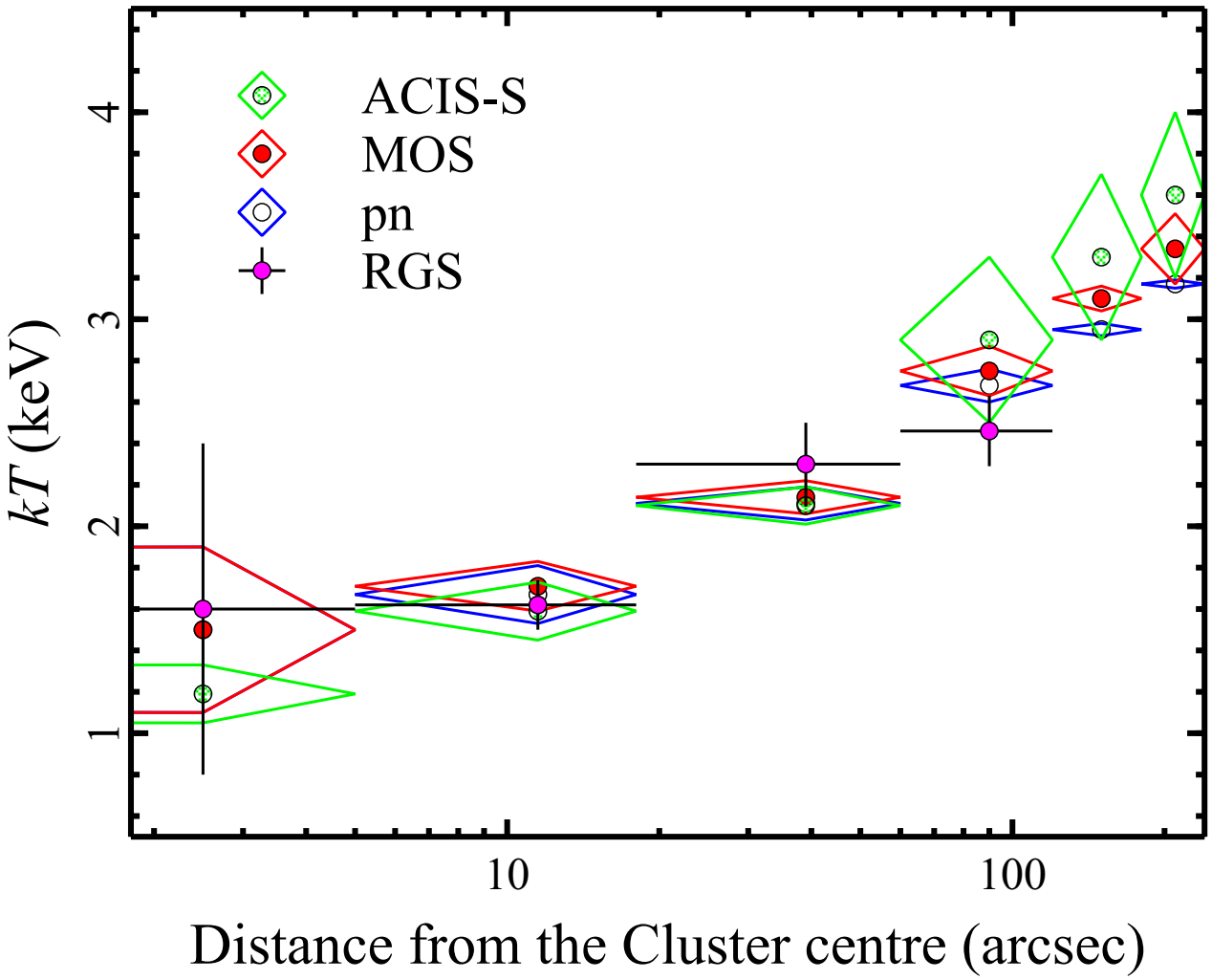

Figure 11: Radial profile of the VEM-weighted average temperature. The green-, red-, and blue-diamond plots are for results with *Chandra* ACIS-S, *XMM-Newton* MOS, pn, respectively. The magenta plots indicate the RGS results.

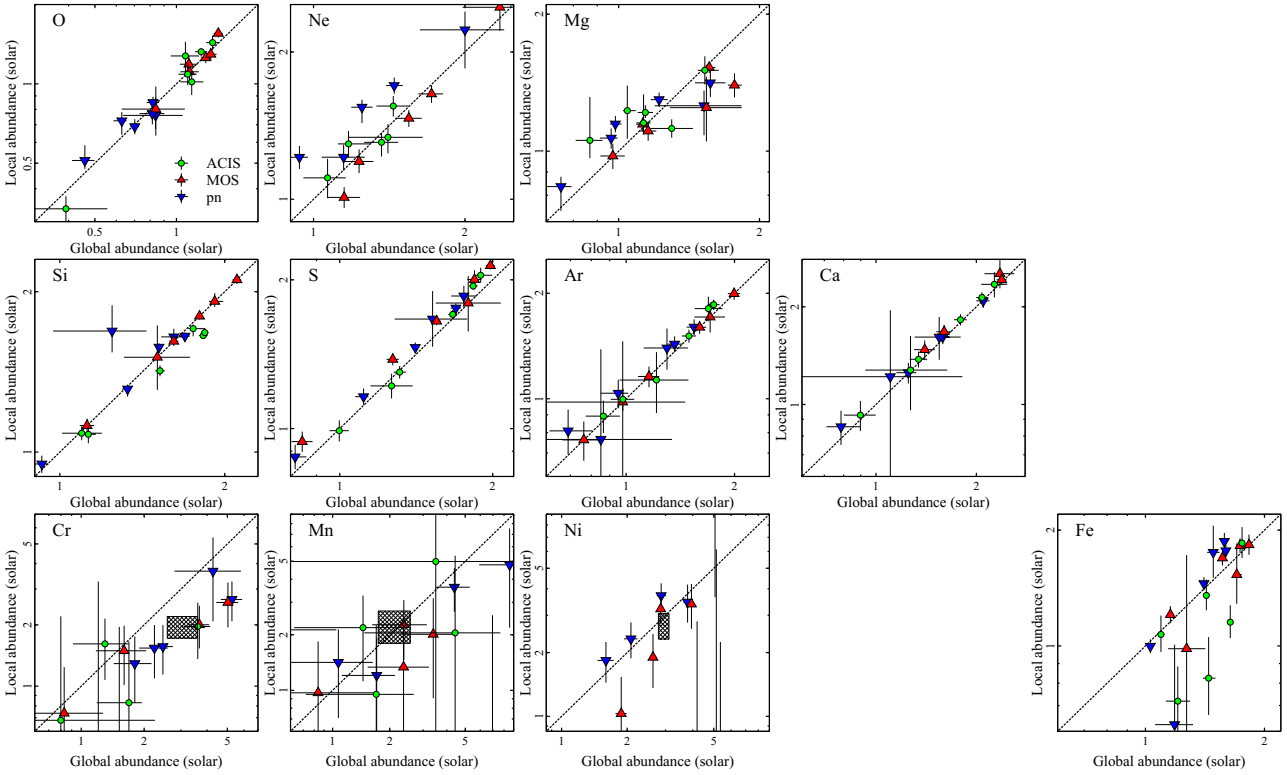

Figure 12: Comparisons of the element abundances in each annular region obtained from global fit with local one. The circle plots indicate the values with ACIS-S3, while the up- and down-triangle ones are for MOS and pn, respectively. The shaded squares for Fe-peak elements are the mean abundances of all CCDs measured in the 18–120 arcsec region.

Table 2: Best-fitting spectral parameters for the ICM emission from the global fits.

Radial range (arcsec)	$N_{\rm H}$[a] (10^{20} cm^{-2})	$kT_{\rm hot}$ (keV)	kT[b] (keV)	VEM$_{\rm hot}$[c] (10^{10} cm^{-5})	VEM$_{\rm middle}$ (10^{10} cm^{-5})	VEM$_{\rm cool}$ (10^{10} cm^{-5})	Fe (solar)	C-stat/dof
Chandra ACIS-S								
0–5	9.65[d]	2.51 ± 0.08	1.19 ± 0.14	0.5 ± 0.1	1.85 ± 0.06	1.29 ± 0.03	1.21 ± 0.09	3233.5/2935
5–18	11.9 ± 0.6	3.02 ± 0.09	1.59 ± 0.14	2.7 ± 0.3	10.0 ± 0.5	3.7 ± 0.1	1.44 ± 0.06	3690.4/3435
18–60	14.0 ± 0.2	3.05 ± 0.04	2.10 ± 0.09	31 ± 1	60 ± 1	0.88 ± 0.07	1.64 ± 0.02	4476.1/3624
60–120	13.2 ± 0.2	4.81 ± 0.12	2.9 ± 0.4	25 ± 5	94 ± 4	< 0.02	1.76 ± 0.02	4315.0/3636
120–180	13.3 ± 0.2	5.47 ± 0.22	3.3 ± 0.4	24 ± 4	87 ± 4	< 0.04	1.43 ± 0.02	4246.0/3637
180–240	14.8 ± 0.3	5.43 ± 0.09	3.6 ± 0.6	30 ± 6	59 ± 6	< 0.35	1.09 ± 0.03	4120.9/3637
XMM-Newton MOS								
0–5	8.7 ± 1.6	3.0 ± 0.3	1.5 ± 0.4	0.2 ± 0.1	0.8 ± 0.1	0.56 ± 0.08	1.27 ± 0.15	33650.7/32951
5–18	9.1 ± 0.5	3.05 ± 0.07	1.71 ± 0.12	2.7 ± 0.2	7.4 ± 0.3	2.46 ± 0.08	1.70 ± 0.05	39746.3/38544
18–60	10.3 ± 0.2	3.19 ± 0.04	2.14 ± 0.08	25.0 ± 0.8	44.7 ± 0.9	1.72 ± 0.06	1.83 ± 0.03	48983.6/45484
60–120	10.0 ± 0.2	4.10 ± 0.05	2.75 ± 0.12	39.8 ± 1.6	75.3 ± 1.7	1.0 ± 0.1	1.73 ± 0.02	52423.1/49521
120–180	9.5 ± 0.2	3.11 ± 0.03	3.10 ± 0.06	99.1 ± 0.9	0.7 ± 0.4	0.14 ± 0.04	1.57 ± 0.02	53470.1/51021
180–240	9.7 ± 0.2	3.35 ± 0.04	3.34 ± 0.17	93.1 ± 0.9	< 0.32	0.19 ± 0.05	1.16 ± 0.02	53906.0/51525
XMM-Newton pn								
0–5	9.2 ± 1.6	3.2 ± 0.3	1.5 ± 0.4	0.18 ± 0.07	0.87 ± 0.09	0.56 ± 0.09	1.19 ± 0.13	17058.5/17149
5–18	9.0 ± 0.5	3.03 ± 0.08	1.67 ± 0.14	2.6 ± 0.2	8.1 ± 0.4	2.6 ± 0.1	1.48 ± 0.06	20386.6/20754
18–60	10.4 ± 0.2	3.20 ± 0.04	2.11 ± 0.08	26.7 ± 1.0	51.3 ± 1.0	2.28 ± 0.07	1.58 ± 0.03	25294.5/24836
60–120	9.8 ± 0.1	4.17 ± 0.04	2.68 ± 0.08	35.2 ± 1.7	84.9 ± 0.4	1.44 ± 0.06	1.60 ± 0.01	26942.3/24630
120–180	9.2 ± 0.1	3.98 ± 0.02	2.95 ± 0.03	106.9 ± 0.1	1.5 ± 0.2	0.30 ± 0.03	1.41 ± 0.01	26862.7/26803
180–240	9.5 ± 0.1	3.18 ± 0.02	3.17 ± 0.02	103.4 ± 0.1	< 0.20	0.30 ± 0.04	1.03 ± 0.01	27476.0/27085
XMM-Newton RGS								
0–5	12.2[e]	3.02 ± 0.09	1.6 ± 0.8	< 6.73	22 ± 5	3.4 ± 0.6	0.58 ± 0.10	5303.1/5662
5–18	12.2	1.70 ± 0.03	1.62 ± 0.12	51 ± 2	4.0 ± 0.2	1.0 ± 0.1	1.09 ± 0.10	6799.2/6824
18–60	12.2	3.55 ± 0.08	2.3 ± 0.2	54 ± 4	114 ± 6	3.4 ± 0.4	1.39 ± 0.11	7685.8/7271
60–120	12.2	2.52 ± 0.11	2.46 ± 0.17	114 ± 4	4.8 ± 0.8	9.4 ± 0.1	1.46 ± 0.10	7585.3/7266

[a] The absorption cross sections are taken from Verner et al. (1996).

[b] The VEM-weighted average temperature.

[c] The volume emission measure (VEM) is given as $\int n_e n_{\rm H} dV/(4\pi D^2)$, where V and D are the volume of the emission region (cm^3) and the distance to the emitting source (cm), respectively.

[d] We fix this parameter to the best-fitting value.

[e] Hydrogen column density towards the Centaurus cluster taken from http://www.swift.ac.uk/analysis/nhtot/.

Table 3: Abundances of N, O, Ne, Mg, Si, S, Ar, Ca, and Fe derived from the local fits (CCDs) and the global fits (RGS) for the proto-solar values in Lodders et al. (2009).

Radial range (arcsec)	N (solar)	O (solar)	Ne (solar)	Mg (solar)	Si (solar)	S (solar)	Ar (solar)	Ca (solar)	Fe (solar)
Chandra ACIS-S (local)									
0–5	–	0.34 ± 0.08	1.34 ± 0.10	1.12 ± 0.05	1.09 ± 0.03	1.22 ± 0.07	1.13 ± 0.23	1.28 ± 0.35	0.71 ± 0.16
5–18	–	1.02 ± 0.11	2.73 ± 0.17	1.51 ± 0.11	1.70 ± 0.06	2.04 ± 0.07	1.81 ± 0.15	2.4 ± 0.2	0.8 ± 0.2
18–60	–	1.32 ± 0.05	1.31 ± 0.08	1.22 ± 0.04	1.65 ± 0.02	1.93 ± 0.03	1.86 ± 0.06	2.14 ± 0.08	1.15 ± 0.12
60–120	–	1.43 ± 0.09	1.55 ± 0.08	1.15 ± 0.18	1.68 ± 0.03	1.70 ± 0.03	1.51 ± 0.06	1.82 ± 0.07	1.85 ± 0.19
120–180	–	1.09 ± 0.10	1.30 ± 0.08	1.23 ± 0.17	1.42 ± 0.03	1.30 ± 0.04	1.00 ± 0.07	1.38 ± 0.08	1.35 ± 0.13
180–240	–	1.28 ± 0.17	1.11 ± 0.10	1.1 ± 0.3	1.08 ± 0.04	0.99 ± 0.05	0.89 ± 0.10	0.93 ± 0.10	1.07 ± 0.13
XMM-Newton MOS (local)									
0–5	–	0.80 ± 0.17	2.5 ± 0.3	1.3 ± 0.2	1.54 ± 0.14	1.8 ± 0.2	0.9 ± 0.5	< 0.60	1.0 ± 0.7
5–18	–	1.11 ± 0.09	2.87 ± 0.12	1.40 ± 0.09	2.08 ± 0.06	2.00 ± 0.09	1.81 ± 0.19	2.5 ± 0.3	1.5 ± 0.3
18–60	–	1.55 ± 0.06	1.64 ± 0.07	1.53 ± 0.04	2.03 ± 0.03	2.14 ± 0.04	2.17 ± 0.08	2.88 ± 0.10	1.83 ± 0.12
60–120	–	1.26 ± 0.06	1.01 ± 0.05	1.15 ± 0.04	1.81 ± 0.02	1.65 ± 0.03	1.72 ± 0.07	2.42 ± 0.08	1.82 ± 0.08
120–180	–	1.30 ± 0.07	1.46 ± 0.06	1.11 ± 0.05	1.59 ± 0.03	1.38 ± 0.04	1.34 ± 0.09	1.68 ± 0.08	1.69 ± 0.08
180–240	–	1.19 ± 0.09	1.19 ± 0.07	0.98 ± 0.06	1.14 ± 0.03	0.94 ± 0.04	0.97 ± 0.11	1.48 ± 0.10	1.21 ± 0.06
XMM-Newton pn (local)									
0–5	–	0.76 ± 0.13	2.2 ± 0.4	1.26 ± 0.17	1.7 ± 0.2	1.7 ± 0.2	0.8 ± 0.6	1.2 ± 0.7	0.6 ± 0.4
5–18	–	0.77 ± 0.07	2.60 ± 0.12	1.41 ± 0.10	1.65 ± 0.06	1.85 ± 0.09	1.40 ± 0.19	1.6 ± 0.3	1.8 ± 0.3
18–60	–	0.85 ± 0.04	1.22 ± 0.07	1.30 ± 0.05	1.65 ± 0.03	1.75 ± 0.04	1.60 ± 0.08	2.09 ± 0.10	1.87 ± 0.10
60–120	–	0.69 ± 0.05	1.22 ± 0.07	1.15 ± 0.05	1.55 ± 0.03	1.46 ± 0.03	1.43 ± 0.07	1.61 ± 0.08	1.77 ± 0.06
120–180	–	0.72 ± 0.08	1.71 ± 0.07	1.07 ± 0.06	1.31 ± 0.04	1.16 ± 0.05	1.04 ± 0.10	1.25 ± 0.09	1.45 ± 0.06
180–240	–	0.51 ± 0.07	1.54 ± 0.11	0.84 ± 0.10	0.95 ± 0.03	0.88 ± 0.05	0.81 ± 0.12	0.85 ± 0.10	1.00 ± 0.04
XMM-Newton RGS (global)									
0–5	0.8 ± 0.4	0.54 ± 0.09	0.42 ± 0.10	0.42 ± 0.09	–	–	–	–	0.58 ± 0.10
5–18	2.0 ± 0.5	0.93 ± 0.09	0.74 ± 0.10	0.82 ± 0.12	–	–	–	–	1.09 ± 0.10
18–60	2.3 ± 0.5	1.31 ± 0.11	0.99 ± 0.14	1.03 ± 0.12	–	–	–	–	1.39 ± 0.11
60–120	< 0.47	1.40 ± 0.15	0.76 ± 0.15	0.62 ± 0.18	–	–	–	–	1.46 ± 0.10

3.3.1.2 *RGS spectra*

We fit the high-resolution X-ray spectra of RGS with the almost same spectral model described in Sect. 3.3.1.1, considering the spectral broadening effect due to the spatial source extent using the `rgsxsrc` model with the MOS1 images. The first- and second-order spectra of each observation are fitted simultaneously. Since the astrophysical background contributions are relatively minor to the spectra of the innermost core regions, we only account for the instrumental component with a steep power-law model. We assume the line and continuum temperatures are the same because the continuum temperatures are poorly constrained with the RGS spectra. We also fix the Galactic absorption to the values estimated through the tool of Willingale et al. (2013). As shown in Fig. 13, the RGS instrument enables us rather to resolve the Ne lines from the Fe-L lines. The N Lyα emission line (~ 0.5 keV) is also prominent in the RGS spectra. Then, we allow N, O, Ne, Mg, Fe, and Ni abundances to vary, and C abundance is fixed to the solar value. The other element abundances are tied to those of the nearest lower atomic number element that can vary freely. As shown in Fig. 13, this model yields good fits with C-stat/dof ~ 1.0. The best-fitting parameters are summarized in Table 2, 3, and Fig. 13, respectively. Although each spectral extraction slice for RGS is not identical to the annulus for the CCD detectors as described in Sect. 3.2.2, the VEM-weighted average temperatures from RGS and CCDs are consistent with each other when the inner radius of the CCD region is the same as the inner cross-dispersion distance of RGS (Fig. 11).

3.3.2 *Abundance profiles*

As noted in Sect. 3.1, our main purpose is to study the central metal distribution in the Centaurus cluster. In Fig. 14, we show radial profiles of element abundances, except for the Cr and Mn ones with large statistical errors. The derived abundances of Fe and IMEs show steep negative gradients outside 60 arcsec from the cluster centre, peaks at 60 arcsec, and abrupt drops within the central 18 arcsec. In contrast, O, Ne and Mg have somewhat flatter profiles up to 120 arcsec. The discrepancies among the abundances from different detectors are significant, about a factor of two at most, especially within the Fe abundance peak. The RGS tends to give lower values of metal abundance than those from the CCDs, with a more significant abundance drop than that with CCDs. These profiles obtained from our analysis are roughly consistent with those from previous works (Panagoulia et al. 2013; Sanders et al. 2016; Liu et al. 2019; Lakhchaura et al. 2019). Moreover, our RGS analysis provides first the Ne

Table 4: Abundances of Fe-peak elements derived from the local fits (CCDs, except for Ni of ACIS) and global fits (Ni of ACIS and RGS) concerning the proto-solar values in Lodders et al. (2009).

Radial range (arcsec)	Cr (solar)	Mn (solar)	Ni (solar)
Chandra ACIS-S			
0–5	< 2.69	< 6.43	3.5 ± 0.4
5–18	< 1.52	< 3.31	4 ± 3
18–60	2.0 ± 0.6	< 1.30	3.13 ± 0.10
60–120	1.6 ± 0.5	2.2 ± 1.1	2.40 ± 0.07
120–180	< 0.30	< 0.75	2.02 ± 0.08
180–240	0.8 ± 0.6	< 0.48	1.61 ± 0.11
XMM-Newton MOS			
0–5	< 4.67	< 3.44	< 15
5–18	< 1.70	< 2.55	< 2.11
18–60	2.6 ± 0.7	2.0 ± 1.0	3.4 ± 0.8
60–120	2.0 ± 0.5	2.3 ± 0.8	3.2 ± 0.5
120–180	1.5 ± 0.5	1.3 ± 0.9	1.9 ± 0.6
180–240	0.7 ± 0.5	1.0 ± 0.9	1.0 ± 0.5
XMM-Newton pn			
0–5	< 2.38	< 3.04	< 4.16
5–18	3.7 ± 1.7	5 ± 3	< 1.99
18–60	2.7 ± 0.6	3.6 ± 1.0	3.5 ± 0.7
60–120	1.6 ± 0.4	1.2 ± 0.7	3.7 ± 0.5
120–180	1.5 ± 0.5	2.1 ± 0.7	2.3 ± 0.5
180–240	1.3 ± 0.5	1.4 ± 0.7	1.8 ± 0.4
XMM-Newton RGS			
0–5	–	–	2.2 ± 0.4
5–18	–	–	2.5 ± 0.3
18–60	–	–	2.1 ± 0.2
60–120	–	–	1.2 ± 0.3

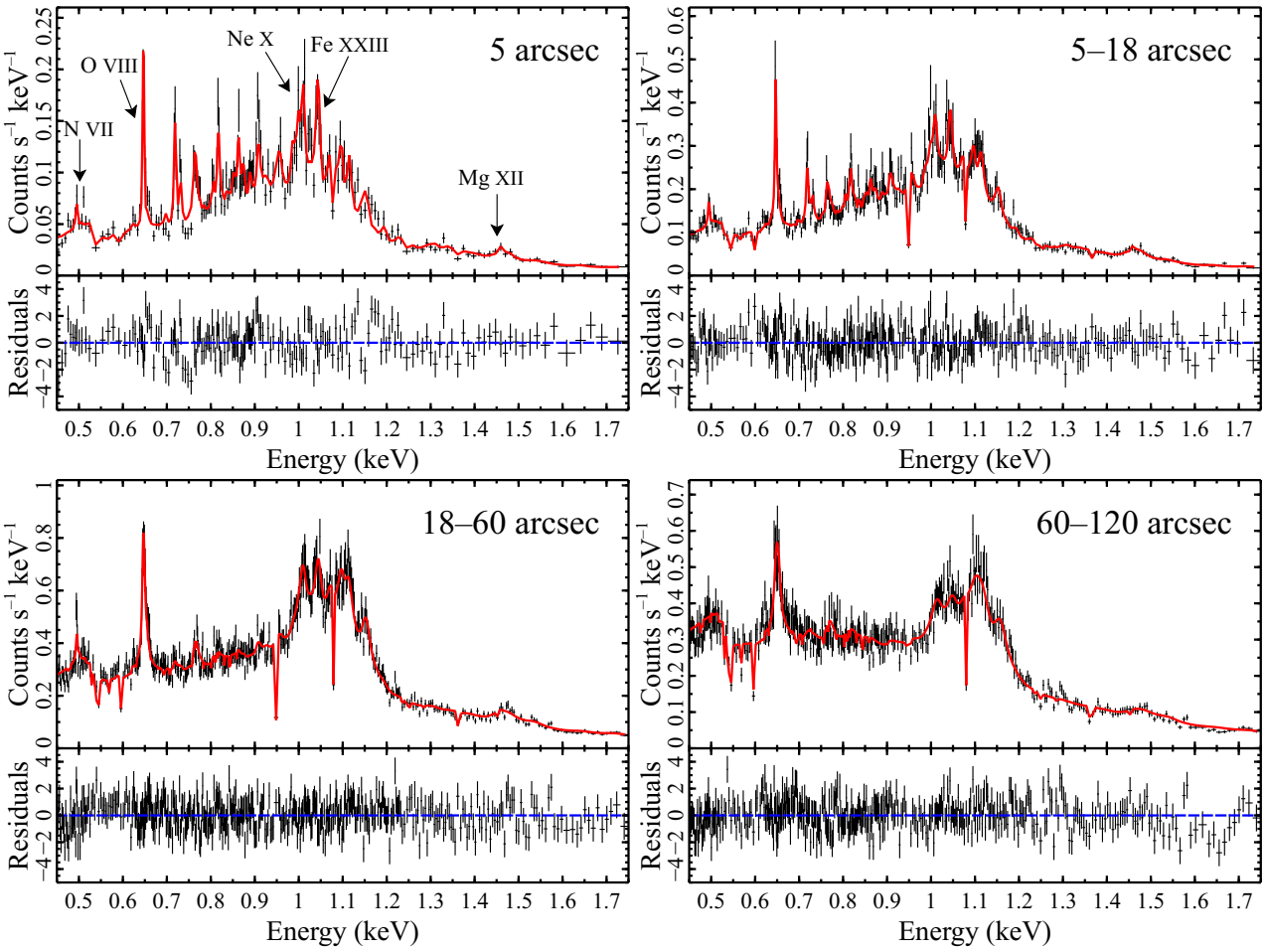

Figure 13: The RGS spectra extracted from each cross-dispersion slice. The black points indicate the data from the observation in 2007 and the red lines are the best-fitting model summarized in Table 2 and 3, where only the first-order spectra are shown for clarity. Several emission line structures are marked on the top left panel.

abundance profile showing a similar drop with Fe, although there had been no hint of declination of the Ne abundance from works with CCD data (Liu et al. 2019).

As shown in Fig. 15, the abundance ratios to Fe (X/Fe) show flat distributions while the S/Fe, Ar/Fe, and Ca/Fe ratios enhance in the central 60 arcsec by a few tens of per cent compared to those beyond 120 arcsec. The scatters in the X/Fe ratios among the different detectors are much smaller than those in absolute abundance. Exceptionally, RGS and CCDs yield significantly different Ne/Fe ratios. Given that the Ne-K lines are blended in the Fe-L bump with CCDs as mentioned in Sect. 3.3.1.1, we expect RGS to provide more reliable Ne/Fe estimation. The O/Fe ratios for MOS, which are about a factor of two higher than the pn values with a slightly better energy resolution than pn, are globally consistent with those derived from the RGS spectra. Therefore, for CCSN products of O, Ne, and Mg to some extent, we will discuss the results only with the RGS data, which would give a better estimation of these abundances thanks to its high spectral resolution. The Ca/Fe ratios among the CCD detectors show differences of up to ~ 50 per cent, while the other IMEs/Fe ratios are consistent with each other.

3.3.3 Systematic uncertainties

Some systematic uncertainties possibly give biases in abundance measurements in cool cores (e.g., Werner et al. 2008). For example, simple temperature modelling to a complex structure in the centres will lead to underestimation of abundances, especially when fitting the spectra with strong Fe-L lines (e.g., Buote & Canizares 1997; Matsushita et al. 2003). Therefore, we also estimate the abundances using other temperature structure models; two and four CIE components. For the four-CIE model, the temperature of the coolest component is half of that of the second coolest one, adjusting the temperatures of this model to be a geometric sequence with a common ratio of 0.5. Even for the innermost region, these models give almost consistent Fe abundances with those derived in the previous subsection with several per cent. Since the quadruple temperature model yields unreasonably low VEM for one component (< 1 per cent of the other three) and almost the same C-statistic values, we conclude that the three temperature-components model is sufficient to reproduce the emission from the Centaurus core.

Projection of X-ray emission along the line of sight could also obscure the actual distribution of temperature or abundances. Since the Centaurus cluster core deviates from the spherical symmetry due to the plume-like structure, we do not apply the

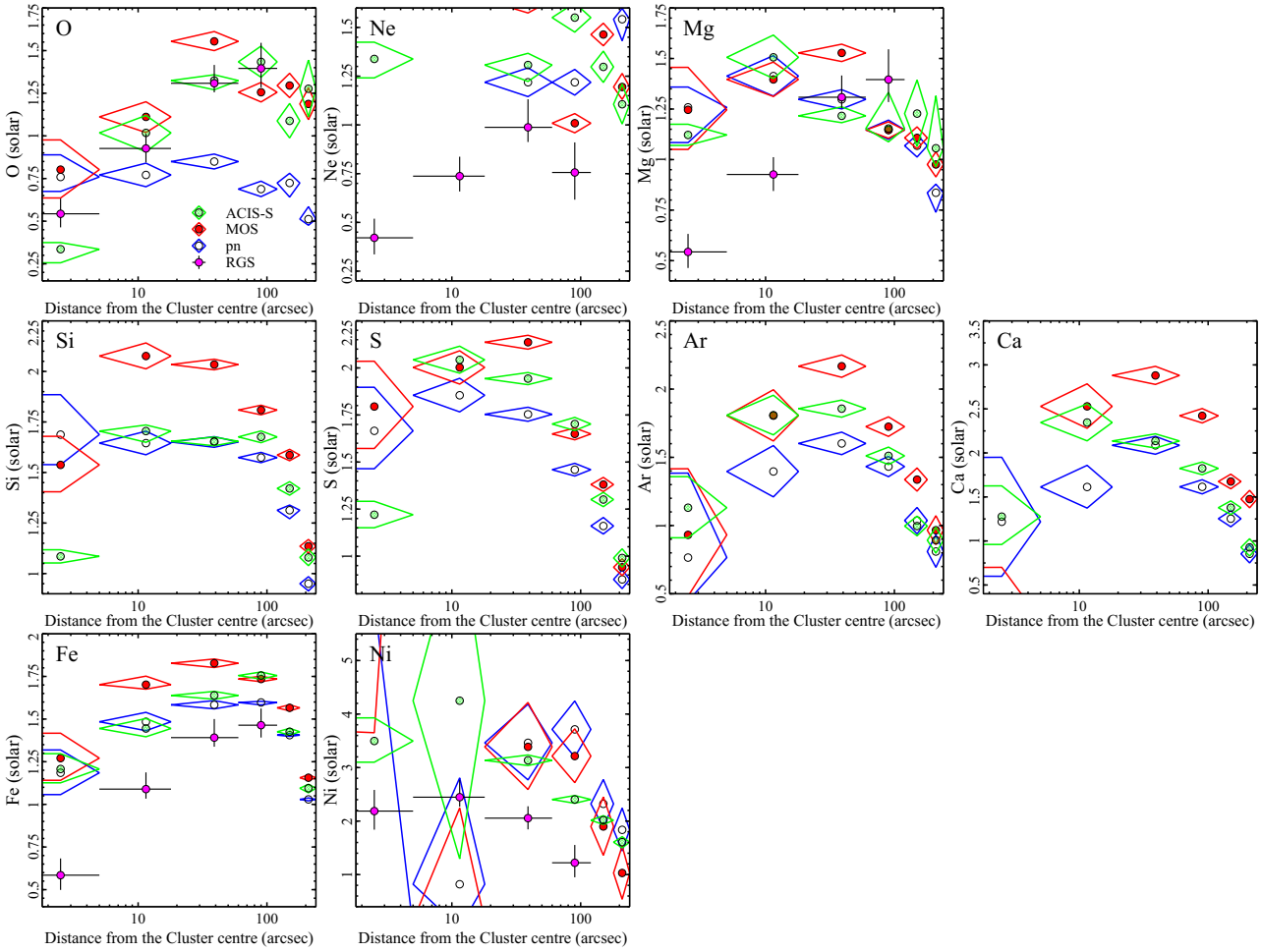

Figure 14: Radial profiles of the metal abundance (O, Ne, Mg, Si, S, Ar, Ca, and Fe) obtained from a triple CIE modelling. The green-, red-, and blue-diamond plots are for results with *Chandra* ACIS-S, *XMM-Newton* MOS, and pn, respectively. The magenta plots indicate the RGS results of O, Ne, Mg, Fe, and Ni. We plot the Ne abundance setting the y-axis range according to values with RGS for clarity.

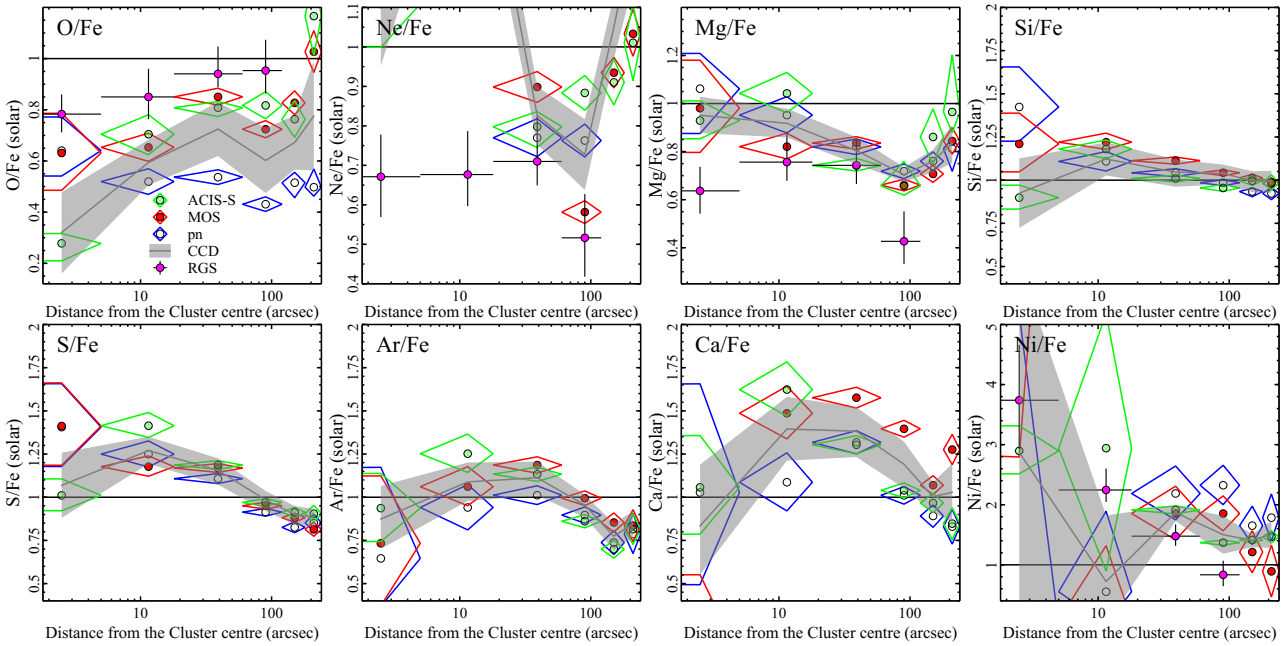

Figure 15: Radial profiles of the relative abundance ratios to Fe obtained from a triple CIE modelling. The diamond markers follow the same manner as Fig 14. The shaded areas indicate the mean values among three CCD detectors. We also show the solar ratio with solid lines on each panel.

deprojection method often used to analyse the X-ray emission from cluster cores (e.g., Ettori 2002; Ikebe et al. 2004; Russell et al. 2008). Instead, we fit the innermost spectra using a sextuple-CIE model. Here, we first fit the spectra of the outermost bin, or 180–240 arcsec region, with a single-CIE model. Then, we fit the spectra of 120–180 arcsec region with a two-CIE model, where one CIE component has the same temperature and metal abundances as those at the outermost region. Finally, we fit the innermost spectra using a sextuple-CIE model. Then, we get almost the same metal abundances within 10 per cent as those with the three-component CIE model.

Next, in order to study the uncertainties caused by systematics in the atomic data, we fit the spectra of the MOS and RGS with the SPEXACT version 3.06.01 (Kaastra et al. 1996). We plot the derived abundances and relative abundance ratios to Fe with AtomDB and SPEXACT in Fig. 16. We do not report the results for Ne in Fig. 16(a) because the Ne-K lines are blended into the Fe-L complex in CCD spectra. With the MOS data, the latest version of SPEXACT gives almost the same abundances, except for the O abundances. The fitting results of RGS spectra with SPEXACT yield nearly constant metal abundances in the core, which is significantly different from those with AtomDB (Fig. 16(b)). On the other hand, the RGS abundance ratios are mostly consistent between both atomic codes in a few tens of per cent for all elements (Fig. 16(c)). The differences of ~ 20 per cent in the O/Fe ratios and Ne/Fe

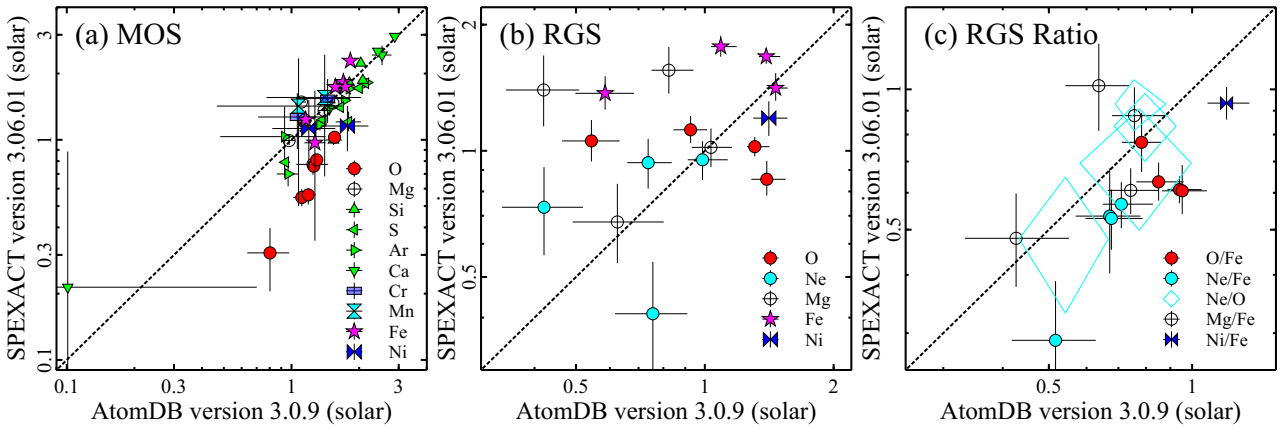

Figure 16: (a) A comparison of the metal abundance (O, Mg, Si, S, Ar, Ca, Fe, Cr, Mn, and Ni) in each annular region of the MOS data with AtomDB version 3.0.9 and SPEXACT version 3.06.01. The Ne abundance is absent in the plots for its unreliability (see Sect. 3.3.2). For the Cr, Mn, and Ni abundance, we show the averaged values on the central < 120 arcsec core and the outer 120–240 arcsec region. (b) Same as (a) for O, Ne, Mg, Fe, and Ni taken from the RGS data. (c) A comparison of the relative abundance ratios for O/Fe, Ne/Fe, Ne/O, Mg/Fe, and Ni/Fe obtained from the RGS data. The dotted lines shown in each panel indicate the equal value between the two codes.

ratios between AtomDB and SPEXACT may be caused by systematic uncertainties in the calculation of the Fe-L lines. We note that the Ne/O ratios with RGS from SPEXACT and AtomDB agree with each other.

3.4 Discussion

3.4.1 Abundance measurements in the innermost regions

As described in Sect. 3.1, the mechanisms of the abundance depletions reported in some cluster cores are still under discussion. We detect abrupt abundance drops within central 18 arcsec for most elements. Panagoulia et al. (2013) and Lakhchaura et al. (2019) proposed that these drops arise from significant metal storage into cool dust grains in the cluster centre. If this is the case, we expect that the abundance of noble gases, rarely forming dust grains, show no central drop. Lakhchaura et al. (2019) reported that only the Ar/Fe ratio in the Centaurus core slightly increases towards the centre in different to the Ar abundance still showing a central drop as other metals. Hence, they concluded that the drops are due to the incorporation of metals into dust grains. Our Ar/Fe profile from the longer exposure data also shows a slight increase to around 60 arcsec from 120 arcsec, which is consistent within error bars with that derived by Lakhchaura et al. (2019). However, we get a flat Ar/Fe profile within $\lesssim 60$ arcsec where the abundance drop is reported (Fig. 15). We note that the increasing profile of the Ar/Fe ratio by Lakhchaura et al. (2019) is partially attributed

to their region selection with $\lesssim 30$ arcsec for the innermost bin. This larger radius than ours is suitable for *XMM-Newton*, and probably makes a too much concession to the extremely high angular resolution of the *Chandra* ACIS (~ 0.5 arcsec), possibly obscuring the accurate innermost metal profile for a trade-off of photon statistics. Our Ar/Fe profile is quite similar to that of the Ca/Fe ratios even though Ca will be easily trapped in dust. In addition, we find that the Ne/Fe profile using RGS is also flat towards the centre. These results do not support the efficient metal storage to dust and the dust grains scenario as the origin of abundance drops.

The different detectors and plasma codes lead to significantly inconsistent elemental abundances; at the same time, the discrepancies in the abundance ratios are relatively small. To investigate the origin of these schisms, we fix the Fe abundance at the peak value (~ 1.7 solar at 60–120 arcsec) and re-fit the spectra of the innermost region (< 5 arcsec) for RGS and MOS spectra. As shown In Fig. 17, this high-Fe abundance model reproduces the continuum and most of the line emissions for both AtomDB and SPEXACT, yielding similar abundance ratios. With AtomDB, the derived C-stat/dof for the RGS spectrum, 5363.8/5663, is larger than 5303.1/5662 with the best-fitting Fe abundance at 0.58 solar. This worse C-statistic value is possibly caused by residual structures at 1.1–1.2 keV energy band, rather than the difference in the equivalent width of lines. As shown In Fig. 17, SPEXACT does not show such residual structures which yields the best-fitting Fe abundance of 1.4 solar at the innermost region. When we exclude the 0.9–1.2 keV bandpass where the abovementioned schism between the two codes is exhibiting, the derived Fe abundance with AtomDB becomes 1.2 ± 0.3 solar. This value mostly converges to that with SPEXACT and also that with MOS data; the Fe abundance with MOS data under the same excision is not significantly changed. Thus, while the Fe abundance drop is not dissolved completely, quite a sharp drop with RGS data could be attenuated. The disagreement between the latest version of AtomDB and SPEXACT occurs for Fe XXIII and Ne X emission lines around 1.2 keV. These deficits around this energy band have been reported since *ASCA*, especially in luminous X-ray sources, such as binaries or SN remnants (e.g., Brickhouse et al. 2000; Katsuda et al. 2015; Nakano et al. 2017). We also fit the RGS and MOS spectra at the 60–120 arcsec region in the same way, fixing the Fe abundance at 0.5 and 1.7 solar. Then, as seen in the bottom-right panel of Fig. 17, the low-Fe abundance models cannot reproduce the line strength of the Fe Heα line at 6.7 keV.

The systematic uncertainties of abundances from ~ 1 keV plasma have been discussed (e.g., Arimoto et al. 1997; Matsushita et al. 1997, 2000; Mernier et al. 2020;

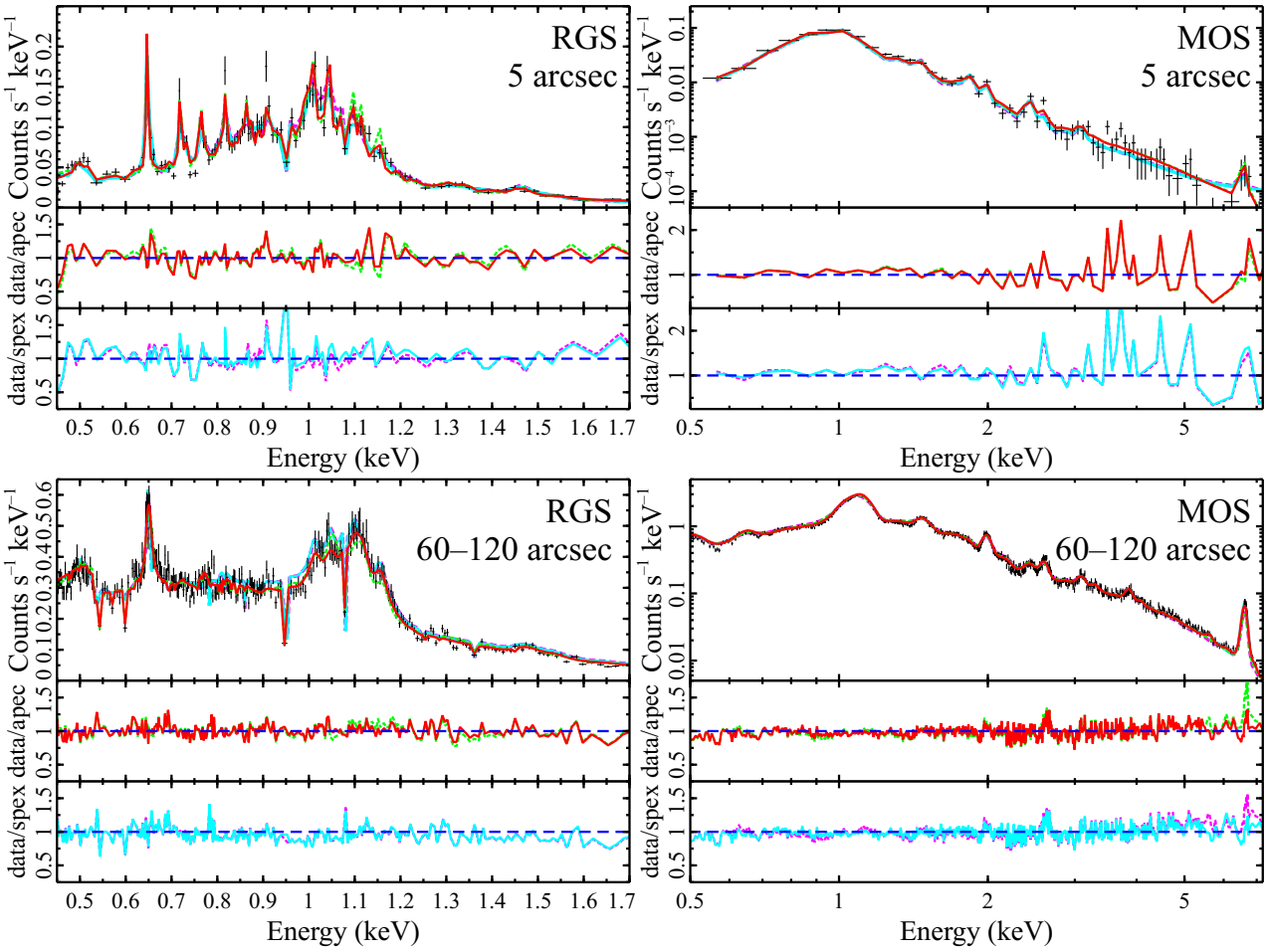

Figure 17: A comparison of two models and atomic codes. The spectra at the innermost region and at the peak of the Fe abundance are plotted for RGS and MOS. The red solid line represents the best-fitting model (Fe $\sim$ 0.5 solar at $<$ 5 arcsec, Fe $\sim$ 1.7 solar at 60–120 arcsec) with AtomDB and the green dotted one is for the fixed Fe abundance model (Fe = 1.7 solar at $<$ 5 arcsec, Fe = 0.5 solar at 60–120 arcsec), respectively. The cyan solid and magenta dotted lines follow the same plotting manner but using SPEXACT, where the best-fitting and peak Fe abundances are 1.4 and 1.7 solar, respectively. We also plot the divided data by each model, where data/apec is for the results with AtomDB and data/spex is for SPEXACT.

Gastaldello et al. 2021). The two-photon and free-bound emissions contribute to the continuum, especially for the lower-temperature plasma in the innermost regions. Spectral fits try to reduce C-statistics for the lower energy band with high statistics, where the line emissions dominate the continuum. Then, minor systematic uncertainties in the atomic data and/or in the response matrices will bias the abundance measurement. The local fits around the Fe Heα line, whose atomic data is expected to be much more reliable than those for Fe-L lines, also lead to abundance drops. This is because the abundances of the other elements are fixed to the best-fitting values from the global fits. For example, when we fix the α-element abundances at 1.3 solar, the local fits for the *Chandra* < 5 arcsec region gives 1.1 solar for the Fe abundance. Thus, measurements of absolute abundances are challenging, especially in the very core gas, where the abundance drops are reported. In the hot outer regions with the prominent Fe-K line, absolute abundances are more reliable. In contrast, the abundance ratios are determined from the ratios of line strengths. As a result, the two atomic codes and different CCDs yield more consistent abundance ratios than the absolute abundances.

3.4.2 Abundance pattern of the Centaurus cluster core

We plot the absolute and relative abundance pattern in the ICM of the Centaurus core (Fig. 18(a) and (b)). Here, we use the weighted average abundances within (< 18 arcsec) and outside (18–120 arcsec) the abundance drop region. Outside the drop region, the metal abundances from N to Ni are over-solar values, consistent with previous X-ray studies (e.g., Matsushita et al. 2007; Takahashi et al. 2009; Sakuma et al. 2011; Sanders et al. 2016). These abundances are systematically larger than those observed in the Perseus cluster core with *Hitomi* (Simionescu et al. 2019), other cool-core systems including groups (Mernier et al. 2018c), and early-type galaxies (Konami et al. 2014). The statistical uncertainties in the Cr, Mn, and Ni abundances are comparable to those of the Perseus cluster core (Mernier et al. 2018c; Simionescu et al. 2019). As shown in Fig. 18(b), the abundance ratio pattern in the Centaurus core is largely consistent with the solar composition, those of other cool-core systems, and early-type galaxies (e.g., Mernier et al. 2018c; Simionescu et al. 2019; Konami et al. 2014). The exceptions are the high Ni/Fe ratio, about 1.5–2 solar, with RGS and CCDs, high N/O ratio at 1.5 solar, and low Ne/Fe and Mg/Fe ratios at 0.6 solar with RGS.

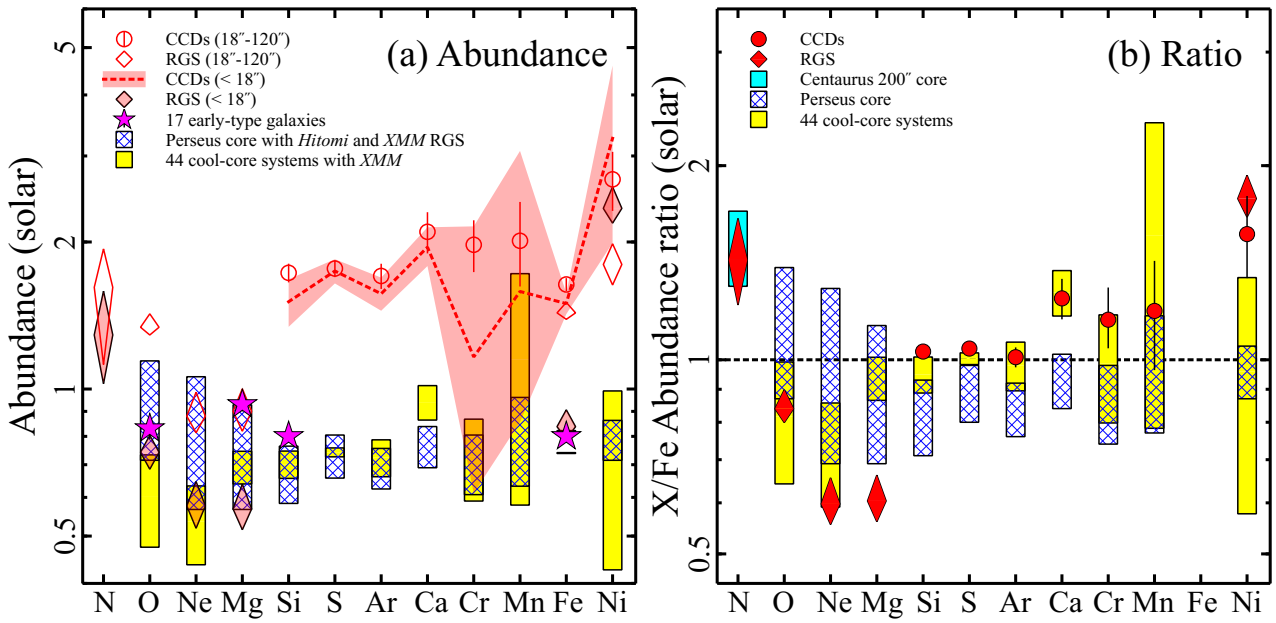

Figure 18: (a) Abundance pattern measured in < 18 arcsec and 18–120 arcsec region of the Centaurus cluster. The open circle and diamond plots show the results of 18–120 arcsec region derived from CCDs and RGS, respectively. The shaded area and filled diamonds are from the central 18 arcsec core with CCDs and RGS, respectively. For comparison, we plot the patterns in the ICM from other works, where the star plots are from 17 early-type galaxies (Konami et al. 2014), the blue boxes are from the Perseus cluster (Simionescu et al. 2019), and the yellow boxes are from 44 cool-core clusters, groups, and ellipticals (CHEERS sample; Mernier et al. 2018c). (b) Abundance ratio pattern obtained from the central 120 arcsec core in the same manner as the left. The cyan box indicates the N/Fe ratio in the Centaurus cluster from Mao et al. (2019), while the blue and yellow boxes are from Simionescu et al. (2019) and Mernier et al. (2018c).

Table 5: Best-fitting combination of CCSN and SN Ia yield models by number to the abundance ratio pattern observed in the core of the Centaurus cluster.

SN type	Model (Reference)	All elements	Excluding Ne, Mg, and Ni
near-$M_{\rm Ch}$ SN Ia	W7 (Leung & Nomoto 2018)	0.10 ± 0.03	0.08 ± 0.04
sub-$M_{\rm Ch}$ SN Ia	double detonation (Shen et al. 2018)	0.06 ± 0.04	0.11 ± 0.06
CCSN	N20 (Sukhbold et al. 2016)	0.84 ± 0.03	0.82 ± 0.04
	χ^2/dof	11.2/8	7.2/5
near-$M_{\rm Ch}$ SN Ia	W7	0.03 ± 0.02	0.02 ± 0.01
sub-$M_{\rm Ch}$ SN Ia	double detonation	0.04 ± 0.02	0.04 ± 0.02
CCSN	classical (Nomoto et al. 2006)	0.93 ± 0.02	0.94 ± 0.02
	χ^2/dof	17.8/8	9.9/5

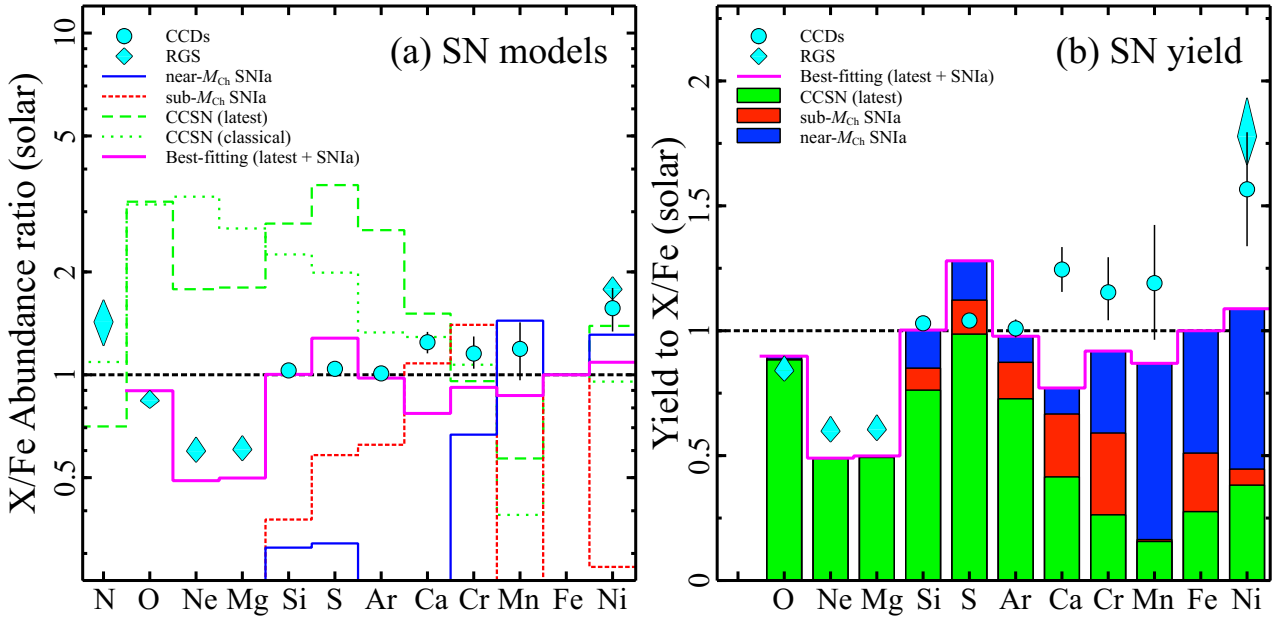

Figure 19: (a) Comparison of the abundance ratio pattern same as Fig. 18(b) with SN nucleosynthesis models. The thin solid, dotted, dashed, and dot-dashed lines represent the relative abundance ratios to Fe for near-$M_{\rm Ch}$ SN Ia (Leung & Nomoto 2018), for sub-$M_{\rm Ch}$ SN Ia (Shen et al. 2018), for latest CCSN (Sukhbold et al. 2016), and "classical" CCSN (Nomoto et al. 2006), respectively. The magenta thick line corresponds to the best-fitting model which assumes a linear combination of the SN Ia and CCSN models. (b) The contribution of each type of SNe to the best-fitting ratio pattern.

3.4.2.1 Contributions from different SN yield models

We test a linear combination of recent SN nucleosynthesis calculations to reproduce the abundance ratio pattern from the O/Fe to Ni/Fe observed in the Centaurus core. We adopt the latest update of the W7 model from 2D hydrodynamical simulations (Leung & Nomoto 2018, for near-$M_{\rm Ch}$ SN Ia) and a double-degenerated double-detonation explosion of a solar mass and solar metallicity white dwarf (Shen et al. 2018, for sub-$M_{\rm Ch}$ SN Ia). A recent yield of exploding massive stars averaged over Salpeter's initial mass function (Salpeter 1955) calibrated using observed energy of SN 1987A (the N20 model, Sukhbold et al. 2016) and the "classical" model of Nomoto et al. (2006) are chosen for CCSN yield models. These model predictions are plotted in Fig. 19(a) with the observed abundance ratios. To fit the pattern and calculate χ^2, we take not only the statistical errors of the observed abundance ratios but also 20 per cent systematic uncertainties into account, reflecting the differences between the derived abundance ratios from AtomDB and SPEXACT. Table 5 summarizes the fitting results with the contributions of each SN type to the total number of SNe. The N20 model by Sukhbold et al. (2016) systematically gives a smaller χ^2 than the "classical" model by Nomoto et al. (2006). Since the Ne/Fe, Mg/Fe, and Ni/Fe ratios

deviate from the best-fitting pattern even using the N20 model, we excluded Ne, Mg, and Ni and re-fit the abundance pattern in the same way. Then, we get a better χ^2, and the contributions of each SN model are consistent within the error bars. The ratio of the numbers of CCSN to the total number of SNe is about 80 per cent with the N20 model, while it is about 90 per cent with the "classical" model. This result is consistent with those for the other clusters (e.g., Simionescu et al. 2015, 2019). Figure 19(b) shows the contributions of CCSN, sub-$M_{\rm Ch}$, and near-$M_{\rm Ch}$ SNe Ia to each element for the best-fitting combination with the N20 model.

3.4.2.2 Abundance pattern of α-elements

Figure 19(b) shows that O, Ne, and Mg are predominately produced by CCSNe. The differences between the observed O, Ne, and Mg abundance pattern and predicted yields by CCSN models lead to the large χ^2 in Table 5. The observed O, Ne, and Mg abundance pattern, lower Ne and Mg abundances compared to the O abundance, resembles that of the latest N20 model by Sukhbold et al. (2016) rather than the "classical" calculation by Nomoto et al. (2006). Figure 19(b) depicts that Si, S, and Ar are mostly synthesized by CCSNe. The combination with the N20 model, near- and sub-$M_{\rm Ch}$ roughly reproduces the observed abundance pattern of these elements and Fe. The SNe Ia contribution is higher to Ca than those for the other IMEs while the observed Ca/Fe ratio is still higher than the best-fitting prediction.

3.4.2.3 Abundance pattern of Fe-peak elements

The observed Cr/Fe and Mn/Fe pattern is explained by a combination of CCSNe, near-$M_{\rm Ch}$ SNe Ia, and sub-$M_{\rm Ch}$ SNe Ia, as was the Perseus cluster core. The Fe-peak elements are dominantly forged by SNe Ia, especially in the hottest layers of the exploding white dwarf (e.g., Seitenzahl et al. 2013a). In particular, ^{55}Mn is an important isotope since SNe Ia much more produces it than CCSNe relative to Fe (Kobayashi & Nomoto 2009), while the Cr/Fe and Ni/Fe ratios are less independent of the SN Ia/CCSN contributions. As shown in Fig. 19(a), the CCSN models predict the Mn/Fe ratios as approximately half of the solar ratio. The observed solar Mn/Fe ratio in the Centaurus core and other systems indicates a significant contribution of SNe Ia to the Fe-peak element production. The updated hydrodynamical simulations (e.g., Leung & Nomoto 2018) anticipate that the extremely high-density core of near-$M_{\rm Ch}$ SNe Ia synthesizes a higher fraction of neutronized isotopes like ^{55}Mn and ^{58}Ni than sub-$M_{\rm Ch}$ ones. This prediction is confirmed by observational studies on

SN Ia remnants (e.g., Yamaguchi et al. 2015; Ohshiro et al. 2021). The observed solar Mn/Fe ratio indicates a significant contribution from near-$M_{\rm Ch}$ SNe Ia. The observed Cr/Fe ratio is close to the solar ratio as in other cool-core systems (e.g., Mernier et al. 2018c). When fitted with a model of either near-$M_{\rm Ch}$ SN Ia or sub-$M_{\rm Ch}$ SNe Ia together with a contribution of CCSNe (N20), the χ^2/dof value becomes 14.3/9 and 26.2/9, respectively, favouring both progenitor types of SN Ia substantially contributing to the enrichment. Hence, the contribution of the sub-$M_{\rm Ch}$ SNe Ia is needed to explain the observed solar Cr/Fe and Mn/Fe patterns.

Although we use the latest atomic code revised after the *Hitomi* observations of the Perseus core, the observed Ni/Fe ratios of the Centaurus cluster, 1.5–2 times the solar ratio, are still higher than the solar composition of the Perseus cluster (Simionescu et al. 2019) and the 44 cool-core systems (Mernier et al. 2018c). Our Milky Way requires both CCSN and SN Ia to produce Ni in the same way as Fe since the Ni/Fe ratio of stars is ~ 1 independent of the Fe abundance (Feltzing & Gustafsson 1998; Gratton et al. 2003). The observed high Ni/Fe ratio suggests that Ni synthesis in the Centaurus cluster core might be different from that in our Galaxy. Note strongly that both Ni-L and K lines are blended into the Fe-L lines and Fe Heβ line at 7.9 keV, respectively, with CCD detectors, and the derived Ni abundances will be affected by some systematics.

3.4.2.4 Origin of nitrogen

We also detected the N emission line with RGS within $R_{\rm e}$ of NGC 4696. The weighted average of the observed N/O ratio is $\sim$ 1.5–2 solar in the central 60 arcsec region. As shown in Fig. 19(a), the CCSN nucleosynthesis models predict that the N/O ratio is much less than the solar value. Different from other light α-elements such as O and Mg, the N abundance in the cool cores of some galaxy clusters and groups, or in early-type galaxies shows super-solar values, implying strong contamination by stellar mass loss from asymptotic giant branch (AGB) stars exhibiting in these systems (e.g., Sanders et al. 2008; Mao et al. 2019; Mernier et al. 2022). Figure 20 compares the observed N/O ratio and the yields expected in AGB stars by Karakas (2010). The observed value is consistent with the calculations assuming AGB stars with less massive (1–2 $M_\odot$) and the initial solar metallicity. Thus, the observed N/O ratio indicates the importance of mass loss from low-mass AGB stars in the BCG.

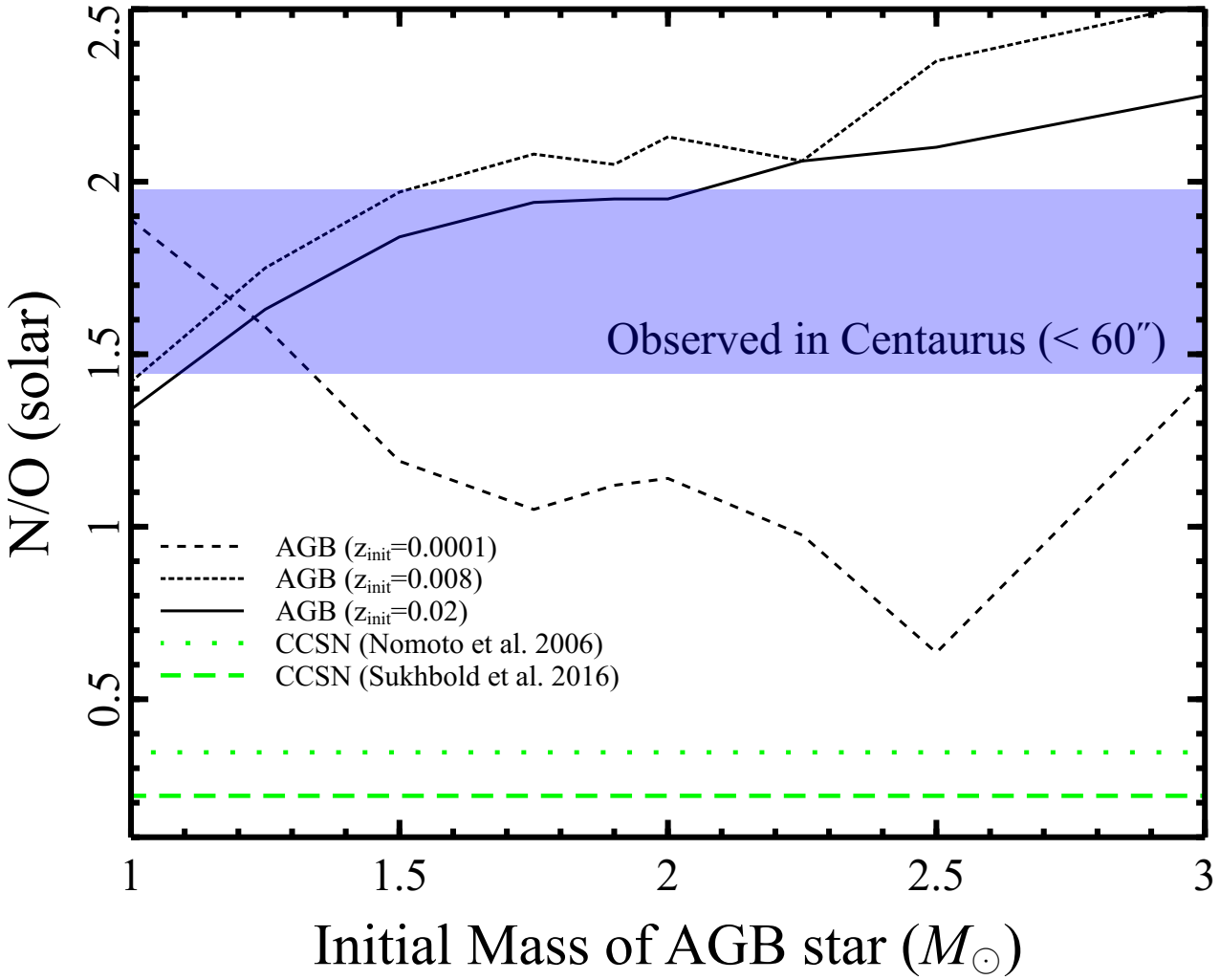

Figure 20: The N/O ratio from AGB stars as a function of initial mass compiled from Karakas (2010), assuming models with several initial metallicity. The shaded area indicates the observed N/O value with RGS in the central 60 arcsec core of the Centaurus cluster. The CCSN yields from Nomoto et al. (2006) and Sukhbold et al. (2016) are also plotted for comparison.

3.4.3 *Comparison with the stellar metallicity profiles*

In a cool core, mass-loss winds from AGB stars and SNe Ia from the BCG enrich the ICM continuously (see Sect. 3.1). The former supplies lighter metals trapped in stars, which were formed from the ISM enriched by early SNe, and the latter, exploding white dwarfs, pollutes the ICM with heavy Fe-peak elements.

In Fig. 21, we plot the stellar metallicity profiles of NGC 4696 given by Kobayashi & Arimoto (1999) and the average profiles of stars observed in early-type galaxies scaled with R_e by Kuntschner et al. (2010). Here, we adopt $R_e \sim 85$ arcsec of NGC 4696 (Carollo et al. 1993), and convert the metallicities to abundances using the proto-solar values of Lodders et al. (2009). The stellar metallicity of galaxies generally increases towards the centre (Carollo et al. 1993). Around the effective radii, the stellar metallicity of α-elements of these galaxies are typically close to the solar value. It is cautious that the accurate metallicity is possibly different by a factor of two because of large uncertainty and poor understanding of the estimate of the metallicity of Mg and Fe from strength and depth of their optical absorption lines (Kobayashi & Arimoto 1999). Figure 21 also compares the Mg and Fe profiles in the ICM of the Centaurus cluster derived from the RGS observations to the stellar metallicity profiles of these metals. As described in the previous subsection, at R_e of the BCG, the accurate abundances are more reliable than the innermost regions. We found that the Mg abundances obtained from X-ray measurements around R_e are consistent with the stellar Mg metallicity. At the inner regions, if we adopt the high-Fe abundance model without the abundance drop described in Sect. 3.4.1, i.e. the model with Fe ~ 1.7 solar, the Mg abundances with AtomDB and SPEXACT increase to ~ 1 solar, and becomes largely consistent with the stellar metallicity as shown in Fig. 21.

When integrating the electron density calculated from the VEM profile out to 120 arcsec, the hot gas mass is derived to be $7{\times}10^{10}\,M_\odot$. This mass is orders of magnitude higher than those in early-type galaxies. For example, the gas mass of a massive elliptical galaxy NGC 1404 is only $\sim 7 \times 10^8\,M_\odot$ (Mernier et al. 2022). Adopting the K-band luminosity [19] of NGC 4696 is $1.8{\times}10^{12}\,L_\odot$ [20], this gas mass is about 4 per cent of the stellar mass of the BCG, where stellar mass-to-light ratio with K-band of giant early-type galaxies are around unity (e.g., Nagino & Matsushita 2009). Given that stars have lost 10–20 per cent of the initial mass

[19] The K-band is a window centred on 2.2 μm.

[20] Retrieved from Hyperleda: http://atlas.obs-hp.fr/hyperleda/

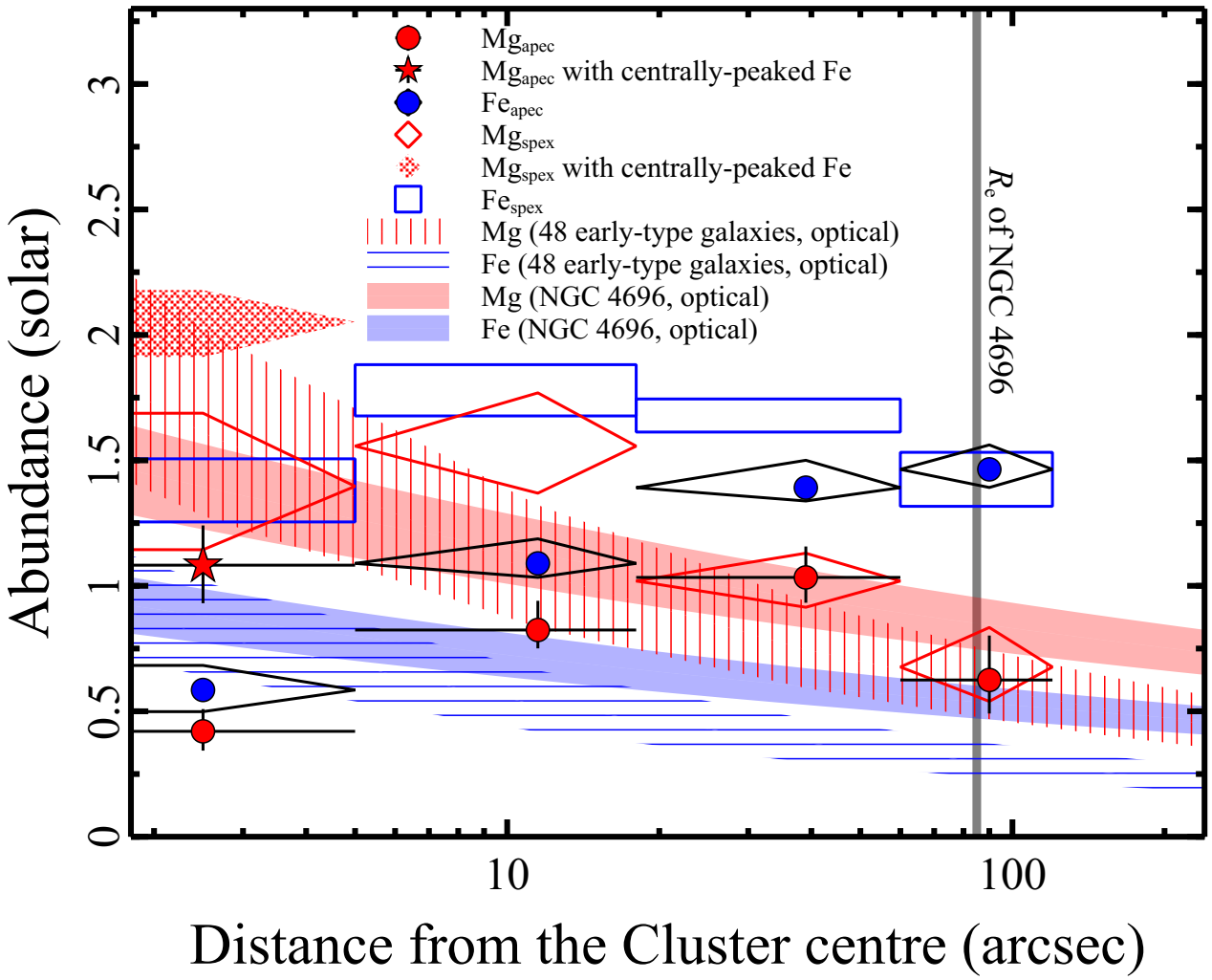

Figure 21: The abundance profile of Mg (red) and Fe (blue) overlaid with the stellar metallicity observed in early-type galaxies (hatched strips, Kuntschner et al. 2010) and NGC 4696 (shaded strips, Kobayashi & Arimoto 1999).

via mass-loss winds over the Hubble time (e.g. Courteau et al. 2014; Hopkins et al. 2023), the accumulating time of the mass loss of NGC 4696 may be much longer than those of early-type galaxies while early mass-loss products would have been lost. Assuming the star formation epoch, for instance, at 2.5 Gyr ($z \sim 2.5$, the peak star formation is at $z = 2$–3, e.g., Madau et al. 1996; Brandt & Hasinger 2005), the time to congregate the observed ICM mass in the central 120 arcsec region is about 9–10 Gyr. Here, the injection rate of stellar winds from Ciotti et al. (1991) is $\sim 1.3\,(t/t_{\rm now})^{-1.3}\,{\rm M}_\odot\,{\rm yr}^{-1}$ in NGC 4696. We found no significant change in this estimated time when choosing different star formation epochs $z = 2$ or $z = 3$. Such a long time could strongly overestimate the gas mass in normal early-type galaxies (e.g., Mernier et al. 2022). Since we compare abundances in stars and ICM which have experienced very different histories, the actual enrichment time may change from our simple or simplistic calculation. For the other clusters with more luminous cool cores, with higher ICM masses and lower metal abundances, it may be difficult to explain the observed α-elements peak with stellar mass loss only (e.g. de Plaa et al. 2006; Simionescu et al. 2009; Mernier et al. 2017).

3.4.4 Fe mass and SN Ia rate

While the entire gas mass in the Centaurus core can be accounted for by the mass ejection via stellar winds (see Sect. 3.4.3), how about the masses of each element, especially of Fe? As shown in Fig. 21, the Fe abundances in the ICM are higher than the stellar Fe metallicity, particularly around $R_{\rm e}$ of the BCG where the absolute abundances are reliable. In addition, the Mg/Fe ratios in the ICM are also different from the super-solar α/Fe ratios of stars in giant early-type galaxies (e.g., Kobayashi & Arimoto 1999; Kuntschner et al. 2010). These results strongly suggest the additional and late enrichment of Fe by SNe Ia. Then, the Fe abundances in the ISM can constrain the past metal supply by SNe Ia. Adopting the stellar Fe metallicity ~ 0.5 solar, the SN Ia contribution accounts for the Fe abundance ~ 1 solar. From the obtained electron density and Fe abundance profiles, the total Fe mass from SNe Ia in the ICM out to 120 arcsec is estimated as $(1.1 \pm 0.2) \times 10^8\,{\rm M}_\odot$. We note that the Fe mass ejected from the stellar population with the metallicity in Fig. 21 is about $6 \times 10^7\,{\rm M}_\odot$ which is a factor of two lower than the observed Fe mass.

The present metal supply by SNe Ia will be studied using the Fe abundance of the ISM in early-type galaxies. The mass of the hot ISM in giant early-type galaxies is typically less than 1 per cent of stellar mass and the timescale for the enrichment of

the hot ISM is smaller than ~ 1 Gyr (Matsushita 2001). At a given epoch, the absolute abundance of Fe contributed by SNe Ia is estimated by

$$M^{\rm Fe}_{\rm SN\ Ia} \frac{\theta_{\rm SN\ Ia}}{\alpha_* z^{\rm Fe}_{\rm solar}}. \quad (1)$$

Matsushita et al. (2003) give a detailed discussion for equation (1). Here, $M^{\rm Fe}_{\rm SN\ Ia}$, the Fe mass forged by one SN Ia, is ~ 0.5–$0.7\,{\rm M}_\odot$ (e.g., Iwamoto et al. 1999; Seitenzahl et al. 2013a; Shen et al. 2018; Leung & Nomoto 2018), $\theta_{\rm SN\ Ia}$ is the SN Ia rate, α_* is the mass-loss rate, and $z^{\rm Fe}_{\rm solar} \sim 0.001$ is the solar Fe mass fraction. The optically observed rate of SNe Ia is 0.1–0.4 SN Ia $(100\,{\rm yr}\,10^{10}\,{\rm L}_{B,\odot})^{-1}$ (e.g., Li et al. 2011). Using the injection rate of stellar wind by Ciotti et al. (1991), the expected Fe abundance from SNe Ia in the hot ISM in early-type galaxies is at least 2 solar (e.g., Matsushita et al. 2000; Konami et al. 2014). However, the observed Fe abundances in the ISM of early-type galaxies with *Suzaku* are about 1 solar (e.g., Konami et al. 2014). Since the temperatures of the hot ISM in early-type galaxies are close to that of the ICM in the innermost region of the Centaurus cluster, there may be some systematic uncertainties in the derived metal abundances in the ISM.

The Fe abundance in the ICM at the Fe enhancement of the Centaurus cluster is significantly higher than those in the hot ISM in early-type galaxies. We integrated the stellar mass-loss rate and SN Ia rate over the past 9–10 Gyr, using the injection rate by Ciotti et al. (1991) and the delay-time distribution of SN Ia rate modelled by a power-law behaviour ($\propto t^{-1.34}$, Heringer et al. 2019). Assuming star formation at 2.5 Gyr ($z \sim 2.5$), the present SN Ia rate is estimated to be 0.11 SN Ia $(100\,{\rm yr}\,10^{10}\,{\rm L}_{B,\odot})^{-1}$ in order to produce the entire Fe mass observed in the core over the past 9–10 Gyr. This value is marginally consistent with the SNe Ia rate by the optical observations (Li et al. 2011). When applying star formation at $z = 2$ and $z = 3$, we did not find remarkable changes in these results.

The ratio of the ICM mass to the stellar mass in the core of the Centaurus cluster (~ 4 per cent) is a few orders of magnitude higher than those in early-type galaxies, indicating a longer enrichment timescale (see Sect. 3.4.3). On the other hand, the iron-mass-to-light ratio of the Centaurus cluster core ($\sim 6 \times 10^{-5}\,{\rm M}_\odot/{\rm L}_{K,\odot}$) is much lower than those of clusters of galaxies ($\sim 10^{-4}\,{\rm M}_\odot/{\rm L}_{K,\odot}$, Matsushita et al. 2013a). Note that the latter values would be obtained from a bit broader regions of integration than ours in the Centaurus cluster and calculated using the whole Fe mass from SNe Ia and stellar population; thus, the iron-mass-to-light ratios may be

practically consistent between some clusters of galaxies, excluding the Perseus cluster ($\sim 10^{-3}\,M_\odot/L_{K,\odot}$, Matsushita et al. 2013b). Our proposed enrichments by SNe Ia and/or stellar winds are a relatively recent or even ongoing enrichment scenario in the Centaurus core. However, such a recent enrichment picture hardly explains the uniform and solar X/Fe ratio (in early-type galaxies, the Centaurus core, and other clusters) unless SNe Ia and stellar winds have been sophisticatedly controlled to reproduce the observed abundance pattern, which might be *a handiwork*. Recently, Mernier et al. (2022) argued that the abundance patterns in cluster or galaxy centres are more likely produced by an early enrichment starting at $z \sim 3$ and ending around $z = 2$. If this is the case, enrichment channels must be CCSNe, the earliest SNe Ia, and stellar winds whose rates are more difficult to estimate accurately than those at present. We also note that such an early enrichment scenario is challenged by the escaping or depleting metals that must have been produced subsequently unless the recent SNe Ia and stellar winds are completely quiescent. Further studies of metal abundance, distribution, and cycle process, not only at central cores but also at large scales will provide important clues to solving this cosmic conundrum.

3.4.5 Future prospects

Future X-ray missions with high-resolution and spatially resolved spectroscopy such as *XRISM* is more crucial to reduce the systematic uncertainties and to estimate the absolute abundance in the innermost cool regions of clusters. Since the observational data, the nucleosynthesis models, and the atomic codes are limited at present, we comprehend the necessity of extremely high-resolution spectra with micro-calorimeter detectors onboard future missions like *XRISM* (XRISM Science Team 2020) or *Athena* (Nandra et al. 2013). For example, the Resolve instrument, which will be mounted on *XRISM* and deliver a constant < 7 eV spectral resolution, enables us to resolve the Ne K-shell emission line from the Fe-L complex. Offering its non-dispersive X-ray spectroscopy, the Resolve spectra will provide more accurate spatial information on metal abundances in the cluster and group centres than those with the RGS data. By testing the observation data of low-temperature regions of these targets with laboratory experiments (e.g., electron beam ion traps, Gu et al. 2020), we expect that the remaining uncertainties or gaps between AtomDB and SPEXACT will continue to be improved. In particular, our proposed disagreement in the 0.9–1.2 keV band, possibly attributed to mis-modelling of the Fe XXIII and Ne X emission lines (see Sect. 3.4.1), will be an urgent issue to be resolved. Based on

these upcoming leaps, *XRISM* and/or *Athena* will provide crucial knowledge of metal content in the cluster or group centres, including the abundance drop, as discussed in Gastaldello et al. (2021).

Furthermore, it is important that the trace odd-Z elements other than N are a sensitive diagnostic of the initial metallicity of CCSN progenitors (e.g., Nomoto et al. 2006, 2013) or of the stellar population (e.g., Campbell & Lattanzio 2008; Karakas 2010). Unfortunately, we cannot constrain the abundance of these elements while using the present grating data. The micro-calorimeter detector mounted on *Hitomi* have been shown enough resolution and sensitivity to constrain the abundance of trace odd-Z elements (e.g., Simionescu et al. 2019), which makes us expect invaluable information about the underlying stellar population contributing to the early enrichment history of the ICM.

Chapter 4

Metal Contents in Hot Haloes of Early-type Galaxies

4.0 Statement

This chapter is from a published paper *"O, Ne, Mg, and Fe Abundances in Hot X-Ray-emitting Halos of Galaxy Clusters, Groups, and Giant Early-type Galaxies with XMM-Newton RGS Spectroscopy"* by **K. Fukushima**, S. B. Kobayashi, and K. Matsushita (The Astrophysical Journal, Volume 953, Number 1, 112, 15 pp). This article has been published in full open access by IOP Publishing on behalf of the American Astronomical Society. That is available online at: https://doi.org/10.3847/1538-4357/ace16a. Minor corrections are made to incomprehensible parts and typos in the arXived version.

4.1 Introduction

Since very light nuclei like H and He were created through the Big Bang nucleosynthesis, heavier metals have been produced in stellar cores and ejected into interstellar space by supernova (SN) explosions and mass-loss winds over several giga years. As widely known, core-collapse SNe (CCSNe) synthesize a significant fraction of O, Ne, and Mg (e.g., Nomoto et al. 2013). Type Ia SNe (SNe Ia) predominantly forge the Fe-peak elements (Cr, Mn, Fe, and Ni) in the cores of exploding white dwarfs (e.g., Leung & Nomoto 2018). On the other hand, light metals such as C and N are thought to be generated in the outer layers of massive or asymptotic giant branch (AGB) stars and dispersed via mass-loss winds (e.g., Prantzos et al. 2018; Kobayashi et al. 2020). Today, the bulk of these metals reside within the interstellar medium that pervades the intra- and intergalactic spaces. In addition, the brightest cluster galaxies

(BCGs) of clusters or groups, and early-type galaxies would undergo an ongoing enrichment process by SNe Ia and mass-loss winds. Therefore, metal abundances and their spatial distribution in the hot gaseous haloes [21] of these systems provide one of the most powerful probes for investigating chemical enrichment in the largest scales of the universe.

In the last two decades, thanks to modern X-ray observatories that offer both spectral and spatial resolutions, we have assessed the cosmic mystery of metals from various aspects (e.g., Mernier et al. 2018a; Gastaldello et al. 2021, for recent reviews). We can test model calculations of the nucleosynthesis and/or mass-loss yield by comparing them to the observed abundance pattern (e.g., de Plaa et al. 2007; Hitomi Collaboration et al. 2017; Mao et al. 2019; Simionescu et al. 2019). The enrichment history, including metal transportation triggered by the cooling flows and feedback from central galaxies, is also studied based on the studies of metal distributions, especially in central regions (e.g., Sanders et al. 2016; Mernier et al. 2022). Particularly, the detailed element abundance pattern and distribution of metals are well investigated in core regions of clusters and groups thanks to their luminous X-ray emissions.

An intriguing puzzle is the "metal abundance drop" that is reported within a central few-kiloparsec region of relaxed clusters and groups, even though there should be active enrichment from their BCGs. After the Fe abundance drop was first discovered in A2199 (Johnstone et al. 2002), central abundance depletions have been reported in some cool-core systems despite active element supply from their central galaxies (e.g., Churazov et al. 2003; Panagoulia et al. 2015; Mernier et al. 2017; Liu et al. 2019). Based on a metallicity profile derived from CCD data, Panagoulia et al. (2015) partly attributed these drops to metal depletion into the cool dust grains, which is supported by Lakhchaura et al. (2019) for the Centaurus cluster; the noble gas Ar shows a more marginal drop than the Si, S, and Fe abundances. However, the abundance distribution of the same noble gas Ne has been poorly constrained because CCD instruments installed on current observatories such as *Chandra* and *XMM-Newton* cannot resolve the Ne K-shell emission from the Fe-L bump sufficiently (Liu et al. 2019).

The current solution is the Reflection Grating Spectrometer (RGS) on board *XMM-Newton* offering a much better spectral resolution than CCDs. While the RGS instrument has been initially aimed to observe point-like sources (den Herder et al.

[21] Throughout this chapter, we use "halo(es)" interchangeably referring to the intracluster, intragroup, and interstellar media, for convenience.

2001), it can provide important spatial information in extended emission from a luminous X-ray source such as a galaxy centres (e.g., Chen et al. 2018; Zhang et al. 2019). In addition, RGS surpasses any CCD detectors to date at resolving the spectra in the 0.8–1.5 keV band within which two major atomic codes, i.e. the atomic database (AtomDB, Smith et al. 2001; Foster et al. 2012) and the SPEX Atomic Code and Tables (SPEXACT, Kaastra et al. 1996), have been not fully convergent yet (e.g., Gastaldello et al. 2021). In this manner, Fukushima et al. (2022) recently estimated the radial profile of the Ne/Fe ratio in the X-ray-luminous Centaurus cluster core using the RGS data. They provided a robust result that the Ne/Fe ratio shows a flat distribution at the central part of the cluster where the Fe abundance drop has been reported. Their flat RGS Ne/Fe and CCD Ar/Fe profiles make the metal depletion scenario challenging, and the abundance drop in the Centaurus core is difficult to explain. Similar flat profiles of Ne/Fe and Ar/Fe are also reported in the Virgo centre (M87) with the CCD study (Gatuzz et al. 2023).

Precise measurement of the O and Ne abundances and their distribution are also essential for more sophisticated screening of the CCSN nucleosynthesis models since the C-ignition process forges these metals in supergiants (e.g., Doherty et al. 2015; Kobayashi et al. 2020). While the O abundances have been well investigated in clusters, groups, and early-type galaxies (e.g., de Plaa et al. 2017), few reports study and discuss the detailed (and robust) spatial variation and/or pattern of the Ne abundance due to the limitations of CCD detectors. As mentioned above, however, RGS data can give us an excellent complement to our knowledge of metal abundances with CCDs for luminous extended sources.

This chapter analyses the RGS data of the central part of galaxy clusters, groups, and early-type galaxies. We mainly intend to study the N, O, Ne, Mg, Fe, and Ni abundance patterns and, if possible, their spatial distribution in X-ray haloes of these systems, which will provide helpful information to assess abundance drops. The uncertainties of the two latest atomic codes (AtomDB and SPEXACT) are also discussed in our spectral analysis. This chapter is structured as follows. In Sect. 4.2, we summarize our *XMM-Newton* observations and data reduction. Section 4.3 presents details of our spectral analysis. We interpret and discuss the results in Sect. 4.4. In this part, cosmological parameters are assumed as $H_0 = 70\,\mathrm{km\,s^{-1}\,Mpc^{-1}}$, $\Omega_m = 0.3$ and $\Omega_\Lambda = 0.7$. All abundances are given in reference to the proto-solar values from Lodders et al. (2009). The errors are given at the 1σ confidence level unless stated otherwise.

4.2 Observations and Data Reduction

In this work, we analysed the publicly archival observation data of core regions of 14 nearby early-type galaxies, including BCGs in groups and clusters with RGS mounted on *XMM-Newton* (den Herder et al. 2001). Table 6 lists the analysed objects in this work and some properties thereof. Our sample is based on well-known objects of the chemical enrichment RGS sample (CHEERS, de Plaa et al. 2017) for objects with long total exposure (> 50 ks) and good statistic of Fe-L lines ($> 10^5$ counts in the 0.9–1.2 keV band). For simplicity, we limited the sample to ellipticals and/or BCGs. Finally, our sample has four central galaxies of compact groups and seven BCGs, including both types of systems with and without Fe abundance drops (Panagoulia et al. 2015; Liu et al. 2019). This sample allows us to study the Ne abundance of objects in various temperature and gas mass regimes. The data reduction was performed using the *XMM-Newton* Science Analysis System (SAS). All RGS data were reprocessed with `rgsproc` following the standard procedures by the SAS team. First, we extracted light curves and fitted them with Gaussians; then, the mean count rate μ and standard deviation σ were calculated. A $\mu \pm 2\sigma$ threshold was applied to create good time intervals. Table 6 summarizes total exposures after removing flare events.

When the X-ray peak of the target object is close to the pointing position, the RGS spectra can provide one-dimensional spatial information over a 5 arcmin width ($\lesssim$ the width of the central CCD chip of the MOS detectors) along the cross-dispersion direction (e.g., Chen et al. 2018; Zhang et al. 2019; Fukushima et al. 2022). All the data sets listed in Table 6 have offsets less than 0.5 arcmin from the centre of the target object. By the prescription in Fukushima et al. (2022), we extracted first- and second-order RGS spectra centred on the emission peaks of each object along the dispersion direction. The response matrices are generated for each spectrum. We filtered events by the cross-dispersion direction and extracted spectra over a broad region on each side with 0–6, 6–18, 18–60, 60–120, and 0–60 arcsec. As discussed in Fukushima et al. (2022), this method has the advantage of region selection with an accurate width exactly matching the one of the corresponding annular compared to the use of the `xpsfincl` parameter that has been traditionally utilized. The first- and second-order spectra are fitted together, combining the RGS1 and RGS2 spectra for each order. Our analysis in the following sections provided consistent results, regardless of whether or not combining the different responses of these two instruments.

Table 6: The RGS observations analysed in this chapter.

Object	ObsID	l, b[a] (deg)	Redshift[b]	$N_{\rm H}$[c] (10^{20} cm^{-2})	Luminosity[d] (10^{10} L$_{\odot}$)	Exposure[e] (ks)
NGC 1404	0781350101	237.0, −53.6	0.0065	1.6	5.0	122.7
NGC 4636	0111190701	297.7, 65.5	0.0037	2.1	3.6	56.8
NGC 4649	0021540201, 0502160101	295.9, 74.3	0.0037	2.2	4.5	118.2
NGC 5846	0021540101/501, 0723800101/201	0.42, 48.8	0.0061	5.1	3.7	188.8
M49	0200130101	286.9, 70.2	0.0044	1.6	9.6	76.3
HCG 62	0504780501/601, 0112270701	303.6, 53.7	0.0140	3.8	2.1	134.2
Fornax	0400620101, 0012830101	236.7, −53.6	0.0046	1.6	3.9	143.8
NGC 1550	0152150101, 0723800401/501	191.0, −31.9	0.0123	16	2.2	165.5
M87	0803670601, 0200920101, 0114120101	283.8, 74.5	0.0042	2.1	6.6	182.0
A3581	0205990101, 0504780301/401	323.1, 32.9	0.0214	5.3	4.0	126.7
A262	0109980101, 0504780201	136.6, −25.1	0.0161	7.2	2.1	57.3
AS 1101	0147800101, 0123900101	348.3, −64.8	0.0580	1.2	11	99.3
AWM 7	0605540101, 0135950301	146.3, −15.6	0.0172	12	2.6	150.4
Perseus	0085110101/201, 0305780101	150.6, −13.3	0.0183	21	8.0	167.6

[a] Galactic coordinates of object centres.

[b] Redshift of each object retrieved from Chen et al. (2007) and Snowden et al. (2008).

[c] Galactic absorption column densities calculated using the method of Willingale et al. (2013).

[d] The B-band luminosity (peaked at 440 nm) of early-type galaxies and BCGs in clusters or groups retrieved from Makarov et al. (2014).

[e] Total exposure time after the filtering procedures described in Sect. 4.2.

4.3 Analysis and Results

4.3.1 *Spectral fitting*

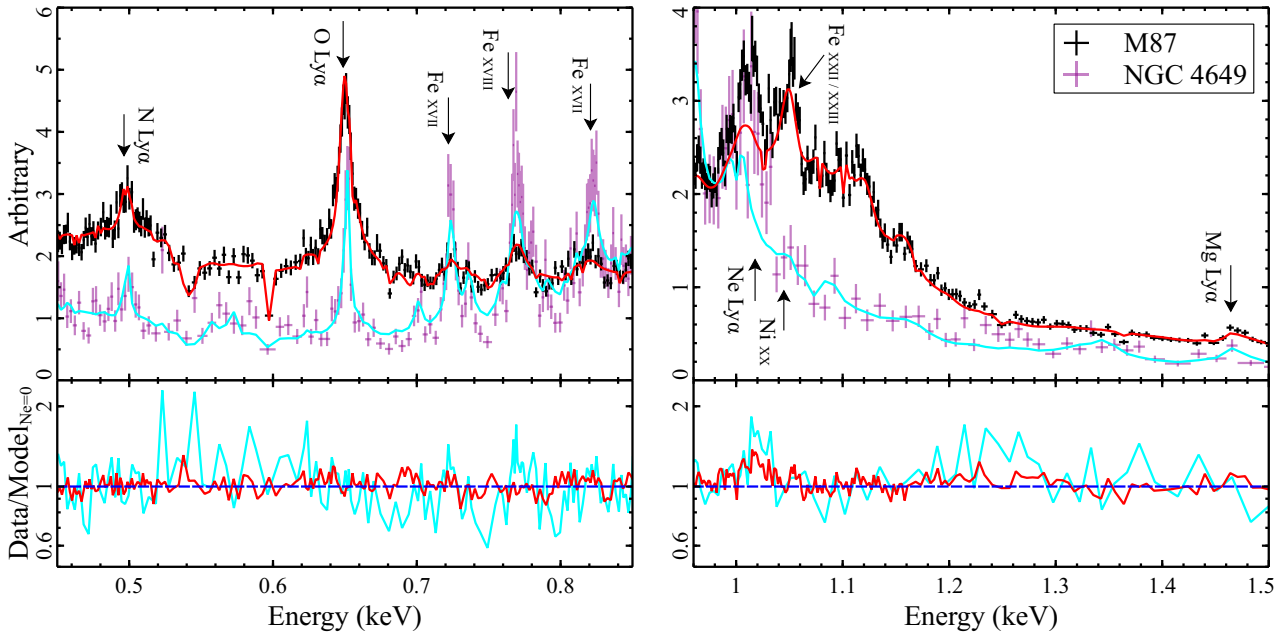

Figure 22: RGS spectra of M87 and NGC 4649 extracted from the 0–60 arcsec slice. The crosses indicate the first-order data and the solid lines represent the best-fitting models with AtomDB, but assuming Ne is 0 solar. The ratios of data to the zero-Ne models are plotted in the lower panels. The emission lines of our interesting elements are marked on the upper panels.

The spectral fittings of the RGS X-ray spectra substantially follow the same strategy as Fukushima et al. (2022). We use the XSPEC package version 12.10.1f (Arnaud 1996). In the subsequent spectral fits, the model parameters and their error ranges are estimated using the C-statistic method (Cash 1979), expecting a smaller bias than the χ^2 technique (Kaastra 2017). The spectra are re-binned to have at least one count per spectral bin. We fit the first- and second-order spectra jointly in the 0.45–1.75 keV and 0.8–1.75 keV bands, respectively, with the same fitting parameters. Given that the halo emission dominates the other astrophysical background emissions in our analysis regions, only the possible instrumental component is accounted for by a steep power-law model. We take the broadening effect on emission lines due to the spatial extent of the source into account by using the `rgsxsrc` model with MOS1 images.

We utilize the latest AtomDB version 3.0.9 [22] to reproduce the emissions from collisional ionization equilibrium (CIE) plasmas. The spectra obtained from each object

[22] http://www.atomdb.org

Table 7: Best-fitting spectral parameters for halo emission within 60 arcsec regions.

Object	$\langle kT \rangle$[a] (keV)	$kT_{\rm hot}$[b] (keV)	$\rm VEM_{hot}$[c] (10^{10} cm^{-5})	$\rm VEM_{middle}$[c] (10^{10} cm^{-5})	$\rm VEM_{cool}$[c] (10^{10} cm^{-5})	C-stat/dof	Regime[d]
NGC 1404	0.49 ± 0.08	0.68 ± 0.14	16 ± 2	16.9 ± 1.0	1.7 ± 1.0	4441.3/3512	C
NGC 4636	0.61 ± 0.04	0.77 ± 0.06	27.6 ± 0.7	14.4 ± 0.8	2.4 ± 0.7	3594.8/3259	C
NGC 4649	0.82 ± 0.04	0.86 ± 0.13	$27.2^{+2.7}_{-0.7}$	< 0.7	1.8 ± 0.3	3558.5/3343	C
NGC 5846	0.56 ± 0.12	0.8 ± 0.2	$20.1^{+0.5}_{-4.6}$	$13.8^{+4.3}_{-0.6}$	$4.0^{+0.4}_{-3.0}$	3468.9/3316	C
M49	0.92 ± 0.05	0.98 ± 0.08	32.3 ± 0.9	3.8 ± 0.3	0.6 ± 0.5	3738.9/3476	C
HCG 62	0.80 ± 0.14	1.0 ± 0.3	26 ± 4	5.7 ± 1.3	$4.3^{+9.7}_{-0.7}$	3240.8/3154	C
Fornax	$0.83^{+0.17}_{-0.04}$	$0.9^{+1}_{-0.06}$	50^{+28}_{-1}	3.8 ± 0.4	$3.2^{+47.1}_{-0.7}$	4196.4/3582	C
NGC 1550	1.26 ± 0.16	1.3 ± 1.0	40^{+3}_{-22}	$0.44^{+1.4}_{-0.2}$	0.6 ± 0.4	3596.5/3575	W
M87	1.5 ± 0.2	$1.5^{+1.1}_{-0.3}$	$4.2^{+2.2}_{-0.4} \times 10^2$	$16.6^{+8.7}_{-1.5}$	$1.2^{+1.0}_{-0.5}$	4122.0/3672	W
A3581	1.56 ± 0.07	1.6 ± 0.2	95 ± 5	2.2 ± 0.8	0.7 ± 0.4	3649.5/3589	W
A262	1.8 ± 0.3	1.9 ± 0.4	71 ± 10	3.5 ± 0.5	1.1 ± 0.3	3181.4/3379	W
AS 1101	2.6 ± 0.2	2.6 ± 0.5	$(1.51 \pm 0.14) \times 10^2$	$3.1^{+3.2}_{-1.3}$	1.2 ± 0.3	3812.1/3659	H
AWM 7	2.8 ± 0.5	2.9 ± 0.9	79 ± 15	$1.3^{+4.8}_{-0.9}$	1.5 ± 0.3	3672.6/3644	H
Perseus	2.73 ± 0.18	2.8 ± 0.4	$(1.39 \pm 0.13) \times 10^3$	11^{+45}_{-4}	30 ± 4	4359.0/3668	H

[a] The VEM-weighted average temperature.

[b] Temperature of the hot component.

[c] The volume emission measures (VEMs) of each temperature component. The VEM is given as $\int n_e n_{\rm H} dV/(4\pi D^2)$, where V and D are the volume of the emission region (cm^3) and the angular diameter distance to the emitting source (cm), respectively.

[d] We define three temperature regimes of cool (C), warm (W), and hot (H): $\langle kT \rangle$ is less than 1.0 keV, greater than 1.0 keV and less than 2.0 keV, and greater than 2.0 keV, respectively.

Table 8: The Fe abundance and the N/Fe, O/Fe, Ne/Fe, Mg/Fe, and Ni/Fe ratios for halo emission within 60 arcsec regions. For NGC 4649, HCG 62, Fornax, and NGC 1550, the O/Fe, Ne/Fe, and Mg/Fe ratios are computed by averaging over each radial bin (see Sect. 4.3.2).

Objec	Fe (solar)	N/Fe (solar)	O/Fe (solar)	Ne/Fe (solar)	Mg/Fe (solar)	Ni/Fe (solar)
NGC 1404	0.34 ± 0.02	2.1 ± 0.4	0.58 ± 0.04	1.28 ± 0.14	1.66 ± 0.15	3.4 ± 0.5
NGC 4636	0.56 ± 0.02	1.6 ± 0.3	0.64 ± 0.04	0.89 ± 0.09	1.10 ± 0.11	2.4 ± 0.3
NGC 4649	$0.39^{+0.08}_{-0.02}$	2.6 ± 0.8	0.73 ± 0.09	1.52 ± 0.12	1.31 ± 0.14	1.7 ± 0.4
NGC 5846	0.35 ± 0.01	2.5 ± 0.5	0.74 ± 0.09	1.24 ± 0.13	1.33 ± 0.16	4.2 ± 0.6
M49	0.46 ± 0.03	2.7 ± 0.6	1.01 ± 0.09	1.45 ± 0.19	1.86 ± 0.16	2.9 ± 0.4
HCG 62	$0.24^{+0.10}_{-0.02}$	1.1 ± 0.8	1.01 ± 0.07	1.44 ± 0.18	2.2 ± 0.2	1.5 ± 0.7
Fornax	0.28 ± 0.02	4.3 ± 0.9	1.23 ± 0.09	1.52 ± 0.13	1.77 ± 0.16	4.8 ± 0.6
NGC 1550	0.57 ± 0.07	3.5 ± 1.3	1.31 ± 0.10	0.91 ± 0.16	0.61 ± 0.18	1.9 ± 0.5
M87	$0.67^{+0.16}_{-0.04}$	2.5 ± 0.4	1.09 ± 0.05	0.97 ± 0.07	1.02 ± 0.08	1.9 ± 0.2
A3581	0.66 ± 0.04	< 1.3	1.14 ± 0.10	0.96 ± 0.17	1.15 ± 0.15	0.7 ± 0.3
A262	1.0 ± 0.2	3.8 ± 1.4	1.23 ± 0.16	1.1 ± 0.3	0.7 ± 0.3	1.1 ± 0.6
AS 1101	0.67 ± 0.09	< 0.8	1.10 ± 0.10	0.99 ± 0.14	0.76 ± 0.15	1.0 ± 0.4
AWM 7	$2.0^{+1.4}_{-0.4}$	< 0.4	1.17 ± 0.09	0.8 ± 0.2	1.33 ± 0.17	1.3 ± 0.3
Perseus	0.84 ± 0.06	0.9 ± 0.5	1.58 ± 0.05	1.14 ± 0.07	0.73 ± 0.05	1.02 ± 0.13

are modelled with three `bvvtapec` components. Two temperatures for line and continuum have the same value because the continuum temperature is poorly constrained for the RGS spectra. Although the two-phase CIE modelling has been used to reproduce the halo emissions (e.g., Panagoulia et al. 2013; de Plaa et al. 2017; Lakhchaura et al. 2019; Simionescu et al. 2019), it can still underestimate the Fe abundance in some cases (the "double Fe bias", see Mernier et al. 2022). Here, the triple-component model is chosen in our analysis. We do not adopt any assumption regarding the emission measures of each temperature component. Instead, temperatures of each component are coupled along a geometric series with a common ratio of 0.5 to interpolate the continuous temperature structure as $kT_{\rm hot} : kT_{\rm middle} : kT_{\rm cool} = 1 : 0.5 : 0.25$. We note that adding the fourth component does not change fitting results nor improve the fitting significantly, as in the case of the Centaurus cluster in Fukushima et al. (2022). The model with free temperatures also makes minor changes to other parameters. Our modelling sufficiently interpolates the continuous temperature distribution in haloes, giving better fits than a Gaussian differential emission measure model. All three CIE plasmas are modified by a common Galactic absorption of `phabs` whose column densities are calculated following the method of Willingale et al. (2013) for each object (summarized in Table 6). We adopt absorption cross sections of Verner et al. (1996).

Here, we show the representative spectra obtained from the 60 arcsec cores of M87 and NGC 4649 (Fig. 22). Prominent K-shell emission lines of N, O, Ne, and Mg, as well as the L-shell emission lines of Fe, are detected in the spectra. In addition to these metals, the Ni abundance is also allowed to vary, and the abundances of other elements with faint lines shrouded under the continuum emission are fixed to the solar value. All abundances for the three temperature components are tied to each other. Finally, we allow the volume emission measures (VEMs) of each component to vary, which is given as $\int n_e n_{\rm H} dV/(4\pi D^2)$, where n_e and $n_{\rm H}$ are electron and proton density, V and D are the volume of the emission region and the angular diameter distance to the object, respectively.

We perform the fitting to spectra extracted not only from each slice with 0–6, 6–18, 18–60, and 60–120, and 0–60 arcsec. Our modelling largely gives a good fit with the ratios of the C-statistic value to degrees of freedom (C-stat/dof) $\sim$ 1 in the broader region and each slice. The fitting results are summarized in Tables 7 and 8 for the 0–60 arcsec regions. Results for each slice will be indicated in figures in subsequent sections. In Fig. 22, the model partially fails to reproduce the spectrum of NGC 4649 around the 0.7–0.8 keV band, wherein the Fe XVII and Fe XVIII lines are affected

by a large optical depth of resonant scattering (e.g., Sanders et al. 2008; Ogorzalek et al. 2017). Mernier et al. (2022) suggests that simply excluding the Fe XVII line makes minor changes in the abundance ratios up to 10 per cent. In addition, we also test to add Gaussians with a negative normalization at these emission lines possibly contaminated by the resonant scattering effect in some early-type galaxies. However, this model remains similar to our measurement of abundance ratios. The resonant scattering effect can matter just on reproducing line intensities of Fe, especially for Fe XVII and Fe XVIII, not on measuring abundances and ratios.

4.3.2 Radial abundance profiles

Here, we provide the central metal distribution in the hot haloes of each system. In Fig. 23, the radial profiles of the Fe abundance are plotted for each object. In some previous works with CCD detectors, NGC 4636, NGC 4649, NGC 5846, HCG 62, A3581, A262, AS 1101, and Perseus are proposed to show an Fe abundance drop (e.g., Churazov et al. 2003; Panagoulia et al. 2015; Liu et al. 2019). Our RGS results show no clear abundance declination in these objects, excluding a hint of a drop in the Perseus cluster. Likewise, M87 has a sharp Fe drop, where no abundance drop has been reported with CCD studies so far (e.g., Matsushita et al. 2003; Million et al. 2011; Gatuzz et al. 2023). However, we should be cautious in interpreting these profiles because the metal abundances are estimated using the RGS spectra. Additionally, the abundance drop might be detected only with broadband spectra, including both the Fe L- and K-shell emission lines (Gatuzz et al. 2022, for the Centaurus cluster).

The relative abundance ratio to Fe is a more robust parameter than the absolute abundance in the RGS analysis (e.g., de Plaa et al. 2017; Gastaldello et al. 2021). We plot the O/Fe, Ne/Fe, and Mg/Fe abundance ratios in Fig. 24, removing the outermost bins of NGC 4649 and HCG 62 with large errors (> 1.5 solar) due to their line-poor or line-less spectra. This is the first report of the Ne distribution using the RGS data sets. Considering that the Fe-L bump with CCD spectra obscures the Ne Lyα lines severely, our Ne profile is more reliable than previous ones (e.g., Million et al. 2011; Liu et al. 2019). More importantly, such a flat distribution shows no individuality among the samples, irrespective of whether or not an object shows an abundance drop (in CCD spectra, e.g., Panagoulia et al. 2013; Liu et al. 2019). The ratios are primarily around the solar ratio and give a flat profile within the 60 arcsec regions in each object, except for NGC 1404. In NGC 1404, the Ne/Fe and Mg/Fe ratios

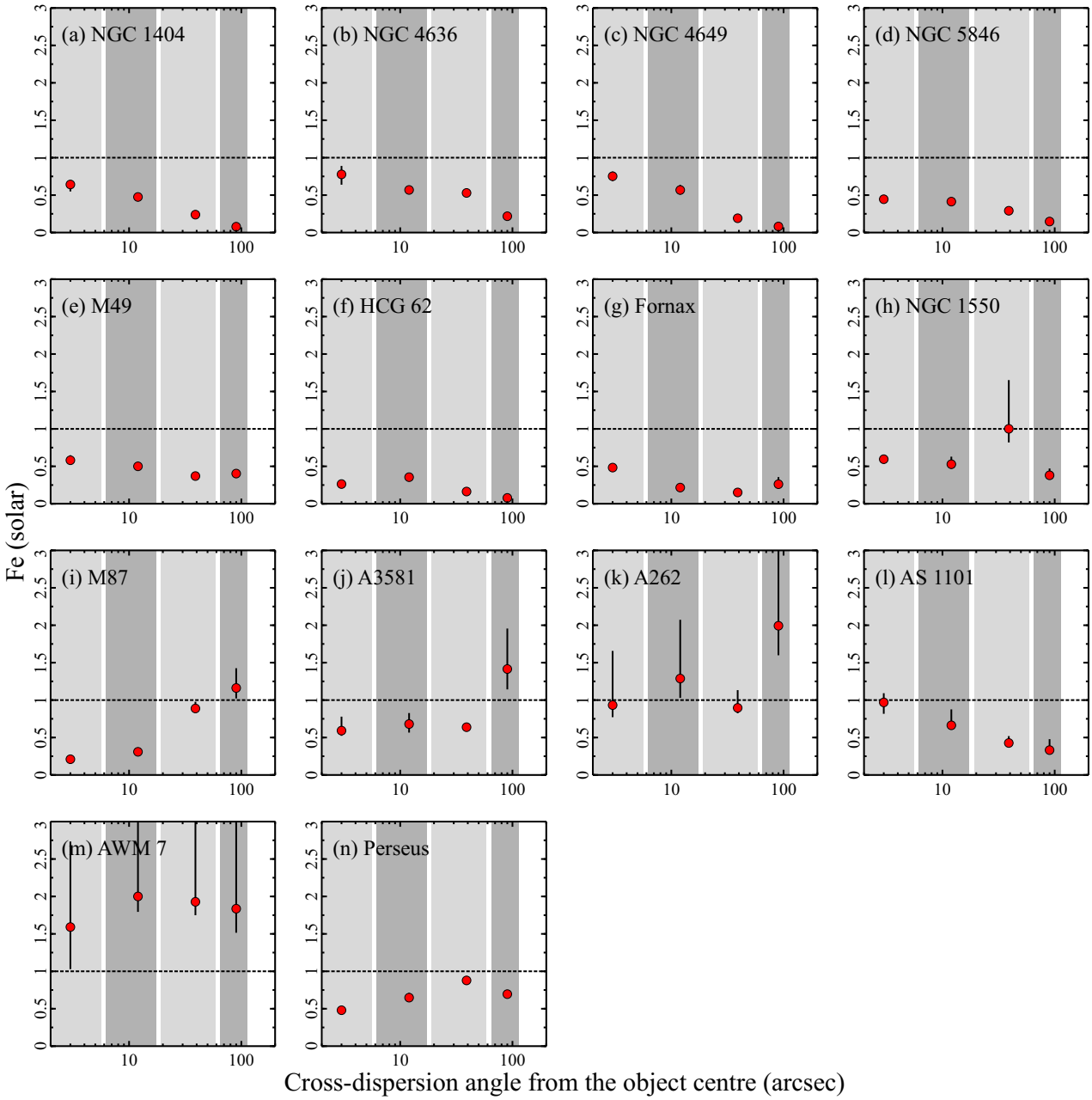

Figure 23: Radial profiles of the Fe abundance as a function of radial distance in units of arcseconds from the centre of each object. Grey areas show the width of the slice region for RGS analysis: 0–6, 6–18, 18–60, and 60–120 arcsec from left to right, respectively. The solar ratio is indicated with dotted lines on each panel.

exhibit clear central enhancements despite a flat distribution of O/Fe as in the other systems. Following Mernier et al. (2022), we have also included the halo emission from the Fornax cluster as a background of NGC 1404 in the outer two bins. Our background treatment does not change the abundance measurements in the outer region of NGC 1404.

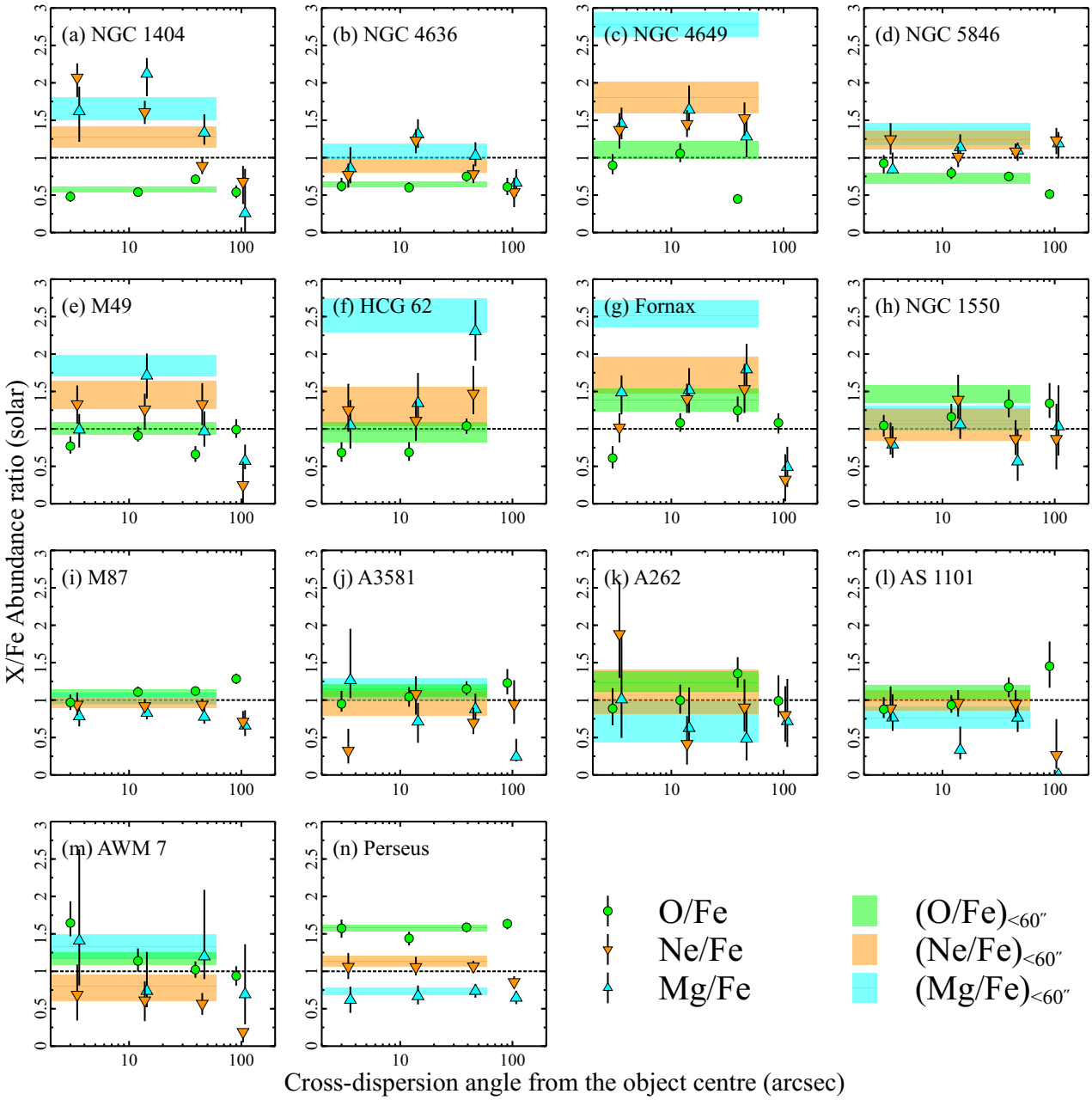

Figure 24: Radial profiles of the O/Fe, Ne/Fe, and Mg/Fe abundance ratios for each object. The circles, down-, and up-triangles represent the O/Fe, Ne/Fe, and Mg/Fe ratios, respectively, as a function of distance in units of arcseconds from the centre of each object. The plots are slightly shifted on the x-axis for clarity. Color-shaded areas show the ratios obtained from broad 60 arcsec slices. The solar ratio is indicated with dotted lines on each panel.

4.3.3 Abundances and temperature in the central 60 arcsec

As reported in Sect. 4.3.2, the O/Fe, Ne/Fe, and Mg/Fe profiles generally show a flat distribution in the central 60 arcsec core of each halo, suggesting that the metal content is remarkably uniform in these central cores. The best-fitting parameters of the 0–60 arcsec slice are summarized in Tables 7, 8, and Fig. 24 (shaded areas).

Notably, our estimated abundance ratios of the Perseus cluster are globally consistent with the previous report by Simionescu et al. (2019) despite a different spectral fitting strategy. The low Fe abundance of theirs ~ 0.4 solar may originate from a narrower width of about 0.8 arcmin than our selection and/or their simple biphasic component modelling.

Table 7 also gives the VEM-weighted average temperatures (expressed as $\langle kT \rangle$) derived within the 60 arcsec core. These values suggest that our samples will be divided into three subgroups by $\langle kT \rangle$ of haloes. Henceforward, two threshold temperatures ($\langle kT \rangle = 1$ and 2 keV) determine three regimes of cool, warm, and hot haloes (denoted by C, W, and H, respectively). Tables 6 and 7 suggest that three temperature regimes correspond well to the traditional classification of object scales, i.e. "galaxies", "groups", and "clusters".

One caveat is that the abundance ratios obtained from the cumulative spectra are sometimes overestimated, especially for Mg/Fe, compared to those of each individual bin (e.g., see the cyan area and up-triangles for NGC 4649, Fig. 24(c)). Such a gap is apparent in the C-regime objects that have relatively low Mg lines (Fig. 22(b)). Abundance estimate by RGS is complex for metals whose emission lines do not dominate the continuum component (e.g., de Plaa et al. 2017; Mao et al. 2019; Gastaldello et al. 2021). A strategy of narrow-band fits within 1.3–1.6 keV around the Mg Lyα line, which can minimize such biases, improves the overestimation, yielding Mg/Fe = 1.5, 2.1, and 2.2 solar for NGC 4649, HCG 62, and Fornax, respectively. Thus, we report in Table 8, giving up better photon statistics of cumulative spectra, and adopt the average ratios over the inner three bins instead of unreasonably high ratios for concerning objects in subsequent sections.

4.3.4 AtomDB vs SPEXACT

Abundance measurements will suffer from a systematic bias caused by uncertainties in atomic codes (e.g., Mernier et al. 2020, for a review). In this work, we test the SPEXACT version 3.06 (Kaastra et al. 1996) on the spectra extracted within the 60 arcsec regions to examine the differences arising from systematics in the atomic data. In order to minimize modest deviations in the modelling procedure of XSPEC and SPEX, we tabulate the lines and continuum information calculated by a simple `cie` model at 201 bins of temperature on SPEX and export them into the APEC table format that can be directly read in XSPEC. This process is done with a PYTHON code

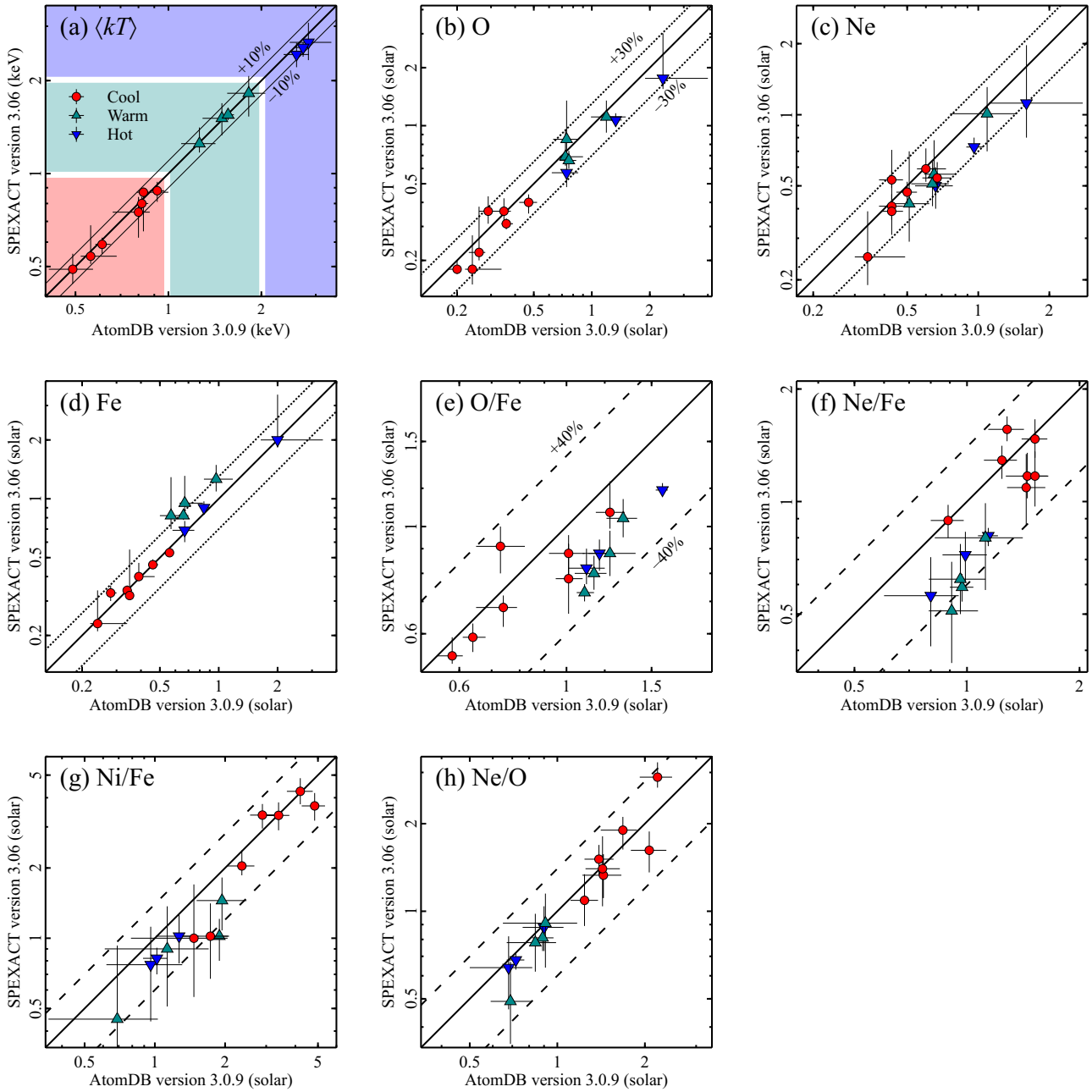

Figure 25: Comparisons of the spectral parameters obtained from central 60 arcsec slices for each object when using AtomDB or SPEXACT. (a) The VEM-weighted averaged halo temperature. Our sample is subdivided into three subsamples: cool, warm, and hot (see the text) represented by the circles, up-, and down-triangles, respectively. (b, c, d) The absolute abundances of O, Ne, and Fe. (e, f, g, h) The relative abundance ratios of O/Fe, Ne/Fe, Ni/Fe, and Ne/O. The solid lines in each panel indicate equal values between the two codes. The thin-solid, dotted, and dashed lines delimitate ±10, 30, and 40 per cent limits, respectively.

that is publicly available [23].

In Fig. 25, we show direct comparisons of $\langle kT \rangle$, abundances, and relative abundance ratios between AtomDB and SPEXACT. Apparently seen is that the $\langle kT \rangle$

[23] https://github.com/jeremysanders/spex_to_xspec

measurements are in quite good agreements between the two codes ($\lesssim 10$ per cent) regardless of the halo temperature regimes (Fig. 25(a)). Such agreements on gas temperature between two codes have also been reported not only for RGS data but also for calorimetric ones (Hitomi Collaboration et al. 2018a; Simionescu et al. 2019). The O, Ne, and Fe abundances are mostly consistent with each other in up to ~ 30 per cent differences. For the abundance ratios, more moderate agreements $\lesssim 40$ per cent are measured (Figs. 25(e), (f), (g), and (h)). The Ne/O ratios show a relatively small scatter compared to O/Fe, Ne/Fe, and Ni/Fe, and are consistent within their error intervals. These differences between the two codes are possibly consistent with the report of the abundance measurements in the intracluster medium of some clusters (Mernier et al. 2020). Most importantly, these agreements between the atomic codes are independent of the temperature regimes.

4.4 Discussion

4.4.1 Flat O/Fe, Ne/Fe, and Ne/O profiles

As described in Sect. 4.1, the detailed mechanisms of the abundance drops are still elusive. Panagoulia et al. (2015) and Lakhchaura et al. (2019) claimed the dust grains as the origin of such abundance drop and noted that the distribution of non-reactive elements (Ne and Ar) is essential to verify this scenario. For the Centaurus cluster, Fukushima et al. (2022) reported flat radial profiles of the Ne/Fe and Ar/Fe ratios, which suggests that Fe and non-reactive elements have the same spatial distribution. This result is difficult to explain only by the dust depletion process.

In Figs. 26, we show the (a) Fe, (b) O/Fe, (c) Ne/Fe, and (d) Ne/O profiles for representative objects in addition to our previous results of the Centaurus cluster. While the Fe abundance shows various variations across the objects, the O/Fe, Ne/Fe, and Ne/O abundance ratios are relatively flat in the central two or three bins, except for NGC 1404. For the majority of our samples, noble gas Ne and other metals are identically distributed in haloes independent of the (possible) presence of abundance drops. While O and Fe are independently synthesized by CCSNe and SNe Ia, respectively, the dominant fraction of O and Ne must share the same origin. Thus, common flat Ne/Fe and Ne/O profiles strongly contradict the dust grains scenario. Additionally, measuring the absolute abundance with the RGS spectra suffers from systematic uncertainties since the grating spectra are dominated by line emissions rather than continuum emissions (e.g., Mernier et al. 2018a). Hence, the Fe abundance

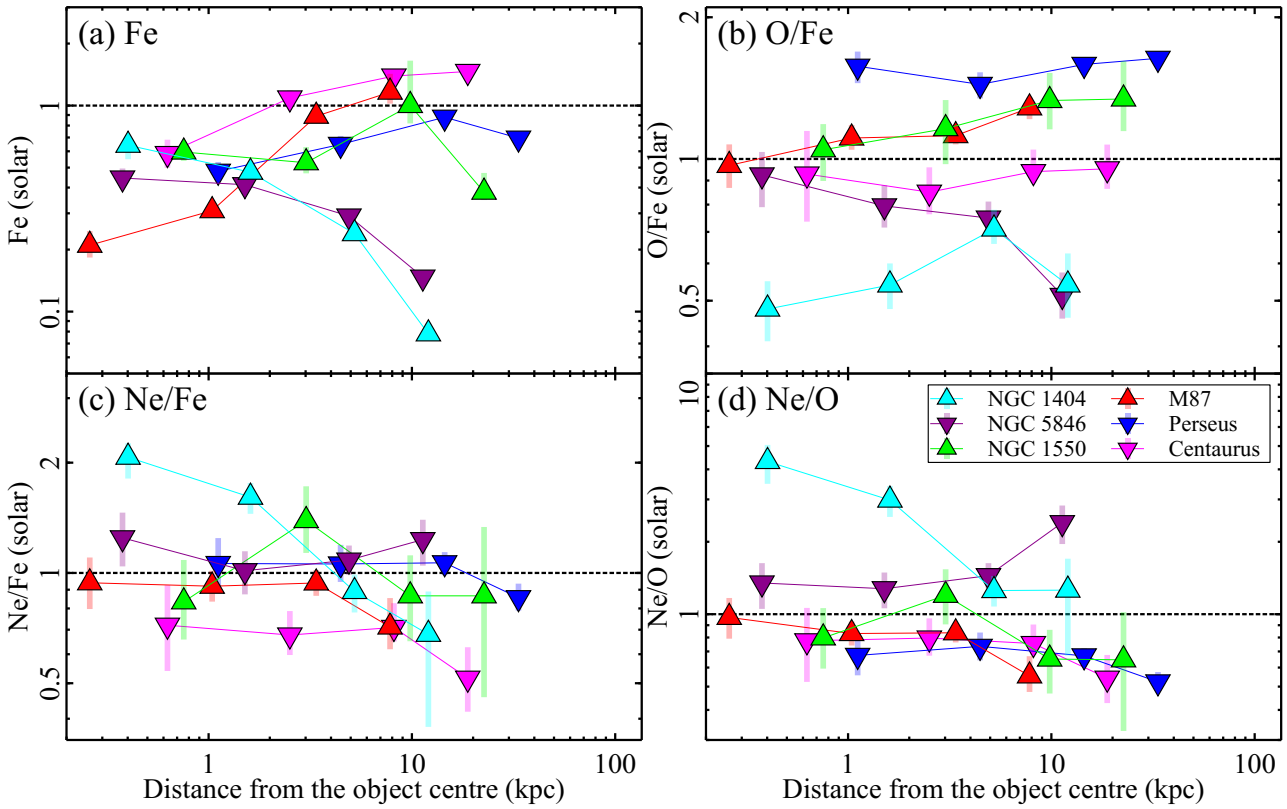

Figure 26: Radial profiles of (a) Fe, (b) O/Fe, (c) Ne/Fe, and (d) Ne/O for representative objects. All are plotted as a function of distance in units of kiloparsecs from the centre of each system. No Fe abundance drop has been reported in objects plotted by up-triangles, and down-triangles are for the Fe drop ones. The values of the Centaurus cluster are retrieved from Fukushima et al. (2022). The solar ratio is indicated with dotted lines on each panel.

drop suggested for M87 and Perseus is caused at least partly by other physical processes such as the central black hole activity and/or artificial uncertainties in abundance measurement, like atomic codes.

One exception is a remarkable enhancement of Ne compared to O and Fe in NGC 1404 (Figs. 26(c) and (d)). However, Mernier et al. (2022) determined the abundance distribution of Mg, Si, and Fe by CCDs installed on *XMM-Newton*, where the centrally-peaked profiles rather than dropping ones are reported, especially for Fe. Our increasing profiles of Fe and Mg/Fe toward the centre support their results (see Figs. 23(a) and 24(a)). Then, suppose that the dust grains do work significantly in this object; in that case, commonly observed increases of Ne/Fe and Mg/Fe are unreasonable because Mg is effectively depleted into dust compared to noble-gas Ne. The dust formation scenario likely does not matter in NGC 1404, even if an increasing Ne/O profile is practically observed.

Worth mentioning is that the innermost $\langle kT \rangle$ of NGC 1404 is the coolest one in our analysis (Sect. 4.3.1). We also plot the Ne/O ratios as a function of local $\langle kT \rangle$ at

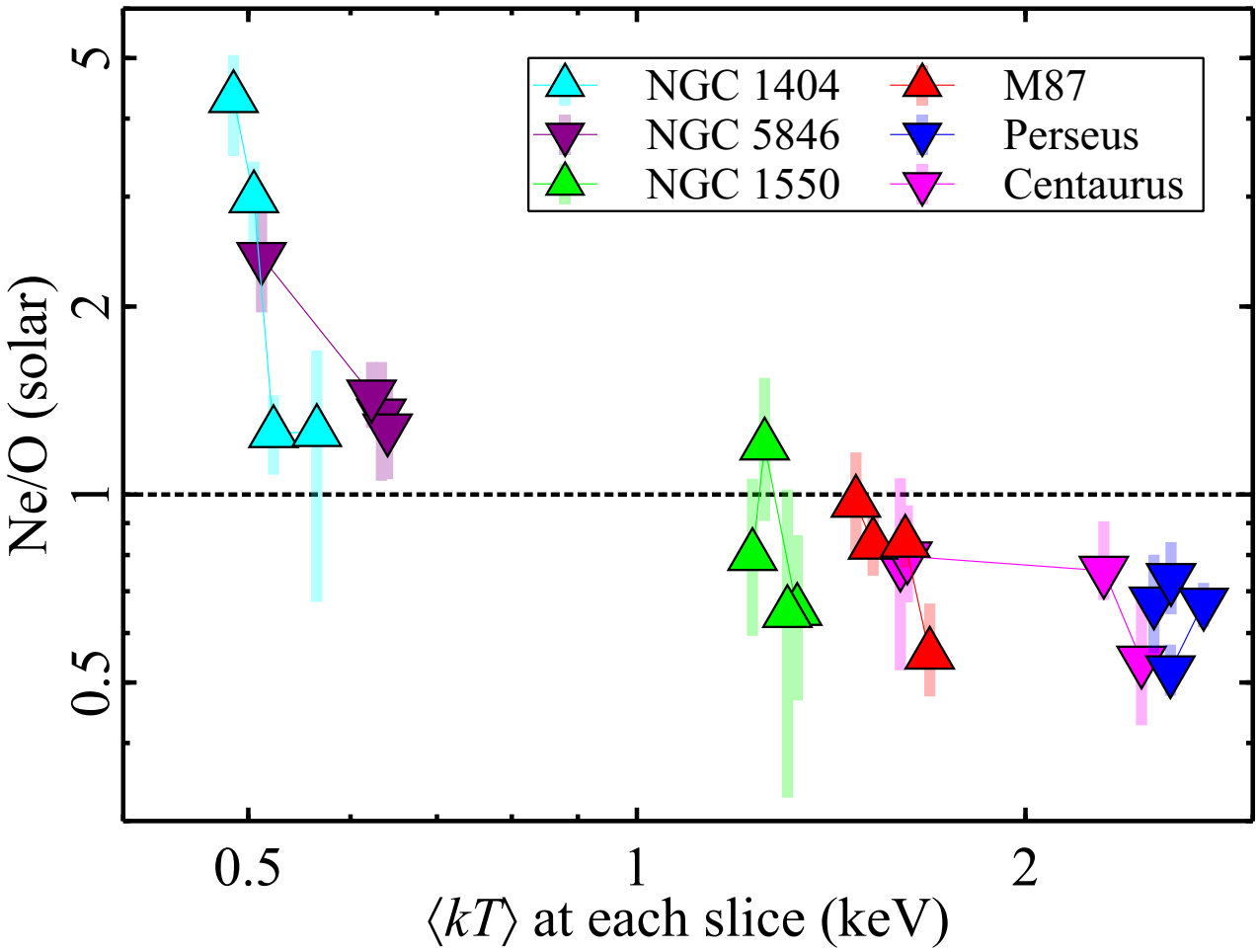

Figure 27: The Ne/O ratio plotted against local $\langle kT \rangle$ at each slice for the same objects of Fig. 26. The solar ratio is indicated with dotted lines on each panel.

each slice (Fig. 27). Interestingly, high Ne/O ratios are observed at lower temperature regions of one object, as well as at a cooler system among the sample. The possible correlation of Ne/O with $\langle kT \rangle$ suggests some systematics in the abundance estimation of cool plasmas. This will be discussed in more detail in Sect. 4.4.2.2.

4.4.2 Metal composition, $\langle kT \rangle$ and $M_{<60''}/L_B$

Here, we show trends in the metal content of various haloes in our sample. One of the most common indicators characterizing the gas phase is, of course, $\langle kT \rangle$; moreover, integrated mass-to-light ratio can be another diagnostic of haloes (e.g., Nagino & Matsushita 2009). Under the rough assumption that the emission is from a uniformly dense sphere, we computed the mass parameter by integrating the electron density in the 60 arcsec slices. Although this is not identical to the true halo mass, such a *pseudo-mass parameter* (denoted by $M_{<60''}$) is a good surrogate for the gas mass at

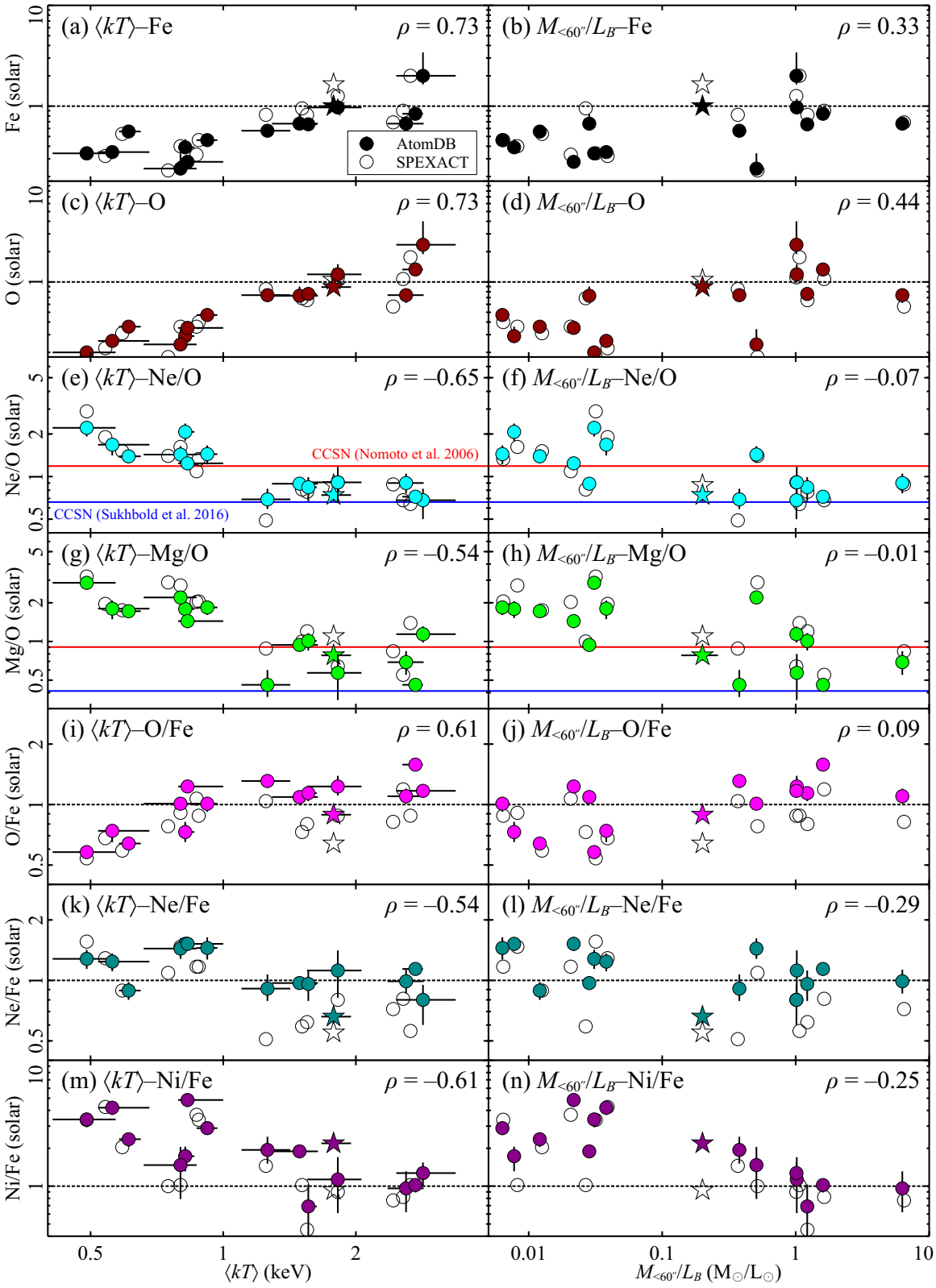

Figure 28: The Fe and O abundances and the Ne/O, Mg/O, O/Fe, Ne/Fe, and Ni/Fe ratios as functions of (a, c, e, g, i, k, m) $\langle kT \rangle$ and (b, d, f, h, j, l, n) $M_{<60''}/L_B$, respectively. The filled and open circles represent the results with AtomDB and SPEXACT, respectively. The stars indicate the results of Centaurus (Fukushima et al. 2022). Errors are shown only for the AtomDB results for viewing purposes. We also show expected ratios by two major CCSN nucleosynthesis models (Nomoto et al. 2006; Sukhbold et al. 2016) on the Ne/O and Mg/O panels. The Pearson's correlation coefficients with the AtomDB results are shown at the right-top corners of each panel.

the central part where the halo emission is dominant. By using the parameters of the Centaurus cluster, Fukushima et al. (2022) showed that the $M_{<60''}$ calculated from the RGS agrees reasonably well (~ 30 per cent) with the more accurate mass estimated by integrating the VEM profile from the CCD. Then, we adopt the B-band luminosity (denoted by L_B) given in Table 6 to calculate the mass-to-light ratio. In Fig. 28, we plot the abundances and abundance ratios as functions of $\langle kT \rangle$ and $M_{<60''}/L_B$.

4.4.2.1 Absolute abundance

A general trend is that the absolute abundances show a positive correlation to $\langle kT \rangle$ with the Pearson's correlation coefficients $\sim$ 0.7 (Figs. 28(a) and (c)). While the abundance distribution for $M_{<60''}/L_B$ has a relatively large scatter, most of the low metallicity systems are located at the low $M_{<60''}/L_B$ regime (Figs. 28(b) and (d)). Considering ongoing SN Ia enrichments in low-$M_{<60''}/L_B$ objects, it is unreasonable that these systems show lower Fe abundance than the high $M_{<60''}/L_B$ systems possibly contributed by primordial gas. Similarly, the lowest O abundances for the coolest objects (Figs. 28(c) and (d)) indicates that the C regime objects (globally identical to the low-$M_{<60''}/L_B$ ones) are less enriched with O, which is hard to interpret due to ongoing metal supplies by mass loss.

Importantly, absolute abundance measurements with RGS spectra are degenerated with continuum estimation, especially in subkiloelectronvolt plasmas. Many authors have also pointed out the systematics in such cool plasmas (e.g., Matsushita et al. 1997, 2000; Gastaldello et al. 2021; Fukushima et al. 2022). Even the CCD spectra are contaminated by continuum emissions from two-photon and free-bound processes of heavy metals in cool plasmas; therefore, absolute abundance measurements in the C or low-$M_{<60''}/L_B$ regimes are challenging with the RGS spectra that are dominated by line emissions. We suspect that this possible bias in the C regime contributes intrinsically to the observed abundance drops in the central coolest part of a system.

4.4.2.2 Ne/O and Mg/O

We also plot the Ne/O and Mg/O ratios that are dominantly expelled via mass-loss winds and CCSNe, and thus represent nucleosynthesis in a core of supergiants. There are clear interrelations for $\langle kT \rangle$–Ne/O and $\langle kT \rangle$–Mg/O; as those at the C regime are higher than the solar ratios that are uniformly observed at the W+H regime (Figs. 28(e) and (g)). In Figs. 28(f) and (h), there are no clear correlations to $M_{<60''}/L_B$ with virtually zero Pearson's correlation coefficients compared to relations

to $\langle kT \rangle$. However, it is an enigmatic picture that O, Ne, and Mg patterns of early-type galaxies contributed by stellar populations are entirely different from the ones in the medium in groups and clusters. For example, the Fornax cluster and NGC 1404 are a host and its member galaxy, respectively, belonging to the same regimes and have similar patterns. The Virgo cluster hosts NGC 4649, M49, and M87, the former two of which exhibit the super-solar Ne/O and Mg/O ratios.

Given that O and Ne share dominantly the same origin and enrichment channel, such schisms are hard to explain by a physical process. Instead, the uncertainty in the abundance measurements is currently a natural solution unless a picture of the dust formation process regains validity after the conflict with flat Ne/O profiles decreases (Fig. 26). As both AtomDB and SPEXACT give consistent ratios, this possible uncertainty depends on $\langle kT \rangle$. Different from the strong O Lyα line, the Ne Lyα and/or Ne Heα lines are not entirely resolved from the Fe L bump even with RGS (Fig. 22). Consequently, the Ne/O ratios of the coolest objects likely suffer from some systematics. If this is the case, unreasonably high Ne/O ratios in the centre of NGC 1404 (Fig. 26(d)), the coolest object in our sample, are naturally interpreted as upwardly biased values. In addition, due to the low relative intensity of Mg lines in subkiloelectronvolt plasmas, the Mg/O ratio, which is uniformly high in the C regime, would also be difficult to measure.

4.4.2.3 O/Fe and Ne/Fe

Generally, abundance ratios concerning Fe show a correlation with $\langle kT \rangle$, and have a rather weak relationship with $M_{<60''}/L_B$ (Figs. 28(i), (j), (k), and (l)). Previous studies have reported uniform abundances and ratios among objects in the broad mass range (e.g., de Plaa et al. 2007; Mernier et al. 2018c). In Fig. 28(i), the O/Fe ratio does not correlate significantly to $\langle kT \rangle$, excluding the coolest objects, which is consistent with de Plaa et al. (2017). While de Plaa et al. (2017) reported that the O/Fe ratio is uniform independent of gas temperature, including subkiloelectronvolt galaxies, recent works utilizing the most recent atomic codes give lower O/Fe ratios than those measured by them (e.g., Mernier et al. 2022). The lower O/Fe of cool objects, which may be a biased value, is *preferred* by the latest codes.

Figure 28(k) is the first robust result of the $\langle kT \rangle$–Ne/Fe relation. The Ne/Fe ratios have a negative $\langle kT \rangle$ correlation with ~ -0.5 coefficient and give a clear delimitation of $\langle kT \rangle = 1$ keV while Fig. 28(l) shows that the correlation between Ne/Fe and $M_{<60''}/L_B$ is more marginal with the Pearson's coefficient ~ -0.3. We

found a hint of an anti-correlation of Ne/Fe to $\langle kT \rangle$ different from the $\langle kT \rangle$–O/Fe relation, which is also suggested in Fig. 28(e). As well as the Ne/O ratios, these inverse properties of O and Ne to each other are unreasonable because of their origin and dispersal history.

4.4.2.4 Ni/Fe

The Ni/Fe ratios show a moderate negative correlation to both $\langle kT \rangle$ and $M_{<60''}/L_B$ (Figs. 28(m) and (n)). When objects fall on the $M_{<60''}/L_B \gtrsim 1\,\mathrm{M}_\odot/\mathrm{L}_\odot$ region, the Ni/Fe ratios are consistent with the solar ratio. The low-$M_{<60''}/L_B$ objects with $M_{<60''}/L_B \lesssim 0.1\,\mathrm{M}_\odot/\mathrm{L}_\odot$ exhibit high Ni/Fe ratios larger than 2 solar. The absence of prominent Ni lines in the RGS band (Fig. 22) prevents us from making a robust assessment of the Ni/Fe ratio. However, a high Ni/Fe ratio has also been reported for the Centaurus cluster using the CCD detectors (Fukushima et al. 2022). As indicated in many previous works, the Ni/Fe ratio is sensitive to SN Ia explosion models since a dominant fraction of Ni is synthesized at a core of exploding white dwarfs (e.g., Dupke & White 2000; de Plaa et al. 2007; Hitomi Collaboration et al. 2017; Mernier et al. 2017). This will be discussed in more detail in Sect. 4.4.3.

4.4.2.5 N enrichment

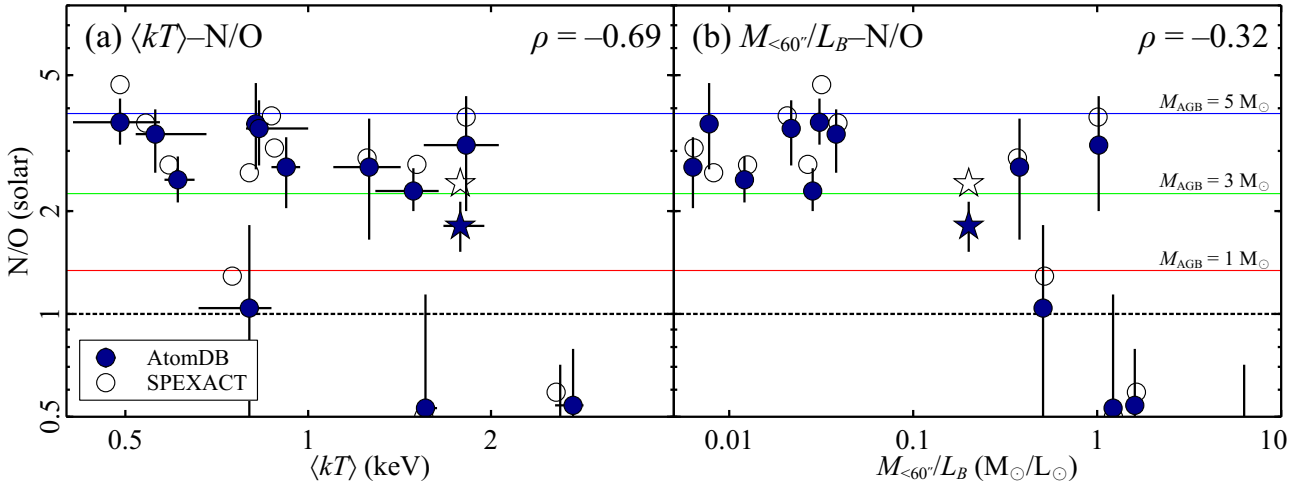

Figure 29: The N/O ratios as functions of (a) $\langle kT \rangle$ and (b) $M_{<60''}/L_B$. The filled and open circles represent the results with AtomDB and SPEXACT, respectively. The stars indicate the results of Centaurus (Fukushima et al. 2022). Errors are shown only for the AtomDB results for viewing purposes. The predicted ratios by Karakas (2010) are shown by horizontal solid lines, assuming the initial metallicity of AGBs at each mass to the solar value. The Pearson's correlation coefficients for the AtomDB results are given at the right-top corners of each panel.

The N enrichment through SNe is negligible, and they can be instead produced

Table 9: Error-weighted average abundance ratios to Fe for each subsample with AtomDB. Statistical variances are also given in parentheses.

	C	W+H	low-$M_{<60''}/L_B$	high-$M_{<60''}/L_B$
N/Fe	3.0 ± 0.2 (1.3)	1.0 ± 0.2 (2.7)	3.01 ± 0.18 (0.59)	0.6 ± 0.2 (2.9)
O/Fe	0.91 ± 0.02 (0.05)	1.50 ± 0.02 (0.10)	0.93 ± 0.02 (0.06)	1.54 ± 0.03 (0.13)
Ne/Fe	1.70 ± 0.06 (0.18)	1.09 ± 0.04 (0.02)	1.41 ± 0.04 (0.06)	1.16 ± 0.05 (0.05)
Mg/Fe	2.03 ± 0.06 (0.30)	0.92 ± 0.04 (0.06)	1.59 ± 0.05 (0.11)	0.92 ± 0.04 (0.30)
Ni/Fe	3.31 ± 0.17 (1.44)	1.24 ± 0.09 (0.19)	2.76 ± 0.13 (1.39)	1.11 ± 0.09 (0.15)

and expelled by AGB stars. We plot the N/O ratios of each object against $\langle kT \rangle$ and $M_{<60''}/L_B$ (Figs. 29(a) and (b)), comparing them to the model prediction in mass-loss winds from AGBs ($M_{\rm initial} = 1,\ 3,\ 5 M_\odot$, Karakas 2010). The N/O ratios are uniformly over-solar $\sim$ 2–4 solar among various objects, which are well explained by enrichments via AGBs $\lesssim 5\,M_\odot$. Stars in the AGB phase, which should be an ongoing enrichment channel in the central regions of early-type galaxies, are expected to account for the dominant fraction of the observed N and O. Since an early CCSN contribution to the O enrichment is undoubtedly important in accumulated halo history, directly comparing observed N/O and the AGB yields is simplistic and cannot completely exclude a possible effect of more massive AGB stars. However, Mao et al. (2019) proposed the importance of the contribution of low- and intermediate-mass stars (~ 0.9–$7\,M_\odot$) in the AGB stage to the halo enrichment. Furthermore, Kobayashi et al. (2020) also attribute the Milky Way N enrichment to intermediate-mass AGBs (4–7 $M_\odot$). Our simple estimation gives consistent results with these works.

In contrast to the global trend of high N/O ratios, some hot or high-$M_{<60''}/L_B$ objects (giant clusters like Perseus) yield N/O $\lesssim$ 1 solar. One possibility is that the mass-loss contribution is severe in the cool or low $M_{<60''}/L_B$ haloes compared to the high N/O objects. However, the N Lyα line is weak in hot gas ($\gtrsim$ 2 keV) and measuring the N abundance in the hot haloes is more challenging than in the cool ones (Mao et al. 2019). Therefore, some caution is required in inferring relationships around high temperature or high-$M_{<60''}/L_B$ regimes from Fig. 29 A more precise trend of N/O will be validated by comparing simulation studies with realistic assumptions of various initial mass functions (IMFs) and mass injection rates. Spatially-resolved analysis with non-dispersive instruments will also provide a unique way to investigate the N enrichment in early-type galaxies.

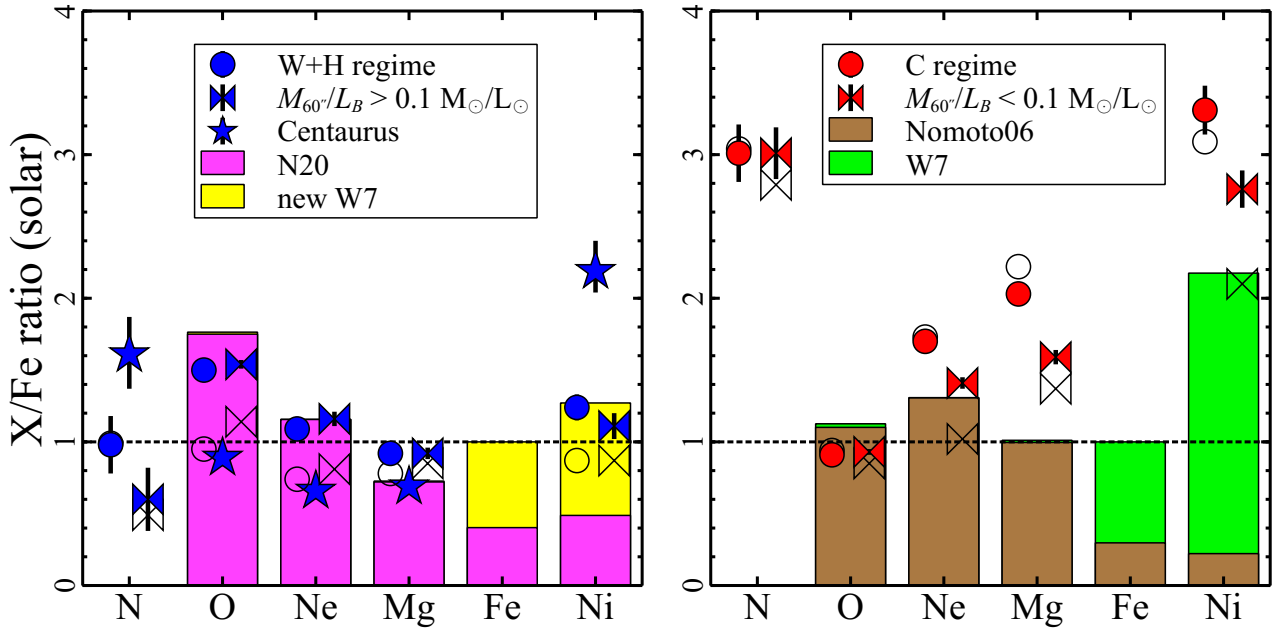

Figure 30: Abundance ratio patterns obtained in central 60 arcsec cores. The sample is divided into two subsamples using temperature regimes (circles) and $M_{<60''}/L_B = 0.1\,\mathrm{M}_\odot/\mathrm{L}_\odot$ (ties), each of which the abundance ratios are averaged. The stars represent the result of the Centaurus cluster given in Fukushima et al. (2022). Filled and open plots indicate the results of AtomDB and SPEXACT, respectively. To fit the observed pattern, we adopt two combination models of CCSN and SN Ia yields: the "classical" CCSN model (Nomoto et al. 2006) and W7 model (Iwamoto et al. 1999), and N20 model (Sukhbold et al. 2016) and new W7 model (Leung & Nomoto 2018). Every progenitor metallicity thereof is assumed to be 1 solar. For viewing purposes, only two combinations with the best χ^2/dof are presented for $M_{<60''}/L_B$ subsamples with AtomDB. See Table 10 for the results of other regimes and combinations.

4.4.3 Entire abundance patterns and SN yields

To summarize the entire trend of metal content for our sample, we calculate the error-weighted average X/Fe ratios for the four subsamples of C, W+H, low-, and high-$M_{<60''}/L_B$ (Table 9). We also show the X/Fe patterns and the best-fitting linear combinations of current SN yield models (Fig. 30 and Table 10). In the left-hand panel of Fig. 30, the ratios are plotted for the objects belonging to the W+H and high-$M_{<60''}/L_B$ regimes. The average ratios for the C and low-$M_{<60''}/L_B$ objects are shown in the right-hand panel. The result of Centaurus of Fukushima et al. (2022) is not included in averages in the left-hand panel.

We reproduce these patterns with a linear combination model of various CCSN and SN Ia nucleosynthesis calculations (e.g., Simionescu et al. 2019). We give representative results here with the latest calculations of the N20 model of Sukhbold et al. (2016) + new W7 model of Leung & Nomoto (2018), since the critical ratio of SN Ia to all SNe is typically 10–20 per cent in other combinations. The results with well-established "classical" yields of Nomoto et al. (2006) + W7 model of Iwamoto

Table 10: Number ratio of SNe Ia to total SNe at the best-fitting combination models for each regime using the AtomDB results.

	C	W+H	low-$M_{<60''}/L_B$	high-$M_{<60''}/L_B$
W7 (Iwamoto et al. 1999) + "classical" (Nomoto et al. 2006)				
SN Ia/(SN Ia+CCSN)	0.18 ± 0.05	0.18 ± 0.05	0.19 ± 0.04	0.16 ± 0.05
χ^2/dof	11.5/3	15.4/3	5.6/3	20.9/3
new W7 (Leung & Nomoto 2018) + N20 (Sukhbold et al. 2016)				
SN Ia/(SN Ia+CCSN)	0.18 ± 0.09	0.11 ± 0.02	0.17 ± 0.08	0.11 ± 0.02
χ^2/dof	32.4/3	1.9/3	25.4/3	2.0/3

et al. (1999) are also reported for comparison. The IMF of Salpeter (1955) is used to average over various progenitor masses for CCSNe. We exclude yield calculations for SNe Ia with a sub-Chandrasekhar mass white dwarf because specific elements, such as Ca or Cr, are completely absent from our patterns in Fig. 30.

The N/Fe ratios are also plotted in Fig. 30 for referential results. The AGB contribution will be included in the combination model to reproduce the N abundance by parameterizing the number of certain mass stellar populations. However, this additional component has little effect on the other metals used in Fig. 30, since the N enrichment due to SN explosions is negligible (Mao et al. 2019). Moreover, the method utilized to fit the SN abundances gives up information on the temporal evolution, which makes it difficult to separate the individual SN contributions from the AGB ones, because the ejecta of the early CCSN and SN Ia had formed stars that are now in the AGB phase. Therefore, the N/Fe ratios are not used to fit the patterns in this study.

4.4.3.1 Hot or High-$M_{<60''}/L_B$ objects

In the left-hand panel of Fig. 30, both patterns of the W+H and high-$M_{<60''}/L_B$ regimes are in plausible agreement with each other for O/Fe, Ne/Fe, Mg/Fe, and Ni/Fe. The O/Fe, Ne/Fe, and Mg/Fe ratios are close to the solar ratios. This pattern is reproduced well by the latest N20 model of Sukhbold et al. (2016), also suggested in the Ne/O and Mg/O plots (Figs. 28(e) and (g)). We found that the Ni/Fe ratio is also about 1 solar, especially for SPEXACT, and prefers the new W7 calculation by Leung & Nomoto (2018). The sub-solar N/Fe ratio of high-$M_{<60''}/L_B$ objects compared to the W+H ones, still cautious to directly accept this trend (see Sect. 4.4.2.5), implies the SN Ia effect in systems with long-timescale enrichment. Such a trend is also predicted by simulation study (e.g., Kobayashi et al. 2020). For these patterns, the ratio of SNe Ia to total SNe is $\sim$ 11 per cent (Table 10), contributing to 60 per cent

of observed Fe. These results are globally consistent with the results for the Perseus cluster (Simionescu et al. 2019). While the two codes give consistent results within the atomic code uncertainties (see Sect. 4.3.4), the O/Fe ratio with SPEXACT is closer to the solar value than with AtomDB, which is also indicated in Simionescu et al. (2019).

Notably, the O/Fe, Ne/Fe, and Mg/Fe ratios of Centaurus are slightly smaller than the other objects in the same regime. Fukushima et al. (2022) suggest a significant contribution of SN Ia in this object in comparison to other cool core systems. High N/Fe and Ni/Fe ratios also distinguish the Centaurus cluster from the others. This object likely shows an intermediate property of enrichment channels between the two temperature regimes (e.g., mass-loss winds, SNe, primordial gas), which is also implied by medium $\langle kT \rangle$ and $M_{<60''}/L_B$ among our sample (Fig. 28). Interestingly, a recent cosmological simulation predicts sub-solar O/Fe, Ne/Fe, and Mg/Fe ratios (Fukushima et al. 2023a) agree with our observed pattern of the Centaurus cluster. While there can still be some uncertain factors in the simulation (e.g., the delay time distribution of SN Ia, mass-loss rate, IMF), traditional linear combination modelling is too simplistic for discussing halo enrichment. We need closely coordinated observations, simulations and theoretical modelling in the next era of high-resolution spectroscopy missions.

4.4.3.2 Cool or Low-$M_{<60''}/L_B$ objects

We find that the C or low-$M_{<60''}/L_B$ regime shows the solar O/Fe ratio with both codes of AtomDB and SPEXACT (right-hand panel of Fig. 30). Therefore, these objects prefer the "classical" CCSN model of Nomoto et al. (2006). The Ne/Fe and Mg/Fe ratios are globally higher than the O/Fe, especially with AtomDB. This is also implied in the Ne/O and Mg/O ratios (Figs. 28(e), (f), (g), and (h)). High Ne/Fe and Mg/Fe ratios are not reproduced well by our SN combination models with high χ^2/dof (Table 10). In particular, the combination of the latest SN models for the C regime (Sukhbold et al. 2016; Leung & Nomoto 2018) yield the worst χ^2/dof value among all trials (Table 10). Additionally, the Ni/Fe ratios are higher than 2 solar that even exceeds the high predictive value of the "classical" W7 calculation by Iwamoto et al. (1999). On the other hand, super-solar N/Fe ratios are explained by mass-loss winds from 3–4$M_\odot$ stars in the AGB stage, consistent with the picture provided in Sect. 4.4.2.5. The best-fitting combination model suggests that the SN Ia ratio to total SNe is $\sim$ 20 per cent (Table 10), where SNe Ia are responsible for 70 per cent of all

Fe.

4.4.4 Future prospects

As discussed in Sects. 4.3.4 and 4.4.3, the state-of-the-art atomic codes and emission models are still limited and endeavoured. Hence, future X-ray missions with high-resolution spectroscopy such as *XRISM* (XRISM Science Team 2020) and *Athena* (Nandra et al. 2013) are strengthening more and more importance. For example, the Resolve instrument on *XRISM* obtained at a great spectral resolution < 7 eV will offer entirely resolved spectra within the Fe-L complex band even in subkiloelectronvolt plasmas.

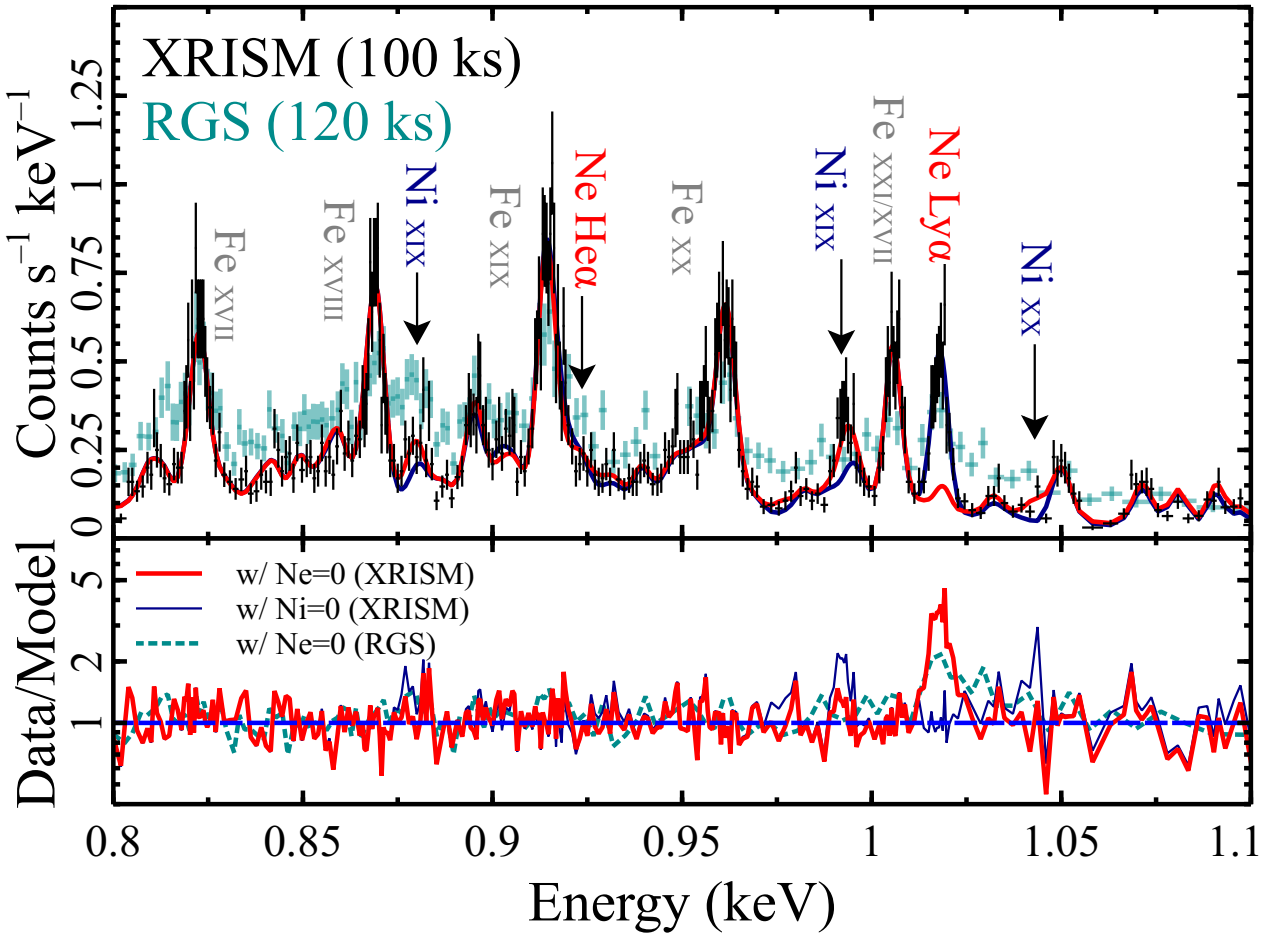

Figure 31: Simulated *XRISM* spectrum of the central arcmin scale of NGC 4649. The current RGS data within the 60″ region is also plotted in dark cyan. The red and dark blue lines represent the best-fitting models without Ne and Ni lines, respectively. Prominent emission lines are marked on the upper panel.

In Fig. 31, we show a simulated Resolve spectrum of NGC 4649 that exhibits $\langle kT \rangle \sim 0.8$ keV and the strongest Ne Lyα emission among the three coolest objects

in Table 7. The Ne Lyα is wholly resolved from the Fe-L bump with excellent sharpness and significance in the simulated spectrum. Determining the Ne abundance accurately enables us to address our proposed Ne issues with the current RGS data more confidently (Sects. 4.4.1, 4.4.2.2, and 4.4.2.3). For example, we will discuss whether the high Ne/O ratio in the subkiloelectronvolt haloes is real or an artefact. This is important for decisively favouring or abandoning the dust formation effect in early-type galaxies. We also expect that observing cool and metal-rich objects with O, Ne, and Mg lines impacts the theoretical research of CCSNe and the nucleosynthesis process in supergiants.

Furthermore, we will reveal some information on Ni-L emissions, which are hidden below the continuum emission in current RGS spectra, by detecting their lines as relatively sharp line structures. The clear detection of Ni-L lines in cool plasma allows us to make robust measurements of the Ni abundance, even though the Ni K-shell emissions are absent in observed objects. As indicated in Sect. 4.4.2.4, the super-solar Ni/Fe ratio is observed in such cool systems. Measuring the Ni/Fe ratio with clear emission lines in these objects will significantly improve our current unclear knowledge of SN Ia in early-type galaxies that are less enriched and assembled than are groups or clusters. In addition, the study of SNe Ia in early-type galaxies will be an invaluable complement to the *Hitomi* results of the Perseus cluster (Hitomi Collaboration et al. 2017; Simionescu et al. 2019), which is one of the most evolved objects. The anomalously high Ni/Fe ratio in the Centaurus cluster will also be discussed in more detail.

Finally, we stress that spectra with well-resolved Fe- and Ni-L lines are an ideal *laboratory* to examine the atomic codes such as AtomDB and SPEXACT. Although significant efforts in laboratory measurements have improved these codes and have reduced uncertainties among them (e.g., Gu et al. 2019, 2020, 2022), some disagreements between the two codes lead to controversy in current observational studies, especially around Fe-L lines in cool plasma (e.g., Gastaldello et al. 2021; Fukushima et al. 2022). In tandem with progressive laboratory physics, high-resolution spectroscopic observations will help us *Fe-ing* the persistent wrinkles out of the atomic codes [24].

[24] Strange to think that ironing a shirt seems more difficult to the author. Praised be those who do housework properly.

Chapter 5

Abundance Pattern and Charge-exchange Emission in M82

5.0 Statement

This chapter consists of an unpublished manuscript before the peer-review process: *"Revisiting the abundance pattern and charge-exchange emission in the M82 centre"* by **K. Fukushima**, S. B. Kobayashi, and K. Matsushita (submitted to Astronomy & Astrophysics).

5.1 Introduction

Core-collapse supernovae (CCSNe), which originate from massive star progenitors, play a crucial role in the evolution of galaxies. They are primary sources of light α-elements such as O, Ne, and Mg (e.g., Nomoto et al. 2013). Additionally, they heat the interstellar medium (ISM) to X-ray-emitting temperatures. In starburst galaxies, particularly in regions of active star formation, CCSNe can induce powerful winds from the galactic disc. These winds, also known as outflows, are essential in enriching the intergalactic medium, which links the ISM and the local universe (Orlitova 2020, for a comprehensive review). Consequently, X-ray observations of starburst galaxies offer valuable insights into the processes supplying energies and metals into both the ISM and circumgalactic spaces.

In recent years, numerous X-ray observations have focused on the extended X-ray-emitting ISM in starburst galaxies (e.g., Strickland et al. 2004; Yamasaki et al. 2009; Konami et al. 2012; Mitsuishi et al. 2013; Yang et al. 2020). The M82 galaxy, a well-established starburst system located at a distance 3.53 Mpc from our Solar System (Karachentsev et al. 2004), has been a key object among these studies. The

nearly edge-on orientation makes it an ideal laboratory for studying biconical outflows originating from the central region of the galaxy (e.g., Strickland & Heckman 2009; Zhang 2018). These outflows exhibit a multiphase structure, which is characterized by infrared, Hα, and X-ray emissions (Strickland et al. 1997; Lehnert et al. 1999; Read & Stevens 2002; Engelbracht et al. 2006; Zhang et al. 2014; Lopez et al. 2020). Strickland & Heckman (2007) found diffuse Fe Heα emission in the central regions, suggesting the presence of gas at temperatures of several kiloelectronbolts. Additionally, strong emission lines of elements such as O, Mg, Si, S, and Fe have been detected from the core to the wind regions of the galaxy (e.g., Tsuru et al. 1997, 2007; Ranalli et al. 2008; Konami et al. 2011). In the central regions, these elements exhibit an unusual abundance pattern: super-solar ratios of Ne/O and Mg/O (> 1.5 solar) with super-solar O/Fe ratios have been reported (e.g., Tsuru et al. 1997; Ranalli et al. 2008; Konami et al. 2011; Zhang et al. 2014). This contradicts the existing nucleosynthesis models of CCSN. In contrast, the outflowing gas outside the disc shows an abundance pattern consistent with CCSN predictions(Tsuru et al. 2007; Konami et al. 2011).

An additional exciting feature in M82 is the presence of charge exchange (CX) X-ray emission. This process, where one or more electrons are transferred from cold neutrals to highly ionized atoms, resulting in X-ray emission lines through the de-excitation of these ionized particles (e.g., Gu & Shah 2023). It is expected that CX emissions will be observed at the fronts of hot gas flows colliding with cold matter. A notable feature of the CX process is the O VII triplet, which exhibits an enhanced forbidden line at 0.56 keV, compared to the resonance line at 0.57 keV [25]. Liu et al. (2012) analysed the data from the Reflection Grating Spectrometer (RGS) on board *XMM-Newton* and reported this enhancement in the O VII triplet in several starburst galaxies, suggesting a significant CX contribution in addition to plasma in a collisional ionization equilibrium (CIE) state. Konami et al. (2011) and Lopez et al. (2020) included the CX component in their analysis of the CCD spectra from M82, although their spectral resolution is limited. Zhang et al. (2014) used the RGS data from an *XMM-Newton* observation of M82 and estimated that the interaction area between the neutral and ionized matter is significantly larger than the geometry surface area of the galaxy.

[25] In the CX process, an electron is transferred to the outer shell ($n = 3, 4$, e.g., Cravens 2002) of a projectile ion. Then, de-excitation from the high-n state causes enhancements of Lyγ and δ lines for H-like ions. For He-like ions, the forbidden line is also formed by cascade transition from outer triplet shells.

The RGS on board *XMM-Newton* is adequate for our study, offering good spatial and spectral resolution within the ~ 0.5–2 keV band. This makes it particularly useful for measuring α-element abundances and estimating the CX contribution. However, it is important to note that the dispersion effect and source spatial information are degenerated along the dispersion direction, leading to decreased resolving power for extended emissions (Mao et al. 2023, for a recent review). Consequently, careful treatment is required when analysing the RGS spectra of galaxies, especially for the broadening effect on each emission line (e.g., Chen et al. 2018; Yang et al. 2020; Fukushima et al. 2023b). In this study, we used deep 300 ks RGS data obtained with different position angles to model the spectra of the central region of M82 to determine its temperature structure, the CX contribution, and the abundance pattern. This chapter is structured as follows. Section 5.2 summarizes the *XMM-Newton* observations and data reduction. In Sect. 5.3, we outline the line-broadening effect intrinsic to the RGS analysis. Section 5.4 presents the general prescription for our fitting and the results. We will discuss and interpret our findings in Sect. 5.5. We assume cosmological parameters as $H_0 = 70\,\mathrm{km\,s^{-1}\,Mpc^{-1}}$, $\Omega_\mathrm{m} = 0.3$, and $\Omega_\Lambda = 0.7$. The proto-solar abundance of Lodders et al. (2009) is adopted to estimate element abundances.

5.2 Observations and Data Reduction

We analysed the archival observation data of the M82 centre with RGS installed on *XMM-Newton*. Table 11 summarizes the observations used in this work. The M82 nucleus (Lester et al. 1990) is located near the centre of the MOS detecter for these observations. The RGS data were processed using the `rgsproc` task wrapped in the *XMM-Newton* Science Analysis System (SAS) version 18.0.0. We obtained light curves from the CCD9 on the RGS focal plane (den Herder et al. 2001); and next, the mean count rate μ and standard deviation σ were derived by fitting these curves with a Gaussian. In order to discard background soft-proton flares, the count rate threshold as $\mu \pm 2\sigma$ was applied to uncleaned events. Following the SAS team, other standard screening criteria were employed. The cleaned exposure times of each observation are in Table 11.

Table 11: The RGS observations analysed in this work.

ObsID	Date	Exposure[a] (ks)	Position angle[b] (deg)
0112290201	2001 May 06	19.2	293
0206080101[c]	2004 Apr 21	55.3	319
0560590101	2008 Oct 03	27.8	138
0560181301	2009 Apr 03	22.9	316
0560590201	2009 Apr 17	15.1	316
0560590301	2009 Apr 29	21.4	296
0657800101	2011 Mar 18	22.8	330
0657801701	2011 Apr 11	21.4	312
0657801901	2011 Apr 29	11.6	296
0657802101	2011 Sep 24	12.4	147
0657802301	2011 Nov 21	9.2	100
0870940101	2021 Apr 06	28.6	313
0891060101	2021 Oct 17	26.8	127
0891060401	2022 Apr 06	32.1	313

[a] Half the sum of the RGS1 and RGS2 exposures after the deflaring procedure.
[b] The angle of the RGS dispersion axis measured eastwards from the celestial north.
[c] The data set analysed in Zhang et al. (2014).

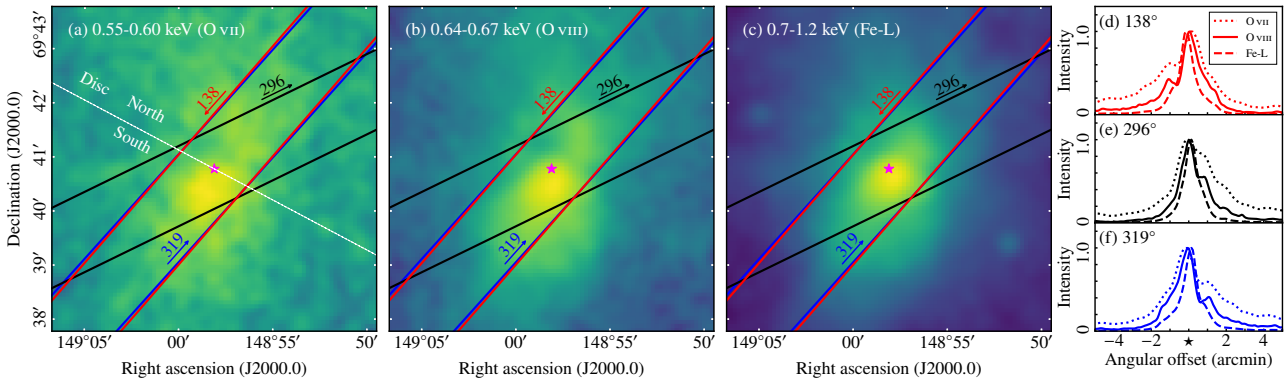

Figure 32: (a) Mosaiced X-ray count image of the M82 centre in the O VII (0.55–0.60 keV) band by CCDs. The representative three RGS position angles are overlaid with the 80 arcsec cross-dispersion widths. The arrows indicate each dispersion direction in which the photons are scattered into the higher energy side. The star marker and the solid line passing through it indicate the M82 centre and disc (Lester et al. 1990; Mayya et al. 2005). (b, c) Same as (a), but in the O VIII Lyα (0.64–0.67 keV) and Fe-L (0.70–1.20 keV) bands. (d) Normalized count profiles projected on to the 138° dispersion axis in the 0.55–0.60 keV (O VII), 0.64–0.67 keV (O VIII), and 0.70–1.20 keV (dominated by Fe-L lines) bands. The angular offset is measured in reference to the star marker in (a), where the positive side of the offset axis is the higher energy part in diffracted spectra. (e, f) Same as (d), but along the dispersion axes of 296° and 319°, respectively.

5.3 Imaging Analysis

In Figs. 32(a), (b), and (c), we show X-ray images of the M82 centre for the O VII (Fig. 32(a), 0.55–0.60 keV), O VIII Lyα (Fig. 32(b), 0.64–0.67 keV), and Fe-L (Fig. 32(c), 0.70–1.20 keV) bands. In these images, the outflows extending from the disc towards the southeast and northwest are visible, especially in Figs. 32(a) and (b). The dispersion directions for the three representative position angles are overlayed. The 80 arcsec cross-dispersion width covers a significant part of the two outflow regions. Incorporating data from different position angles helps resolve the degeneracy between energy and spatial position along the dispersion angle, allowing for a more detailed analysis of the outflow structure.

The X-ray count profiles within an 80 arcsec cross-dispersion width along each dispersion axes are given in Figs. 32(d), (e), and (f). These profiles show significant differences across the three bandpasses. In particular, the Fe-L line band is characterized by a centrally peaked and narrow distribution on a spatial scale of 1–2 arcmin. In contrast, the O VII band exhibits the most broadened profiles. In both the O VII and O VIII profiles, a dip is observed at ~ 1 arcmin offset northward from the galaxy centre. The two peaks beside the dip correspond to the outflows towards the southeast and northeast. This bimodal line profile in the O band, along the centrally-peaked distribution in the Fe-L line band, has been reported by Zhang et al. (2014). This double-peak structure, especially in the O VIII band profile, depends on the dispersion direction (Figs. 32(d) and (f)).

5.4 Spectral Analysis

5.4.1 General prescription

The RGS instrument provides spectra within a 5 arcmin cross-dispersion width (centred on MOS) along the dispersion direction (e.g., Zhang et al. 2019; Narita et al. 2023). Following the method described in Fukushima et al. (2022, 2023b), we extracted first-order RGS spectra, setting the cross-dispersion width to 80 arcsec, centred on the M82 nucleus. The cross-dispersion widths and dispersion directions for three representative position angles are plotted in Figs. 32(a), (b), and (c). The RGS1 and RGS2 spectra and response matrices are co-added through the `rgscombine` script. With the RGS, line broadening in a first-order spectrum is observed as $\Delta\lambda = 0.138\Delta\theta$ (e.g., Mao et al. 2023), where $\Delta\lambda$ and $\Delta\theta$ represent the line broadening and the

spatial extent in the wavlength (10^{-8} cm) and dispersion (arcmin) axes, respectively. This difference is comparable to the energy separation between the forbidden and resonance lines in the O VII triplet.

RGS is primarily designed for observing point-like sources; therefore, the response matrices generated by the standard SAS method are unsuitable for analysing diffuse emissions from various extended sources, such as supernova remnants, galaxies, and clusters (e.g., Chen et al. 2018; Tateishi et al. 2021; Fukushima et al. 2023b). To fit the RGS spectra of these extended sources, it is necessary to convolve the response matrix with the projected surface-brightness profile along the dispersion direction (e.g., Tamura & Ohta 2004; Mao et al. 2023). Moreover, variations in spatial broadening across different energy bands necessitate applying different convolution scales for distinct spectral components. The differences in the spatial distribution of the O VII, O VIII, and Fe-L band images (see Sect. 5.3) imply the presence of multiple thermal CIE components with different spatial scales. Zhang et al. (2014) carefully analysed the RGS spectra of M82, adopting two spectral broadenings: bimodal soft emission and centrally-peaked hard emission. In the subsequent part, we further test different spatial broadenings for the spectra components emitting O VII and O VIII lines.

We use the XSPEC package version 12.10.1f (Arnaud 1996) but with the revised ATOMDB version 3.0.9 (Smith et al. 2001; Foster et al. 2012) that provides information on the line and continuum emissions at two hundred and one temperatures from 8.6×10^{-4} to 86 keV. This updated ATOMDB is implemented standardly in XSPEC version 12.11.0k or later [26]. The C-statistic method (Cash 1979) is adopted in our spectral fitting to estimate the spectral parameters and the error ranges thereof without bias (Kaastra 2017). Each spectrum is re-binned to have a minimum of 1 count per spectral bin.

5.4.2 Spectral models

In our RGS spectral analysis, we will reproduce the diffuse ISM emission (denoted by $\mathrm{ISM_{M82}}$). Two individual absorptions modify the $\mathrm{ISM_{M82}}$ component. We assume $6.7 \times 10^{20}\,\mathrm{cm^{-2}}$ for the Galactic extinction (Willingale et al. 2013). The intrinsic absorption of M82 for diffuse emissions is typically (1–3) $\times 10^{21}\,\mathrm{cm^{-2}}$ (e.g., Konami et al. 2011; Zhang et al. 2014); thus, we use the fixed value $2 \times 10^{21}\,\mathrm{cm^{-2}}$. The photoelectric absorption cross-sections are retrieved from Verner et al. (1996). Letting these absorption parameters free does not significantly change the results we

[26] http://www.atomdb.org

demonstrate below. We do not include diffuse astrophysical background emissions such as the cosmic X-ray background or Milky Way halo component in our spectral fitting since they contribute to the observed RGS spectra just as flat components. A power-law component is introduced to account for increasing flux at low energies below 0.5 keV. We use another power-law component with a 1.6 photon index (Ranalli et al. 2008) subjected to 2×10^{22} cm^{-2} extinction to take the point source emission into account.

The complete model applied to the observed spectra is represented as $\texttt{phabs}_{\rm Gal} \times (\texttt{phabs}_{\rm M82} \times {\rm ISM}_{\rm M82} + \texttt{phabs}_{\rm PS} \times \texttt{powerlaw}_{\rm PS}) + \texttt{powerlaw}_{\rm BKG}$. To account for the line broadening effect on $\rm ISM_{M82}$ described in Sects. 5.1 and 5.3, we use the XSPEC model `rgsxsrc` with mosaiced CCD (MOS+pn) images in specific bands. We first perform spectral fits in two local bands: the O VIII band (0.60–0.77 keV, Sect. 5.4.3) and O VII band (0.45–0.62 keV, Sect. 5.4.4), each convolved with the respective images. Then, we fit the broadband spectra covering the full RGS energy range of 0.45–1.75 keV (hereafter broadband; Sect. 5.4.5), using the image of this band, which closely resembles the Fe-L band image. The spatial distribution of each emission line may not precisely match the image of its corresponding energy band, as these bands also include continuum emissions. The image convolution approach in this study, as well as its predecessors, is an approximation, and the resulting systematic uncertainties will be discussed in further sections.

5.4.3 *Results of O VIII Lyα line*

First, we test the thermal plasma component in collisional ionization equilibrium (CIE) convolved with the O VIII band image: $\rm ISM_{M82}$ = `vapec` (the CIE modelling). We ignore the point source contribution due to quite a strong intrinsic absorption for the point sources at the M82 centre ($\gtrsim 1 \times 10^{22}$ cm^{-2}, e.g., Brightman et al. 2016). Despite focusing on local line structures, in the spectral fittings, we use a wider energy range of 0.60–0.77 keV, including the Fe XVII line around 0.73 keV. This approach enabled more robust measurement of global parameters such as kT; restricting to "local fits" lead to poorly constrained values (e.g., Lakhchaura et al. 2019). The combined spectrum of each observation is fitted with free parameters of kT, emission measure (EM), and the O and Fe abundances.

The CIE modelling approximately reproduces the observed spectra (Fig. 33(a)), achieving good C-statistics/dof values $\lesssim 1.2$ (Fig. 34(a)). However, a spectral subpeak corresponding to the northward wind region at ~0.65 keV and ~0.66 keV for the

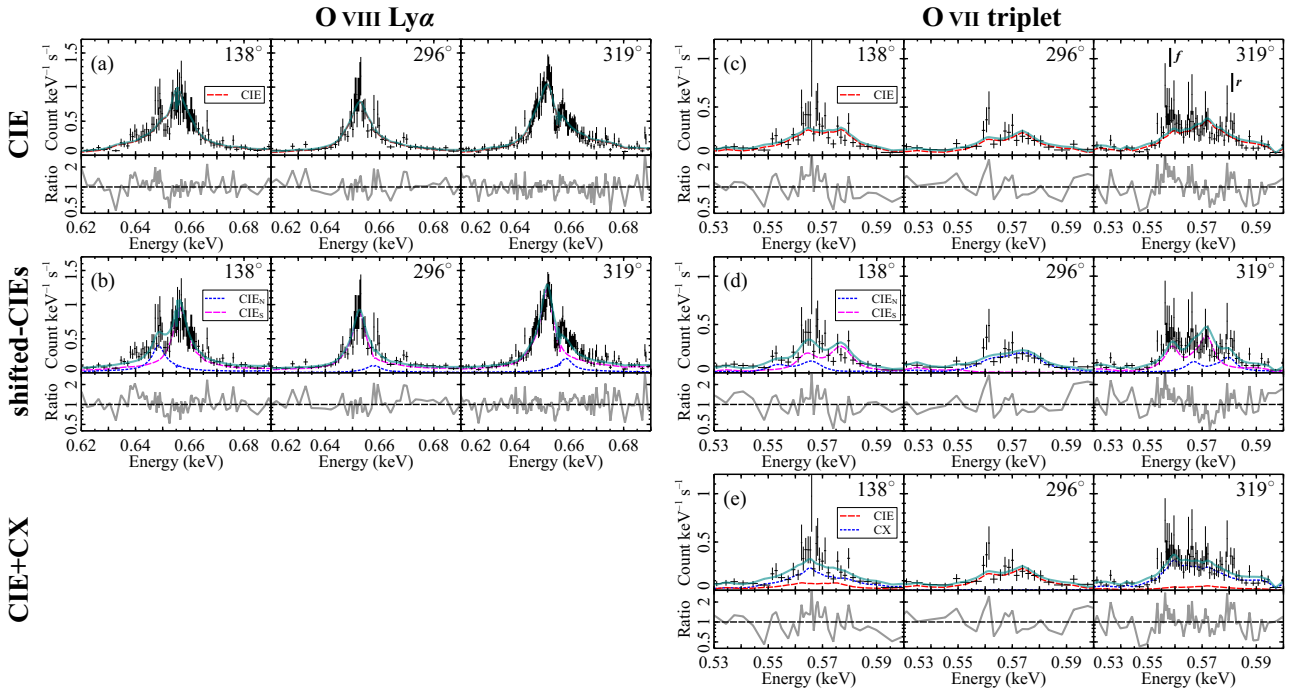

Figure 33: The RGS spectra of the M82 centre in the O VIII (a, b) and O VII (c, d, e) bands for the three representative position angles. The best-fitting models and the data-to-model ratios for the three methods are plotted: the CIE modelling convolved with local band images (the first row), the shifted-CIEs modelling convolved by the broadband image (the second row), and the CIE+CX modelling convolved with the O VII band image (the third row, only for the O VII lines). The positions of the O VII forbidden and resonance lines are labelled in the 319° panel of (c).

position angle of 138° and 319°, respectively, appears narrower than the spectral model convolved with the O VIII band image. The derived $kT_{\rm CIE}$ values are plotted against the RGS position angle in Fig. 34(b), yielding a uniform $kT_{\rm CIE}$ with a median of 0.49 keV and a 16–84th percentile range of 0.47–0.53 keV.

To reproduce the double-peak structure, we then try two spatially distinct components with varying redshift parameters to represent different spatial positions: $\mathrm{ISM_{M82}} = \mathtt{vapec}_{\rm N} + \mathtt{vapec}_{\rm S}$ (the shifted-CIEs modelling). Here, subscripts "N" and "S" represent the northeast and southwest emission peaks, respectively. The temperature and metal abundances of the two components are assumed to have the same values. Each CIE component is convolved with the broadband image (0.45–1.75 keV). While our subscript nomenclature is not an *a priori* assumption, it fits the observed spectra, as shown in (Fig. 33(b)), including the subpeak structure for the northward wind. Good C-stat/dof values are derived on the O VIII line (Fig. 34(a)). This model yields similar temperatures with the CIE modelling (Fig. 34(b)). The $\mathrm{EM_S/EM_N}$ ratios are greater than unity for all position angles (Fig. 34(c)): the brighter $\mathtt{vapec}_{\rm S}$ is shifted to the harder side and the softer side when the dispersion angle is inverted (Fig. 33(b)). This variation naturally arizes due to minor differences among RGS

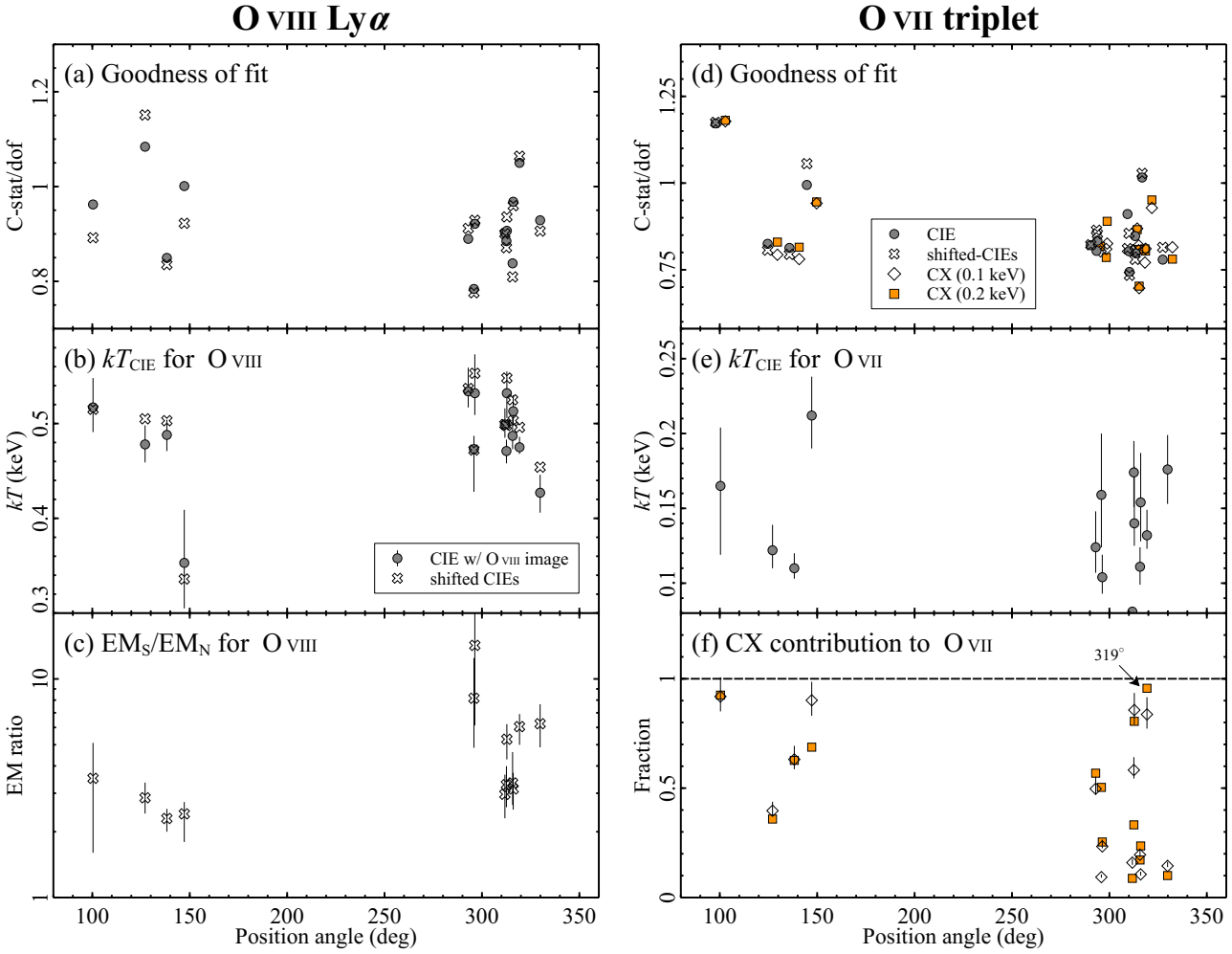

Figure 34: (a) Temperatures derived from the two modellings on the 0.60–0.77 keV band (O VIII and Fe XVII) plotted against the RGS position angle. (b) Differences between the CIE and the shifted-CIEs modellings for C-stats/dof. (c) The EM_S/EM_N profile obtained from the shifted-CIEs method. (d) Same as (a), but with the CIE modelling on the 0.45–0.62 keV band (N VII and O VII). (e) Differences between the CIE and the shifted-CIEs (kT = 0.14 keV) methods for local C-stat/dof values (0.53–0.62 keV). (f) Same as (e), but between the CIE and CIE+CX (kT_{CIE+CX} = 0.1 and 0.2 keV) models. (g) The CX component contribution to the O VII triplet features estimated using the CIE+CX method. The grey lines on (b), (e), and (f) indicate the identity line.

slices. Thus, our shifted-CIEs method approximates successfully and reasonably the spatial variation and broadening of the O VIII Lyα line; that is, two CIE components with the broadband image can be a surrogate for an actual emission plasma broadened as the O VIII band image.

5.4.4 Results of O VII triplet lines

For the O VII triplet feature, we also start with the CIE modelling with the O VII band image: $\mathrm{ISM_{M82}}$ = `vapec`. The ignorance of the point-source contribution aligns with Sect. 5.4.3. On the same philosophy of the O VIII Lyα band analysis, we utilize the 0.45–0.62 keV band, including the N VII line at 0.5 keV. The spectra are fitted with free parameters of kT, emission measure (EM), and the N and O abundances. As shown in Fig. 33(c), the best-fit CIE models, convolved with the O VII band image, closely resemble the observed line profile of O VII. We obtain good C-stat/dof for all dispersions (Fig. 34(d)). A hint of residuals is seen at the forbidden line energy of 0.56 keV, although their significance is relatively tiny. For example, in the 319° angle, which exhibits the largest residual, it remains at $\sim 3\sigma$. The CIE modelling for O VII provides a uniform kT_{CIE} across the position angles as does the O VIII band one (Fig. 34(e)). The median value and 16–84th percentile range for kT_{CIE} are 0.14 keV and 0.11–0.18 keV, respectively.

Next, we apply the shifted-CIEs modelling for O VII taking into account its marginal bimodality: $\mathrm{ISM_{M82}}$ = $\mathtt{vapec_N}$ + $\mathtt{vapec_S}$. Each CIE component is convolved with the broad RGS bandpass (0.45–1.75 keV). We set the temperature of the two CIE components to kT = 0.14 keV based on the results of the CIE modelling. This model effectively fits the broadened O VII lines (Fig. 33(d)), yielding C-stat/dof values similar to those from the CIE modellings (Fig. 34(d)) The significance of the residuals at 0.56 keV decreased to a maximum of 2σ. For certain datasets, including that for the position angle of 296°, a single CIE component is sufficient to represent the spectra, where the dominant component likely corresponds to the bright southwest outflow.

The hint of residuals at 0.56 keV might be attributable to CX. To constrain the contribution of the CX component, we employ the second version of the AtomDB CX Model ACX (Smith et al. 2014), together with a CIE plasma: $\mathrm{ISM_{M82}}$ = `vapec+vacx` (the CIE+CX modelling). Both components are convolved in this model with the O VII band image. The collision velocity between ions and atoms is set to moderate values 200 km s^{-1} (e.g., Cumbee et al. 2016; Zhang 2018). We assumed that the CIE and CX components share the same temperature (and abundance), testing two temperature

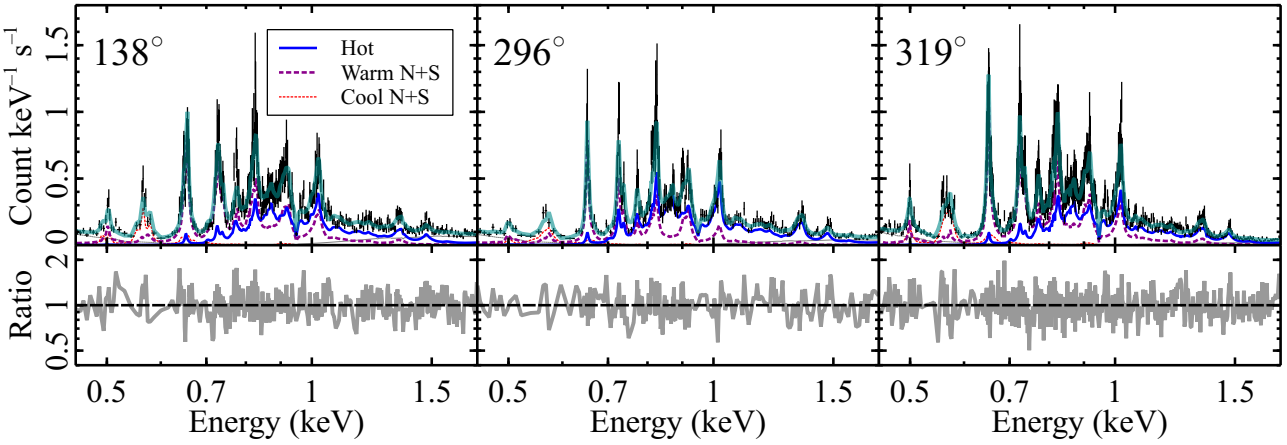

Figure 35: The best-fitting models to the broadband RGS spectra of the M82 centre for the three position angles. Thin dotted and solid lines represent the background and point-source components, respectively (see Sect. 5.4.1).

assumptions of $kT = 0.1$ and 0.2 keV. The CIE+CX model also gives fine-fits for all spectra under both temperature assumptions (Figs. 33(e) and 34(d)). However, this CIE+CX modelling still resulted in similar residuals around the forbidden line at a level of $\sim 2\sigma$ at most. Additionally, Fig. 34(g) shows that at certain position angles, the CX emission significantly exceeds the CIE contribution, reaching up to 96 per cent at 319°, *AND VICE VERSA*. There is no clear correlation between the CX fraction and position angle; for example, similar angles yield significantly different CX fractions. The lack of a consistent pattern leads to the conclusion that the CIE and CX models may not be physically plausible.

The minor residuals observed at 0.56 keV correspond to the energy of the forbidden line of O VII for the bright southward wind component. We attempted to introduce a spatially narrower CX component to fill the residuals. We modified the CIE+CX model by replacing the broader CX component with a more localized and less broadened one. Despite these modifications, the updated model does not change our results nor improve spectral fits, making it challenging to assert the robust presence of the CX emission based on the current RGS data.

5.4.5 Results of broadband spectra

Finally, we fit the broadband RGS spectra (0.45–1.75 keV), excluding the CX model from this analysis. Our adopted model is $\mathrm{ISM_{M82}} = \mathtt{vapec}_{\mathrm{hot}} + \mathtt{vapec}_{\mathrm{warmN}} + \mathtt{vapec}_{\mathrm{warmS}} + \mathtt{vapec}_{\mathrm{coolN}} + \mathtt{vapec}_{\mathrm{coolS}}$. All of the CIE components are convolved with the broadband image. As described in Sects. 5.4.3 and 5.4.4, two CIEs for the cool and warm plasma, when convolved with the broadband image, effectively

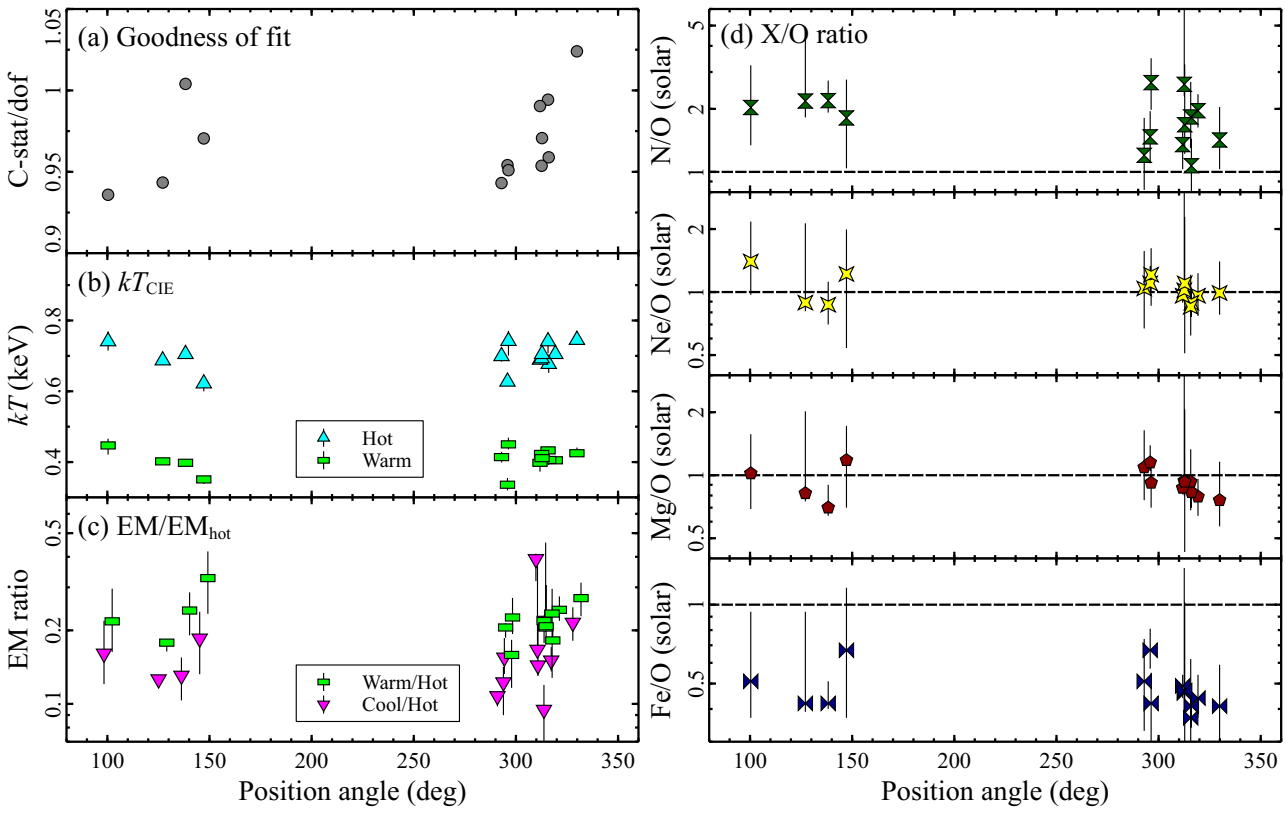

Figure 36: (a) Temperatures of the warm and hot components derived from the 0.45–1.75 keV band plotted against the RGS position angle. (b) C-stat/dof values of the fitting. (c) Relative EM/EM$_{hot}$ ratios for the cool and warm plasmas. (d) Abundance ratios of N/O (vertical ties), Ne/O (ninja-stars), Mg/O (pentagons), and Fe/O (horizontal ties).

reproduce the local band spectra. These gas components mainly contribute to the O VII and O VIII lines, with the new hot component mainly accounting for the Fe-L and Mg lines. In this model, $kT_{\rm hot}$, $kT_{\rm warm}$ and EMs of each component are varied freely, under the assumption that $kT_{\rm warmN} = kT_{\rm warmS}$. We fix $kT_{\rm cool}$ to 0.14 keV. The N, O, Ne, Mg, Fe, and Ni abundances are free parameters with shared values across all spectral components. At the same time, other metals are set to 1 solar. The intrinsic absorption for the hot plasma in M82, which is more substantial than for the warm and cool gases (see Sect. 5.4.1), is difficult to constrain. Hence, we adopt 8×10^{21} cm^{-2} for the hot component extinction, consistent with the intrinsic absorption estimated for the hot gases by the CCD study ($kT \gtrsim 0.7$ keV, Lopez et al. 2020). Even when allowed to vary, the mean value of the hot gas absorption is close to this fixed value. Other prescriptions for the warm and cool components follow the ones with each shifted-CIEs modelling (Sects. 5.4.3 and 5.4.4).

The best-fitting models for the representative broadband spectra of M82 are shown in Fig. 35. As we designed, each CIE component contributes to observed emission lines. This model yields good fits with excellent C-stat/dof values up to 1.1 for all observations (Fig. 36(a)). In Fig. 36(b), we plot the derived $kT_{\rm hot}$ and $kT_{\rm warm}$ against the position angles. We obtain the medians and 16–84th percentile ranges as $kT_{\rm hot} = 0.70\,(0.68–0.74)$ keV and $kT_{\rm warm} = 0.41\,(0.40–0.43)$ keV. The inclusion of the hot gas in the Fe-L lines results in a slight decrease in the $kT_{\rm warm}$ value compared to the results from the shifted-CIEs method for the local O VIII band. Figure 36(c) reveals uniform values for the relative EMs of each temperature plasma. Here, the hot component is more dominant than the other two, with the warm and cool gases in similar intensities. The abundance ratios, N/O, Ne/O, Mg/O, and Fe/O, are also uniform across the dataset: super-solar N/O, solar ratios of Ne/O and Mg/O, and sub-solar Fe/O (Fig.36(d)). In particular, the solar abundance ratios of light α-elements near the disc are the first report, which will be discussed in more detail in Sect. 5.5.3.

5.5 Discussion

5.5.1 Multi-temperature phase in the M82 centre

In our analysis of the RGS spectra from multiple position angles, we determined that the hot (0.7 keV), warm (0.4 keV), and cool (0.1–0.2 keV) components effectively represent the temperature structure of the ISM in M82. The 0.6–0.7 keV component, responsible for Mg (and possibly Si) emission lines, was also reported in studies using

RGS and CCD data Read & Stevens 2002; Origlia et al. 2004; Konami et al. 2011; Zhang et al. 2014; Lopez et al. 2020). A warm plasma component with $kT \sim 0.5$ keV has also been identified by Ranalli et al. (2008). The presence of another cool gas contribution was predicted through line diagnostics of the O VII triplet, suggesting $kT \sim 0.1$–0.3 keV, Ranalli et al. 2008). However, such a cool component at the M82 core has not been reported (e.g., Zhang et al. 2014; Lopez et al. 2020), except for a hint of the 0.2 keV component (Konami et al. 2011, but CCD study). The O VII emission has often been interpreted as a result of the CX processes (e.g., Zhang et al. 2014). However, in our spectral model, which accounts for different spatial broadenings for O VII and O VIII, the CIE components are the primary contributors to these line emissions.

Observational and simulation studies generally predict the core regions of starburst galaxies undergo a multi-temperature phase of gas, ranging from cold dust to hot outflows (e.g., Leroy et al. 2015). Interestingly, such a multiphase state is also applicable to X-ray-emitting gas itself (e.g., Melioli et al. 2013; Schneider et al. 2018). This theoretical prediction is in good agreement with the plasma content that we revealed for M82, as well as with other starburst galaxies (e.g., NGC 3079, Konami et al. 2012; Arp 299, Mao et al. 2021). Furthermore, even in the Milky Way, certain regions with a high concentration of massive stars, such as superbubbles, possess intermixed X-ray plasma with different temperatures (e.g., Kim et al. 2017 for simulation; Fuller et al. 2023 for observation). The multiphase ISM would be ubiquitous in star-forming regions, regardless of their scale. While the origin of different spatial variations of the cool and warm components eludes our present study, we expect it to be examined more robustly through the high-resolution observation of M82.

Needless to say, the aforementioned temperature structure is only an approximation: the three gas components of cool, warm, and hot contribute to the O VII, O VIII+Fe+Ne, and Fe+Mg emission lines (see Fig. 35). The presence of the warm and hot gases has been suggested by previous studies [27] (Ranalli et al. 2008; Konami et al. 2011; Zhang et al. 2014; Lopez et al. 2020). The multi-phase ISM predicted by the simulation study may require additional gas components. Then, what indications from future observations will alert us to the need for additional temperature gas? Restricted to the RGS energy range, it may be worth measuring the distribution of N. If O VII and N show different distributions, this would strongly suggest the

[27] In Jan 2024, Okon et al. (2024) report the similar multi-phase plasma with 0.2, 0.4, 0.9 keV gas components.

presence of even cooler gases that emit the N line. However, due to background emissions, it is more difficult to assess the N distribution than the O one with CCD detectors. Hence, in the future, it will be important to increase the exposure time of M82 using *XMM-Newton*, as well as to perform observations with *XRISM* offering low-background spectra (XRISM Science Team 2020).

5.5.2 Note of CX emission

Previous reports on the CX emission from M82 did focus on the limited position angle (mainly the 319° observation, Liu et al. 2011; Zhang et al. 2014). In this angle, the O VII profile expands toward the low energy scale (Figs. 32(d) and (f)). This expansion is interpreted as high R- or G-ratio values [28] in the energy space. The enhancement in the soft part of the O VII triplet is likely due to the bright outflow towards the southeast, as discussed in Sect. 5.4.4. Although our current results do not strongly favour CX emissions, we consider its contribution in M82 using the 319° result that is, if any, the most significantly contaminated by CX emission. We assume that the CX and CIE components share the same spatial distribution, although a more localized CX emission can be debated (Sect. 5.4.4). From this observation, we obtained an ACX normalization of $3 \pm 1\,\mathrm{cm}^{-5}$. Following the study of M51 by Yang et al. (2020), the ACX normalization can be converted to the spatial scale of the CX reaction as

$$\frac{10^{-10}}{4\pi D^2} \int \frac{n}{\sigma}\,\mathrm{d}A. \tag{2}$$

Here, D, n, and σ are the angular diameter distance to M82, the density of receiver ions in the CX reaction and the CX cross sections, respectively. Assuming a spherical volume with a 40 arcsec (0.7 kpc) radius, we adopted $n = 0.19\,\mathrm{cm}^{-3}$ from the CIE modelling in Sect. 5.4.4. The cross sections were set as $\sigma = 5 \times 10^{-15}\,\mathrm{cm}^2$ (Gu & Shah 2023, and references therein). In consequence, we estimate the CX emitting area $A = 1.4 \times 10^5\,\mathrm{kpc}^2$, which is enormously larger than the assumed surface area $\sim 1.5\,\mathrm{kpc}^2$. This significant discrepancy excites us a suspicion about the brightness of the CX emission if the broadened CX component is a dominant source of the O VII triplet lines. The CX emission properties in M82, such as luminosity or spatial extent, must be under continuous vigilance to be challenged or validated more confidently with the high-resolution and non-dispersive X-ray spectroscopic data coming down from *XRISM* in orbit.

[28] These ratios are given as f/i (R) and $(i + f)/r$ (G), where r, f, and i are the flux of resonance, forbidden, and intercombination lines, respectively

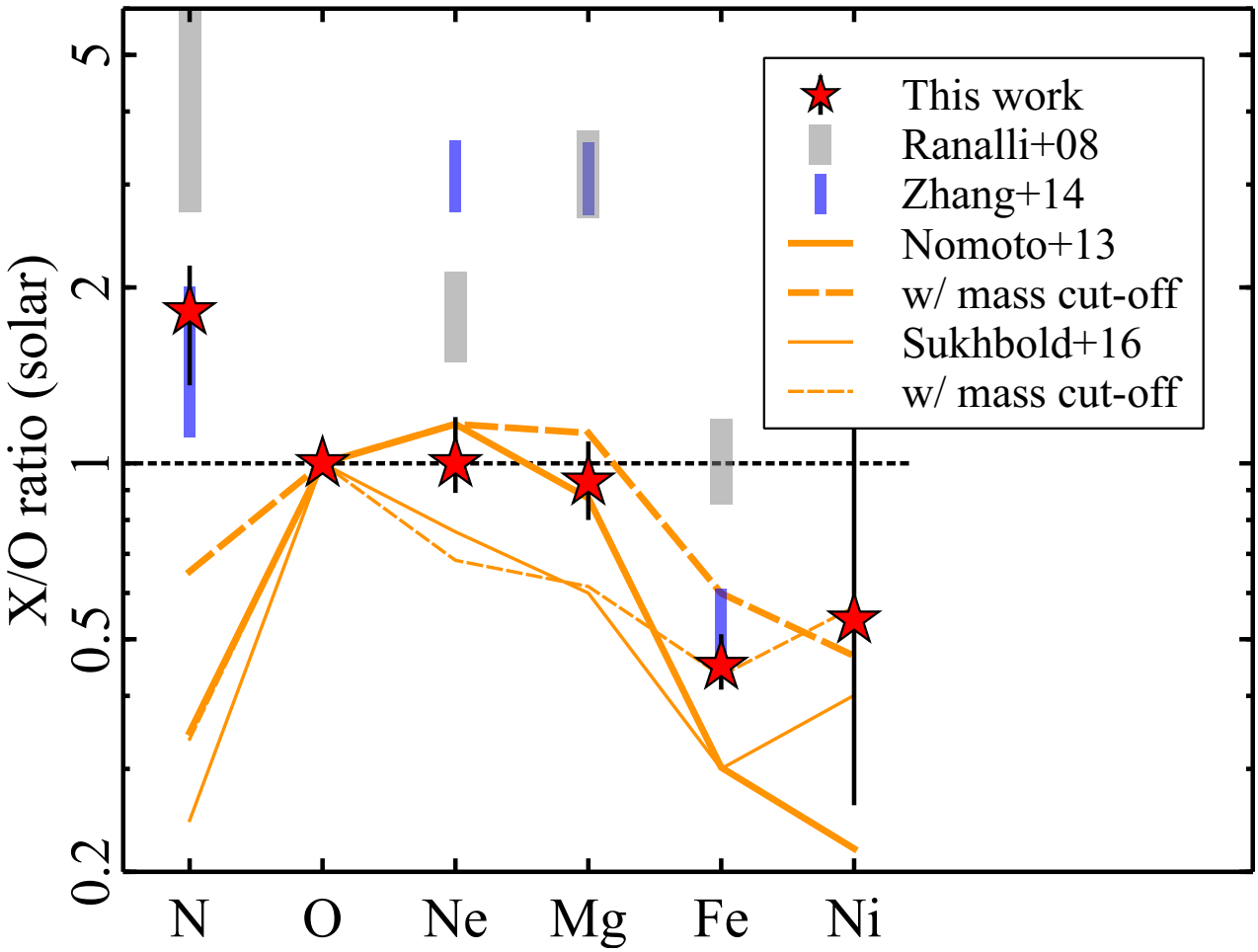

Figure 37: Observed X/O abundance pattern from the broadband spectral fits, where the medians and 16–84th percentile ranges for all dispersion angles are plotted. Two literal values by previous RGS works are given for comparison. The dashed line represents the solar composition. The thick and thin solid lines indicate the IMF-weighted yields predicted by Nomoto et al. (2013) and Sukhbold et al. (2016), respectively, assuming the solar initial metallicity for progenitors. The dashed lines are for each option of the mass-cutoff integration ($< 25\,M_{\odot}$).

5.5.3 Metal abundance pattern

The metal abundance pattern is a key to studying the chemical enrichment process of observed gases. Figure 37 shows the median values and the 16–84th percentile ranges of N/O, Ne/O, Mg/O, Fe/O, and Ni/O across all position angles. We obtained solar-like ratios of the Ne/O and Mg/O that are lower than the results of two earlier RGS works (Ranalli et al. 2008; Zhang et al. 2014). Other studies with CCD reported super-solar patterns of light α-elements (e.g., Konami et al. 2011). The presence or absence of the CX contribution does not change the super-solar abundances in these studies. The primary origin of these gaps is our careful modelling of the O VII and O VIII lines rather than the presence of CX emission, which improves the estimation of a temperature structure in M82. In particular, the inclusion of the cool gas component

would be essential progress in measuring the element abundances.

In Fig 37, we compare the observed abundance pattern in the M82 centre, a starburst system, with nucleosynthesis models of CCSNe. This comparison is crucial as most supernovae in such systems are expected to originate from massive stars. We adopt two models: the "classical" standard yield by Nomoto et al. (2013) and the latest N20 calculations by Sukhbold et al. (2016). For both models, we assume an initial mass function (IMF) by Salpeter (1955) with progenitor masses up to 40 $M_\odot$. In addition, based on the discussion on the missing progenitor mass problem for CCSNe by Smartt (2015), we also employ another IMF-weighted integration with the upper mass limit of 25 $M_\odot$.

For α-elements, the yields with Nomoto et al. (2013) most closely match the observed O, Ne, and Mg pattern but tend to underestimate the Fe/O and Ni/O ratios. For the case with the upper mass limit of 25 $M_\odot$, the half-solar Fe/O and Ni/O values are explained well by both of Nomoto et al. (2013) and Sukhbold et al. (2016). Mao et al. (2021) provide similar consideration in their study of the N/O, Ne/O, Mg/O, S/O, and Ni/O pattern in Arp 299. However, the observed Fe/O and Ni/O ratios in M82 might also be explained by including a minor contribution from Type Ia SNe (only 6 per cent of the total SNe in the M82 core). The hot ISM in M82, as in other starburst galaxies, serves as a significant repository of CCSN products. In any case, the ISM in M82 is a magnificent reservoir of the CCSN products.

Nevertheless, none of these CCSNe models adequately reproduce the N/O ratio ~ 2 solar in M82. Similar high N/O ratios have been reported in more ancient systems, such as early-type galaxies, including the brightest cluster galaxies (e.g., Mao et al. 2019; Fukushima et al. 2023b). These objects owe a dominant fraction of the N enrichment therein to mass-loss winds from massive stellar population or low-mass asymptotic giant branch stars. Thus, it is plausible that such mass-loss channels, aside from CCSNe, contribute to the enrichment observed in the core of M82.

Chapter 6

Concluding Remarks

6.1 Main Results of this Dissertation

Chapter 3 of this dissertation investigated the element distributions in the ICM using deep *Chandra* and *XMM-Newton* observations of the Centaurus cluster. While earlier works had reported an abundance drop in the innermost region, flat profiles were observed towards the centre for noble gas elements like Ne/Fe and Ar/Fe. The results suggested that the abundance drop is partly caused by systematic uncertainties in atomic codes or response matrices rather than the metal depletion process as was claimed. The measured abundance pattern of the Si/Fe, S/Fe, Ar/Fe, Ca/Fe, Cr/Fe, and Mn/Fe ratios was close to solar values. For lighter elements, the O/Fe, Ne/Fe, and Mg/Fe ratios were lower, and the N/Fe ratio was higher than the solar composition. Despite the latest versions of the atomic codes, the Ni/Fe ratio was significantly higher than the solar ratio. Linear combination models of recent SN yield calculations suggested contributions from both near- and sub-Chandrasekhar mass SNe Ia are required to explain certain ratios. The low Ne/Fe, Mg/Fe, and high Ni/Fe ratios are not satisfactorily reproduced by these models. The N/O ratio in the cool core is consistent with the expected values in winds from AGB stars. The ICM mass around NGC 4696, assuming a star formation at redshift $z = 2$–3, can be reproduced by stellar mass loss over the look-back 9–10 Gyr. Our study emphasizes the importance of high-resolution spectroscopy for measuring metal abundances and calls for future missions to refine our understanding of chemical enrichment in galaxy clusters.

In Chapter 4, we analysed the RGS data of 14 nearby early-type galaxies, including BCGs. The focus was on measuring radial metal distribution, abundance patterns, and gas mass. We revealed generally flat radial profiles of the O/Fe, Ne/Fe, and Mg/Fe ratios at the centre of each object, challenging the dust depletion scenario. System-

atic differences up to 10–40 per cent were observed in atomic codes, for determining $\langle kT \rangle$, absolute abundances, and relative abundance ratios, respectively. These differences are independent of the gas temperatures of each object. Abundances and ratios correlate more strongly with $\langle kT \rangle$ than with $M_{<60''}/L_B$. The N/O ratios are systematically higher than the solar value, suggesting ongoing enrichment from mass-loss winds of 3–5 solar-mass stars. Abundance patterns of hot or high-$M_{<60''}/L_B$ systems align with solar composition, while cool and low-$M_{<60''}/L_B$ objects exhibit potentially overestimated super-solar Ni/Fe ratios. The study anticipates advancements with non-dispersive and high-resolution spectroscopic missions such as *XRISM* and *Athena*, offering unique methods for measuring metal abundances in subkiloelectronvolt plasma. These missions are expected to provide invaluable information about supernova contributions to the enrichment of early-type galaxies, particularly in determining the Ne and Ni abundances with unprecedented accuracy.

The study in Chapter 5 focused on the X-ray emission from the M82 core, using the RGS to estimate metal abundances in the ISM accurately. Over 300 kiloseconds of RGS data from 14 position angles were analysed, covering a 80 arcsecond cross-dispersion width. Multi-phase thermal plasma modelling with the three CIEs was adopted to reproduce the spectra, revealing spatial variations, particularly in the O VII band CCD image, which has a broader distribution than those in the O VIII and Fe-L bands. The O VIII line profiles showed a remarkably double-peaked structure, corresponding to the north and south outflows. Although a combination of the CIE and CX emission models successfully reproduced the O VII line profiles, uneven component ratios with the RGS dispersion angles suggest an implausible presence of the CX emission. Broadband spectral fitting suggested a multi-temperature phase of the ISM with components at 0.1, 0.4 and 0.7 keV. The derived abundance pattern shows the super-solar N/O, solar Ne/O and Mg/O, and half-solar Fe/O ratios, indicating chemical enrichment from CCSNe in starburst galaxies. The study highlights the importance of accurate temperature structure estimation and encourages continued efforts in high-resolution X-ray spectroscopy, especially with the upcoming *XRISM* observation.

6.2 Summary Discussion

The results of Chapters 3 and 4 reveal that the spatial distribution of noble gas Ne in many early-type galaxies, including some BCGs, is consistent with that of the normal metals, regardless of the presence of Fe drop. Thus, the cold dust scenario

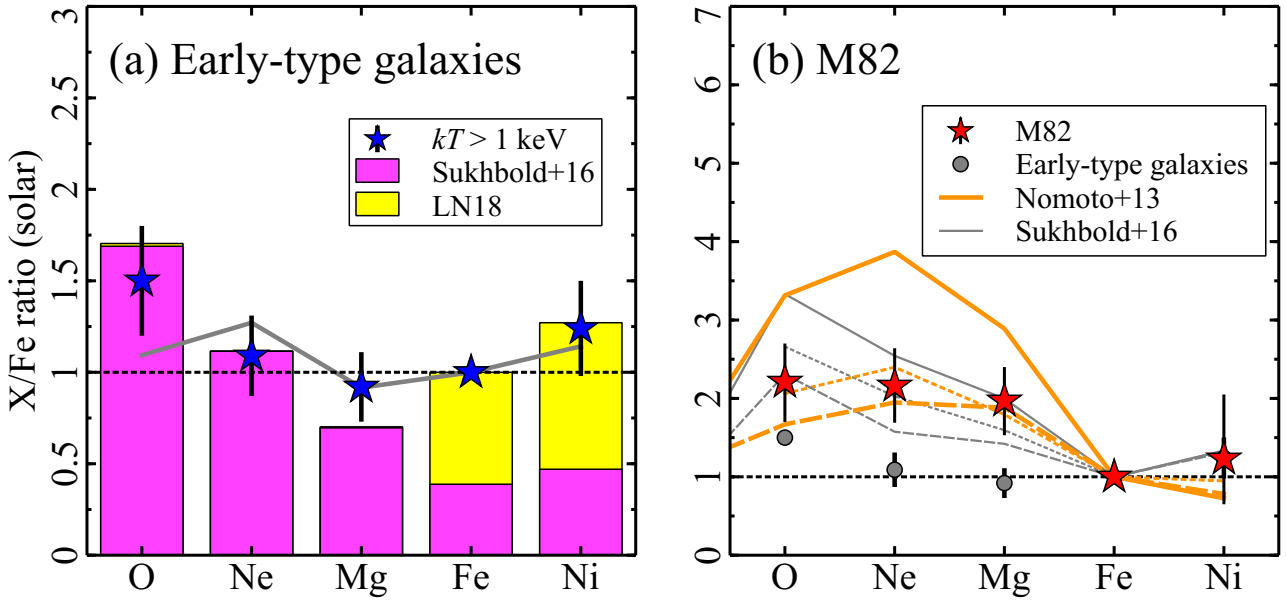

Figure 38: Obtained X/Fe abundance patterns from this work for (a) early-type galaxies with $kT > 1$ keV and (b) a starburst system M82 galaxy. Systematics of 20 per cent are added in quadrature to each statistic error. (a) Stars indicate the observed ratios in early-type galaxies ($kT > 1$ keV). The best-fitting combination model is shown with SN Ia model of Leung & Nomoto (2018) and CCSN yield of Sukhbold et al. (2016), both of which are the latest calculations. The grey line shows a combination of Leung & Nomoto (2018) and Nomoto et al. (2013). (b) Stars show the results of M82 and circles are for the same data in (a). Each CCSN yield calculation is taken from classical Nomoto et al. (2013) and the latest Sukhbold et al. (2016), assuming solar metallicity progenitors. The integrated function of progenitor mass is the Salpeter IMF (Salpeter 1955). The dashed lines are for each option of the mass-cutoff integration ($< 25\,M_\odot$). The dotted lines show a combination model with SN Ia yield of Leung & Nomoto (2018).

(e.g., Panagoulia et al. 2013, 2015) and the cooling-flow model (e.g., Fabian 1994; Fabian et al. 2022, 2023a,b), as the main back supporter thereof (see Chapter 2), are challenged. The abundance drops, *if any*, may originate from the feedback of active galactic nuclei which would remove a fraction of central metal-rich gas directly and dissipate it towards the outer radius (e.g., Sanders et al. 2016; Liu et al. 2019). The abundance ratios of M82 obtained in Chapter 5 also do not deviate from nucleosynthesis models as greatly as in other studies (e.g., Ranalli et al. 2008; Zhang et al. 2014; Okon et al. 2024). There seems to be no evidence for positively accepting the effect of cold dust, also discussed and doubted in Okon et al. (2024), where their abundances require dust grains to affect differently not only between normal and noble gas elements but also among normal metals [29]. In other words, the abundance ratios measured in the ICM or ISM in the central regions of early-type and starburst galaxies do not change significantly from those expected for SN enrichment,

[29]When the dust effect is significant, the Ne/O ratio increases and the Mg/O and Fe/O will not change drastically from the SN yield. Unfortunately, other works derive the mysterious pattern with high Ne/O and Mg/O, and solar Fe/O ratios.

excluding possible observational biases and systematic errors discussed especially in Chapter 4. Now, test the supernova synthetic models using reliable O/Fe, Ne/Fe, Mg/Fe and Ni/Fe abundance ratios that would not be biased by cold dust effects. Figure 38 shows that the observed abundance patterns of early-type galaxies and M82 are compared to SN nucleosynthesis models, where the result of early-type galaxies is limited to the hot samples free from the Ne and Mg problem (see Chapter 4). The N results are also excluded as does it not originate primarily from SNe (see Chapters 2, 3, 4, 5).

In Fig. 38(a), the abundance pattern of early-type galaxies is quite close to the solar composition and reproduced by both CCSN and SN Ia contributions. As seen in Chapters 3 and 4, the latest SN Ia yield is clearly better at estimating Ni [30]; thus, the calculation of Leung & Nomoto (2018) with a near-$M_{\rm Ch}$ progenitor is adopted. If RGS could measure the Cr and Mn abundances as can CCD, a sub-$M_{\rm Ch}$ progenitor model would be required (Hitomi Collaboration et al. 2017; Simionescu et al. 2019; Fukushima et al. 2022). For the CCSN contribution, we try both predictions by Nomoto et al. (2013) and Sukhbold et al. (2016). The combination of Leung & Nomoto (2018) and the latest Sukhbold et al. (2016) with the number ratio SN Ia/(SN Ia+CCSN) ~ 11 per cent gives the best-fitting results, yielding the SN Ia contribution to Fe ~ 60 per cent (see histogram in Fig. 38(a)). On the other hand, the combination of Leung & Nomoto (2018) and the classical Nomoto et al. (2013) also reproduces the observed pattern, fitting O worse and Mg better. This combination provides SN Ia/(SN Ia+CCSN) ~ 18 per cent and 72 per cent of Fe is from SNe Ia. Given that systematic errors of abundance estimate are 20 per cent, the χ^2/dof values are 0.6 and 0.9 for the choices of Sukhbold et al. (2016) and Nomoto et al. (2013), respectively. Both combination models seem to reproduce the observed abundances reasonably well. The differences in estimation of the breakdown of SN types and the SN Ia contribution to iron are at most 10 per cent. Hence, these models are somewhat plausible, especially the SN Ia model (Leung & Nomoto 2018).

Next, look at the abundance pattern of the ISM in a starburst galaxy M82, where the enrichment source *must be* heavily relies on CCSNe. Comparing the star- and circle-shaped plots, it is clear that the chemical composition of M82 is evidently in excess of light α-elements relative to Fe. The CCSN contribution *is actually* stronger

[30]The combination model with classical SN Ia calculations (e.g., Iwamoto et al. 1999) over-predicts the Ni/Fe ratio seriously by a factor of two (see Fig. 2). Models that cannot reproduce solar composition in any way are at least inappropriate as the dominant enrichment channel. This is because such SNe cannot create our solar system, we are *here now*; in that case, we would be *nowhere*.

in M82 than in early-type galaxies. Note that predicted yields by the classical and latest CCSN models are larger than the observed abundances. The classical model is larger for all O/Fe, Ne/Fe and Mg/Fe, and the latest one overestimates only O/Fe. There are two possible ways to fill in this schism. The first is to include the SN Ia (Leung & Nomoto 2018) contribution, as it is unlikely that SNe Ia are never present at all in starburst galaxies. The combination model (see dotted lines in Fig. 38(b)) results in SN Ia/(SN Ia+CCSN) ~ 6 per cent with Nomoto et al. (2013) and ~ 2 per for the choice of Sukhbold et al. (2016). The χ^2/dof values are 0.2 and 0.5 with the classical and latest models, respectively. In both cases, the SN Ia contribution in M82 is smaller than in early-type galaxies, and the dominant enrichment source in M82 is the CCSN as > 94 per cent. Another approach is to assume pure enrichment by CCSNe by imposing an upper limit on their progenitor mass. When considering the chemical enrichment of ancient systems such as early-type galaxies and cluster cores, the metal yields of CCSNe are calculated, assuming that even extremely massive stars undergo CCSNe. Theoretically, whether such massive stars actually undergo CCSN has yet to be settled. In observational studies, Smartt (2015) do not favour massive progenitors, as well as the progenitor mass predicted from observations of CCSN remnants rarely exceeds $30\,M_\odot$ [31]. It is also difficult to accept that the ongoing star formation in M82 generates many such massive stars; thus, the element yields are calculated assuming that stars above $25\,M_\odot$ do not contribute as CCSN (see the dashed lines in Fig. 38(b)). The result is obvious as Nomoto et al. (2013) underestimates O/Fe, and Sukhbold et al. (2016) undervalues Ne/Fe and Mg/Fe, [32] yielding the goodness of fit are 0.6 and 1, respectively. These results show that models including SN Ia give a better fit than those with an upper limit on progenitor masses. Nevertheless, all model configurations reproduce the observed abundance pattern well. Moreover, if the results in CCSN-dominated system M82 are more reliable than in early-type galaxies, the classical Nomoto et al. (2013) model may also prefer the more recent Sukhbold et al. (2016).

Last but not least, the element abundance ratios of the BCGs are consistent with the solar chemical composition, except for Ni/Fe in the Centaurus cluster. The combination model of the latest SN Ia and CCSN models reproduce this abundance pattern well. In these early-type galaxies, the stars capable of forming SNe, including

[31] As far as known, the only exception is a CCSN remnant CTB 109, expected a large progenitor mass as 30–40 $M_\odot$ (Nakano et al. 2017).

[32] The O, Ne, and Mg yield estimates of CCSN models are dependent strongly on the $^{12}C \rightarrow {}^{16}O$ reaction rate that remains a 20 per cent uncertainty (deBoer et al. 2017).

long-lived stars, may have completed their explosions. In this case, it is not correct to say that the abundance pattern of our Milky Way is typical and special in the universe, as if *God-given*; and instead, systems that have finished the bulk of SNe from populations born during star formation will inevitably get to the solar composition. In contrast, the O/Fe, Ne/Fe, and Mg/Fe abundances of M82 are about twice the solar abundances, suggesting the contribution of CCSN to the M82 enrichment. This picture is very different from our Milky Way galaxy, where enough time has passed since the active star formation. In the future, we may be able to observe the solar abundance pattern in M82 after the starburst has subsided and, thenceforth, a few hundred million years later. By that time though, our Milky Way will merge with the neighbour M31 galaxy, causing the next starburst in our beautiful home and forming the stardust as the remnant of us.

6.3 Conclusions

In this work, the abundance patterns are obtained from the hot ISM or ICM in early-type galaxies, groups, and clusters that have been confining metals for several Gyr and from the ISM enriched by enhanced star formation and frequent CCSN in a starburst galaxy M82 which are compared with SN nucleosynthesis models. The discussion above and the main conclusion of this work are summarized as follows.

– There seems to be no need to be concerned about abundance anomalies due to cold dust, as has been previously proposed. In particular, the abundance drops due to element depletion into cold dust grains (supported by the cooling-flow model), which has been predicted in the cluster centres, are questioned. This result is obtained by the robust Ne estimate with the RGS spectroscopy.

– Except high Ne, Mg, and Ni in the objects with low plasma temperatures and high Ni in the Centaurus cluster, the abundance ratios, free from the dust grains, observed in the ISM or ICM of early-type galaxies are surprisingly consistent with the solar composition, i.e. the abundance in our Milky Way. On the other hand, the abundance pattern with enhanced α/Fe in M82, which is classified as a spiral galaxy like our Milky Way, indicates that the CCSN strongly contaminated this system compared to our home. Of course, the latter result is to be expected since M82 is a starburst galaxy, as is known, and there must be numerous CCSNe. It is worth noting that unnatural values for Ne/O, Mg/O, and Fe/O are improved

significantly compared to previous studies by the method that accurately takes into account the spatial distribution of each plasma component.

– Current synthetic models by SNe are plausible enough to reproduce roughly the solar O/Fe, Ne/Fe, Mg/Fe, and Ni/Fe abundance ratios (with 20 per cent systematics), even with different selections of CCSN models. Both models of SN Ia and CCSN can also determine the fraction of each SN type contributing to chemical enrichment by about 10 per cent. In the Centaurus cluster, the Cr/Fe and Mn/Fe ratios are also measured by CCD, suggesting that both near- and sub-$M_{\rm Ch}$ SNe Ia are required. This is the second example following the results from the Perseus cluster.

– In particular for CCSNe, there is a hint that extremely massive stars do not result in SN explosion as some theorists and observers have claimed if the M82 galaxy is a pure CCSN-enriched system. It is also possible that only a small fraction of SN Ia is contributing to the ISM. In both cases, the CCSN model with classical calculations is preferable to reproduce the observed abundance pattern.

– The solar chemical composition, i.e. the abundance pattern of our Milky Way, must not be *special* to this universe. The solar composition is just the element abundance that is ubiquitously exhibited by systems that evolve over a long time in this universe.

Is the conclusion of this dissertation a copestone? No, it must be one of the new cornerstones. A new era of X-ray astronomy has just dawned with the *XRISM* launch.

Bibliography

Abbott B. P., et al., 2017, ApJL, 848, L12

Akahori T., et al., 2020, PASJ, 72, 62

Allen S. W., Fabian A. C., 1994, MNRAS, 269, 409

Alpher R. A., Bethe H., Gamow G., 1948, Physical Review, 73, 803

Arimoto N., Matsushita K., Ishimaru Y., Ohashi T., Renzini A., 1997, ApJ, 477, 128

Arnaud K. A., 1996, in Jacoby G. H., Barnes J., eds, Astronomical Society of the Pacific Conference Series Vol. 101, Astronomical Data Analysis Software and Systems V. p. 17

Arnett W. D., Bahcall J. N., Kirshner R. P., Woosley S. E., 1989, ARA&A, 27, 629

Barré H., Nye H., Janin G., 1999, ESA Bulletin, 100, 15

Bethe H. A., 1939, Physical Review, 55, 434

Biffi V., Mernier F., Medvedev P., 2018, SSRv, 214, 123

Blondin S., Bravo E., Timmes F. X., Dessart L., Hillier D. J., 2022, A&A, 660, A96

Böhringer H., Werner N., 2010, A&A Rv, 18, 127

Böhringer H., Matsushita K., Churazov E., Finoguenov A., Ikebe Y., 2004, A&A, 416, L21

Brandt W. N., Hasinger G., 2005, ARA&A, 43, 827

Brickhouse N. S., Dupree A. K., Edgar R. J., Liedahl D. A., Drake S. A., White N. E., Singh K. P., 2000, ApJ, 530, 387

Brightman M., et al., 2016, ApJ, 829, 28

Bryans P., Landi E., Savin D. W., 2009, ApJ, 691, 1540

Buote D. A., Canizares C. R., 1997, ApJ, 474, 650

Burbidge E. M., Burbidge G. R., Fowler W. A., Hoyle F., 1957, Reviews of Modern Physics, 29, 547

Burrows A., Vartanyan D., 2021, Nature, 589, 29

Campbell S. W., Lattanzio J. C., 2008, A&A, 490, 769

Carollo C. M., Danziger I. J., Buson L., 1993, MNRAS, 265, 553

Cash W., 1979, ApJ, 228, 939

Chen Y., Reiprich T. H., Böhringer H., Ikebe Y., Zhang Y. Y., 2007, A&A, 466, 805

Chen Y., Wang Q. D., Zhang G.-Y., Zhang S., Ji L., 2018, ApJ, 861, 138

Chornock R., et al., 2017, ApJL, 848, L19

Churazov E., Forman W., Jones C., Böhringer H., 2003, ApJ, 590, 225

Ciotti L., D'Ercole A., Pellegrini S., Renzini A., 1991, ApJ, 376, 380

Conselice C. J., Wilkinson A., Duncan K., Mortlock A., 2016, ApJ, 830, 83

Courteau S., et al., 2014, Reviews of Modern Physics, 86, 47

Cravens T. E., 2002, Science, 296, 1042

Crawford C. S., Hatch N. A., Fabian A. C., Sanders J. S., 2005, MNRAS, 363, 216

Cumbee R. S., Liu L., Lyons D., Schultz D. R., Stancil P. C., Wang J. G., Ali R., 2016, MNRAS, 458, 3554

De Grandi S., Molendi S., 2001, ApJ, 551, 153

Doherty C. L., Gil-Pons P., Siess L., Lattanzio J. C., Lau H. H. B., 2015, MNRAS, 446, 2599

Dupke R. A., White Raymond E. I., 2000, ApJ, 528, 139

Engelbracht C. W., et al., 2006, ApJL, 642, L127

Erdim M. K., Ezer C., Ünver O., Hazar F., Hudaverdi M., 2021, MNRAS, 508, 3337

Ettori S., 2002, MNRAS, 330, 971

Ezer C., Bulbul E., Nihal Ercan E., Smith R. K., Bautz M. W., Loewenstein M., McDonald M., Miller E. D., 2017, ApJ, 836, 110

Ezoe Y., Hamaguchi K., Fukushima A., Ogawa T., Ohashi T., 2019, PASJ, 71, 122

Fabian A. C., 1994, ARA&A, 32, 277

Fabian A. C., Ferland G. J., Sanders J. S., McNamara B. R., Pinto C., Walker S. A., 2022, MNRAS, 515, 3336

Fabian A. C., Sanders J. S., Ferland G. J., McNamara B. R., Pinto C., Walker S. A., 2023a, MNRAS, 521, 1794

Fabian A. C., Sanders J. S., Ferland G. J., McNamara B. R., Pinto C., Walker S. A., 2023b, MNRAS, 524, 716

Feltzing S., Gustafsson B., 1998, A&AS, 129, 237

Foster A. R., Ji L., Smith R. K., Brickhouse N. S., 2012, ApJ, 756, 128

Fruscione A., et al., 2006, in Proc. SPIE. p. 62701V, doi:10.1117/12.671760

Fukazawa Y., Ohashi T., Fabian A. C., Canizares C. R., Ikebe Y., Makishima K., Mushotzky R. F., Yamashita K., 1994, PASJ, 46, L55

Fukushima K., Kobayashi S. B., Matsushita K., 2022, MNRAS, 514, 4222

Fukushima K., Nagamine K., Shimizu I., 2023a, MNRAS, 525, 3760

Fukushima K., Kobayashi S. B., Matsushita K., 2023b, ApJ, 953, 112

Fuller C. A., Kaaret P., Bluem J., Kuntz K. D., Hodges-Kluck E., Jahoda K. M., 2023, ApJ, 943, 61

Gastaldello F., Simionescu A., Mernier F., Biffi V., Gaspari M., Sato K., Matsushita K., 2021, Universe, 7, 208

Gatuzz E., et al., 2022, MNRAS, 513, 1932

Gatuzz E., et al., 2023, MNRAS, 520, 4793

Gratton R. G., Carretta E., Claudi R., Lucatello S., Barbieri M., 2003, A&A, 404, 187

Gu L., Shah C., 2023, Charge exchange in X-ray astrophysics. Springer Nature Singapore, pp 255–289, doi:10.1007/978-981-99-4409-5_10

Gu L., et al., 2019, A&A, 627, A51

Gu L., et al., 2020, A&A, 641, A93

Gu L., et al., 2022, A&A, 664, A62

Heringer E., Pritchet C., van Kerkwijk M. H., 2019, ApJ, 882, 52

Hitomi Collaboration et al., 2017, Nature, 551, 478

Hitomi Collaboration et al., 2018a, PASJ, 70, 11

Hitomi Collaboration et al., 2018b, PASJ, 70, 12

Höfner S., Olofsson H., 2018, A&A Rv, 26, 1

Hopkins P. F., et al., 2023, MNRAS, 519, 3154

Hoyle F., 1946, MNRAS, 106, 343

Hyodo Y., Tsujimoto M., Hamaguchi K., Koyama K., Kitamoto S., Maeda Y., Tsuboi Y., Ezoe Y., 2008, PASJ, 60, S85

Ikebe Y., Böhringer H., Kitayama T., 2004, ApJ, 611, 175

Iwamoto K., Brachwitz F., Nomoto K., Kishimoto N., Umeda H., Hix W. R., Thielemann F.-K., 1999, ApJS, 125, 439

Jansen F., et al., 2001, A&A, 365, L1

Johnson J. A., 2019, Science, 363, 474

Johnstone R. M., Allen S. W., Fabian A. C., Sanders J. S., 2002, MNRAS, 336, 299

Kaastra J. S., 2017, A&A, 605, A51

Kaastra J. S., Mewe R., Nieuwenhuijzen H., 1996, in UV and X-ray Spectroscopy of Astrophysical and Laboratory Plasmas. pp 411–414

Käppeler F., Gallino R., Bisterzo S., Aoki W., 2011, Reviews of Modern Physics, 83, 157

Karachentsev I. D., Karachentseva V. E., Huchtmeier W. K., Makarov D. I., 2004, AJ, 127, 2031

Karakas A. I., 2010, MNRAS, 403, 1413

Karakas A. I., Lattanzio J. C., 2014, PASA, 31, e030

Katsuda S., et al., 2015, ApJ, 808, 49

Kim C.-G., Ostriker E. C., Raileanu R., 2017, ApJ, 834, 25

Kirkpatrick C. C., McNamara B. R., 2015, MNRAS, 452, 4361

Kobayashi C., Arimoto N., 1999, ApJ, 527, 573

Kobayashi C., Nomoto K., 2009, ApJ, 707, 1466

Kobayashi C., Karakas A. I., Lugaro M., 2020, ApJ, 900, 179

Konami S., Matsushita K., Tsuru T. G., Gandhi P., Tamagawa T., 2011, PASJ, 63, S913

Konami S., Matsushita K., Gandhi P., Tamagawa T., 2012, PASJ, 64, 117

Konami S., Matsushita K., Nagino R., Tamagawa T., 2014, ApJ, 783, 8

Kuntschner H., et al., 2010, MNRAS, 408, 97

Lakhchaura K., Mernier F., Werner N., 2019, A&A, 623, A17

Leccardi A., Molendi S., 2008, A&A, 486, 359

Lehnert M. D., Heckman T. M., Weaver K. A., 1999, ApJ, 523, 575

Leroy A. K., et al., 2015, ApJ, 814, 83

Lester D. F., Carr J. S., Joy M., Gaffney N., 1990, ApJ, 352, 544

Leung S.-C., Nomoto K., 2018, ApJ, 861, 143

Li W., et al., 2011, MNRAS, 412, 1441

Licquia T. C., Newman J. A., 2015, ApJ, 806, 96

Liu J., Mao S., Wang Q. D., 2011, MNRAS, 415, L64

Liu J., Wang Q. D., Mao S., 2012, MNRAS, 420, 3389

Liu A., Zhai M., Tozzi P., 2019, MNRAS, 485, 1651

Lodders K., Palme H., Gail H. P., 2009, Abundances of the Elements in the Solar System. Springer Berlin, Heidelberg, pp 560–598 (arXiv:0901.1149), doi:10.1007/978-3-540-88055-4_34

Lopez L. A., Mathur S., Nguyen D. D., Thompson T. A., Olivier G. M., 2020, ApJ, 904, 152

Mac Low M.-M., McCray R., Norman M. L., 1989, ApJ, 337, 141

Madau P., Ferguson H. C., Dickinson M. E., Giavalisco M., Steidel C. C., Fruchter A., 1996, MNRAS, 283, 1388

Makarov D., Prugniel P., Terekhova N., Courtois H., Vauglin I., 2014, A&A, 570, A13

Mao J., et al., 2019, A&A, 621, A9

Mao J., et al., 2021, ApJL, 918, L17

Mao J., Paerels F., Guainazzi M., Kaastra J. S., 2023, XMM-Newton Reflection Grating Spectrometer. Springer Nature Singapore, pp 9–45, doi:10.1007/978-981-99-4409-5_2

Matsushita K., 2001, ApJ, 547, 693

Matsushita K., 2011, A&A, 527, A134

Matsushita K., Makishima K., Rokutanda E., Yamasaki N. Y., Ohashi T., 1997, ApJL, 488, L125

Matsushita K., Ohashi T., Makishima K., 2000, PASJ, 52, 685

Matsushita K., Finoguenov A., Böhringer H., 2003, A&A, 401, 443

Matsushita K., Böhringer H., Takahashi I., Ikebe Y., 2007, A&A, 462, 953

Matsushita K., Sato T., Sakuma E., Sato K., 2013a, PASJ, 65, 10

Matsushita K., Sakuma E., Sasaki T., Sato K., Simionescu A., 2013b, ApJ, 764, 147

Mayya Y. D., Carrasco L., Luna A., 2005, ApJL, 628, L33

McGuire B. A., 2022, ApJS, 259, 30

McNamara B. R., Nulsen P. E. J., 2012, New Journal of Physics, 14, 055023

Melioli C., de Gouveia Dal Pino E. M., Geraissate F. G., 2013, MNRAS, 430, 3235

Mernier F., de Plaa J., Lovisari L., Pinto C., Zhang Y. Y., Kaastra J. S., Werner N., Simionescu A., 2015, A&A, 575, A37

Mernier F., et al., 2016, A&A, 595, A126

Mernier F., et al., 2017, A&A, 603, A80

Mernier F., et al., 2018a, SSRv, 214, 129

Mernier F., et al., 2018b, MNRAS, 478, L116

Mernier F., et al., 2018c, MNRAS, 480, L95

Mernier F., et al., 2020, Astronomische Nachrichten, 341, 203

Mernier F., et al., 2022, MNRAS, 511, 3159

Million E. T., Werner N., Simionescu A., Allen S. W., 2011, MNRAS, 418, 2744

Mishra W., Srivastava N., Wang Y., Mirtoshev Z., Zhang J., Liu R., 2019, MNRAS, 486, 4671

Mitchell R. J., Culhane J. L., Davison P. J. N., Ives J. C., 1976, MNRAS, 175, 29P

Mitsuda K., et al., 2007, PASJ, 59, S1

Mitsuishi I., Yamasaki N. Y., Takei Y., 2013, PASJ, 65, 44

Mittal R., et al., 2011, MNRAS, 418, 2386

Mittal R., Whelan J. T., Combes F., 2015, MNRAS, 450, 2564

Nagino R., Matsushita K., 2009, A&A, 501, 157

Nakano T., Murakami H., Furuta Y., Enoto T., Masuyama M., Shigeyama T., Makishima K., 2017, PASJ, 69, 40

Nakashima S., Inoue Y., Yamasaki N., Sofue Y., Kataoka J., Sakai K., 2018, ApJ, 862, 34

Nandra K., et al., 2013, arXiv e-prints, p. arXiv:1306.2307

Narita T., Uchida H., Yoshida T., Tanaka T., Tsuru T. G., 2023, ApJ, 950, 137

Nomoto K., Tominaga N., Umeda H., Kobayashi C., Maeda K., 2006, NuPhA, 777, 424

Nomoto K., Kobayashi C., Tominaga N., 2013, ARA&A, 51, 457

Ogorzalek A., et al., 2017, MNRAS, 472, 1659

Ohshiro Y., et al., 2021, ApJL, 913, L34

Okon H., Smith R. K., picquenot A., Foster A. R., 2024, arXiv e-prints, p. arXiv:2401.02276

Origlia L., Ranalli P., Comastri A., Maiolino R., 2004, ApJ, 606, 862

Orlitova I., 2020, Starburst galaxies. Springer Cham, pp 379–411, doi:10.1007/978-3-030-38509-5

Orr M. E., Fielding D. B., Hayward C. C., Burkhart B., 2022, ApJ, 932, 88

Panagoulia E. K., Fabian A. C., Sanders J. S., 2013, MNRAS, 433, 3290

Panagoulia E. K., Sanders J. S., Fabian A. C., 2015, MNRAS, 447, 417

Prantzos N., Abia C., Limongi M., Chieffi A., Cristallo S., 2018, MNRAS, 476, 3432

Ranalli P., Comastri A., Origlia L., Maiolino R., 2008, MNRAS, 386, 1464

Read A. M., Stevens I. R., 2002, MNRAS, 335, L36

Reddy B. E., Lambert D. L., Allende Prieto C., 2006, MNRAS, 367, 1329

Russell H. R., Sanders J. S., Fabian A. C., 2008, MNRAS, 390, 1207

Sakuma E., Ota N., Sato K., Sato T., Matsushita K., 2011, PASJ, 63, S979

Salpeter E. E., 1955, ApJ, 121, 161

Sanders J. S., Fabian A. C., 2002, MNRAS, 331, 273

Sanders J. S., Fabian A. C., Allen S. W., Morris R. G., Graham J., Johnstone R. M., 2008, MNRAS, 385, 1186

Sanders J. S., et al., 2016, MNRAS, 457, 82

Sarazin C. L., 1988, X-ray emission from clusters of galaxies

Sarkar A., Su Y., Truong N., Randall S., Mernier F., Gastaldello F., Biffi V., Kraft R., 2022, MNRAS, 516, 3068

Sato K., Tokoi K., Matsushita K., Ishisaki Y., Yamasaki N. Y., Ishida M., Ohashi T., 2007, ApJL, 667, L41

Schneider E. E., Robertson B. E., Thompson T. A., 2018, ApJ, 862, 56

Seitenzahl I. R., et al., 2013a, MNRAS, 429, 1156

Seitenzahl I. R., Cescutti G., Röpke F. K., Ruiter A. J., Pakmor R., 2013b, A&A, 559, L5

Serlemitsos P. J., Smith B. W., Boldt E. A., Holt S. S., Swank J. H., 1977, ApJL, 211, L63

Shapiro S. L., Teukolsky S. A., 1983, White Dwarfs. John Wiley & Sons, Ltd, pp 55–81, doi:10.1002/9783527617661

Shen K. J., Kasen D., Miles B. J., Townsley D. M., 2018, ApJ, 854, 52

Simionescu A., Werner N., Finoguenov A., Böhringer H., Brüggen M., 2008, A&A, 482, 97

Simionescu A., Werner N., Böhringer H., Kaastra J. S., Finoguenov A., Brüggen M., Nulsen P. E. J., 2009, A&A, 493, 409

Simionescu A., Werner N., Urban O., Allen S. W., Ichinohe Y., Zhuravleva I., 2015, ApJL, 811, L25

Simionescu A., et al., 2019, MNRAS, 483, 1701

Smartt S. J., 2015, PASA, 32, e016

Smith R. K., Brickhouse N. S., Liedahl D. A., Raymond J. C., 2001, ApJL, 556, L91

Smith R. K., Foster A. R., Edgar R. J., Brickhouse N. S., 2014, ApJ, 787, 77

Snowden S. L., Mushotzky R. F., Kuntz K. D., Davis D. S., 2008, A&A, 478, 615

Strickland D. K., Heckman T. M., 2007, ApJ, 658, 258

Strickland D. K., Heckman T. M., 2009, ApJ, 697, 2030

Strickland D. K., Ponman T. J., Stevens I. R., 1997, A&A, 320, 378

Strickland D. K., Heckman T. M., Colbert E. J. M., Hoopes C. G., Weaver K. A., 2004, ApJS, 151, 193

Struble M. F., Rood H. J., 1999, ApJS, 125, 35

Strüder L., et al., 2001, A&A, 365, L18

Sugiyama H., Ueda M., Fukushima K., Kobayashi S. B., Yamasaki N. Y., Sato K., Matsushita K., 2023, PASJ, 75, 1324

Sukhbold T., Ertl T., Woosley S. E., Brown J. M., Janka H. T., 2016, ApJ, 821, 38

Takahashi I., et al., 2009, ApJ, 701, 377

Takahashi T., et al., 2018, Journal of Astronomical Telescopes, Instruments, and Systems, 4, 021402

Tamura N., Ohta K., 2004, MNRAS, 355, 617

Tateishi D., Katsuda S., Terada Y., Acero F., Yoshida T., Fujimoto S.-i., Sano H., 2021, ApJ, 923, 187

Timmerman R., van Weeren R. J., McDonald M., Ignesti A., McNamara B. R., Hlavacek-Larrondo J., Röttgering H. J. A., 2021, A&A, 646, A38

Tsuru T. G., Awaki H., Koyama K., Ptak A., 1997, PASJ, 49, 619

Tsuru T. G., et al., 2007, PASJ, 59, 269

Tucker W. H., 2019, Mechanisms for the Production and Absorption of Cosmic X-Rays. Institute of Physics Publishing, pp 3.1–3.44, doi:10.1088/2514-3433/ab43dcch3

Turner M. J. L., et al., 2001, A&A, 365, L27

Ueda M., Sugiyama H., Kobayashi S. B., Fukushima K., Yamasaki N. Y., Sato K., Matsushita K., 2022, PASJ, 74, 1396

Urban O., Werner N., Allen S. W., Simionescu A., Mantz A., 2017, MNRAS, 470, 4583

Verner D. A., Ferland G. J., Korista K. T., Yakovlev D. G., 1996, ApJ, 465, 487

Webbink R. F., 1984, ApJ, 277, 355

Weisskopf M. C., Brinkman B., Canizares C., Garmire G., Murray S., Van Speybroeck L. P., 2002, PASP, 114, 1

Werner N., Mernier F., 2020, Hot Atmospheres of Galaxies, Groups, and Clusters of Galaxies. Springer International Publishing, pp 279–310, doi:10.1007/978-3-030-38509-5_10

Werner N., Durret F., Ohashi T., Schindler S., Wiersma R. P. C., 2008, SSRv, 134, 337

Werner N., Urban O., Simionescu A., Allen S. W., 2013, Nature, 502, 656

Werner N., McNamara B. R., Churazov E., Scannapieco E., 2019, SSRv, 215, 5

Whelan J., Iben Icko J., 1973, ApJ, 186, 1007

Willingale R., Starling R. L. C., Beardmore A. P., Tanvir N. R., O'Brien P. T., 2013, MNRAS, 431, 394

Woosley S. E., Heger A., Weaver T. A., 2002, Reviews of Modern Physics, 74, 1015

XRISM Science Team 2020, arXiv e-prints, p. arXiv:2003.04962

Yamaguchi H., et al., 2015, ApJL, 801, L31

Yamasaki N. Y., Sato K., Mitsuishi I., Ohashi T., 2009, PASJ, 61, S291

Yang H., Zhang S., Ji L., 2020, ApJ, 894, 22

Yoshino T., et al., 2009, PASJ, 61, 805

Zhang D., 2018, Galaxies, 6, 114

Zhang S., Wang Q. D., Ji L., Smith R. K., Foster A. R., Zhou X., 2014, ApJ, 794, 61

Zhang S., Wang Q. D., Foster A. R., Sun W., Li Z., Ji L., 2019, ApJ, 885, 157

de Plaa J., et al., 2006, A&A, 452, 397

de Plaa J., Werner N., Bleeker J. A. M., Vink J., Kaastra J. S., Méndez M., 2007, A&A, 465, 345

de Plaa J., et al., 2017, A&A, 607, A98

deBoer R. J., et al., 2017, Reviews of Modern Physics, 89, 035007

den Herder J. W., et al., 2001, A&A, 365, L7

List of Publications

[1] **K. Fukushima**, H. Yamaguchi, P. O. Slane, S. Park, S. Katsuda, H. Sano, L. A. Lopez, P. P. Plucinsky, S. B. Kobayashi, and K. Matsushita, "Element Stratification in the Middle-aged SN Ia Remnant G344.7–0.1", 2020, ApJ, 897, 62

[2] **K. Fukushima**, S. B. Kobayashi, and K. Matsushita, "Chemical enrichment in the cool core of the Centaurus cluster of galaxies", 2022, MNRAS, 514, 4222

[3] M. Ueda, H. Sugiyama, S. B. Kobayashi, **K. Fukushima**, N. Y. Yamasaki, K. Sato, and K. Matsushita, "The soft X-ray background with Suzaku. I. Milky Way halo", 2022, PASJ, 74, 1396

[4] **K. Fukushima**, S. B. Kobayashi, and K. Matsushita, "O, Ne, Mg, and Fe Abundances in Hot X-ray- emitting Halos of Galaxy Clusters, Groups, and Giant Early-type Galaxies with XMM-Newton RGS Spectroscopy", 2023, ApJ, 953, 112

[5] H. Sugiyama, M. Ueda, **K. Fukushima**, S. B. Kobayashi, N. Y. Yamasaki, K. Sato, and K. Matsushita, "The soft X-ray background with Suzaku. II. Supervirial temperature bubbles?", 2023, PASJ, 75, 1324

[6] **K. Fukushima**, K. Tanaka, M. Ueda, N. Y. Yamasaki, S. B. Kobayashi, and K. Matsushita, "Interpreting the thermal plasma contents in the Orion-Eridanus superbubble with joint Suzaku and HaloSat analysis", PASJ submitted

[7] **K. Fukushima**, S. B. Kobayashi, and K. Matsushita, "Revisiting the abundance pattern and charge-exchange emission in the M82 centre", A&A submitted

Curriculum Vitae

I obtained my Bachelor's degree in science at Tokyo University of Science (TUS) in 2019. In my Bachelor's thesis, I studied the nucleosynthesis of SNe Ia using X-ray observational data with *Suzaku*, especially focusing on the centroid energy of Fe K-shell emission lines. Prof. Dr. Kyoko Matsushita and Dr. Shogo Benjamin Kobayashi supervised the overall conduct of my study. At the same time, I also studied the Galactic SN remnant G344.7–0.1 and published the paper [1] in 2020, where Prof. Dr. Hiroya Yamaguchi in the University of Tokyo and ISAS/JAXA and Prof. Dr. Satoru Katsuda in Saitama University gave thorough guidance. After graduation, I stayed at TUS to enrol in a Master's programme and wrote my thesis about the chemical enrichment in the Centaurus cluster, which culminated in the paper [2] in 2022. I received my Master's degree in Science in 2021; and thenceforward, I started my PhD course at TUS. In my PhD research, I focused on the RGS analysis of the ISM and ICM, which led to the paper [4] in 2023 and the main result of this dissertation. At the same time, I collaborated on the research of X-ray foreground emissions in our Milky Way (the papers [3] and [5] in 2022 and 2023, respectively). In relation to the link of the ISM and ICM, I am preparing to publish papers [6] and [7] focusing on the Milky Way superbubble and the M 82 outflow, respectively. During the Master's and PhD courses, I had the chance to present my work at several international conferences, in Boston (USA), Tokyo (Japan, online), Saitama (Japan), Barcelona (Spain), and Athens (Greece); and at many domestic workshops.

Acknowledgements

I would like to present compliments to Prof. Dr. K. Matsushita and to appreciate her continuous support. I shall be grateful to Dr. S. B. Kobayashi for his fruitful discussions and continuous cooperation. They led and encouraged me over my five-year course of graduate school. I thank all present members of our laboratory: Mr. Y. Aoyama, Mr. S. Sekido, Ms. K. Kudo, Mr. Y. Shimatani Mr. K. Suda, and Mr. K. Sugawara; as well as the past members: Prof. Dr. K. Sato, Mr. M. Ueda, Mr. S. Hirai, Ms. Y. Nakagawa, Mr. M. Tagashira, Mr. D. Akimoto, Mr. H. Sugiyama, Mr. Y. Yamamoto, Ms. R. Yoneyama, Ms. H. Ikegame, Mr. M. Kajiyama, Mr. S. W. Kinoshita, Mr. Y. Nakagawa, Mr. H. Obara (Matsumoto), and Mr. Y. Yagi. The help and cooperation of all co-authors in my research should be recognized with praise.

I deem it an honour to have been supported by the Japan Society for the Promotion of Science through Grants-in-Aid for Scientific Research grant Nos. 21J21541 and 22KJ2797. The *Chandra* data used in this work are publicly available from the *Chandra* X-ray Center (https://cda.harvard.edu/chaser/). This work is based on observations obtained with *XMM-Newton*, an ESA science mission with instruments and contributions directly funded by ESA Member States and NASA of the USA. The *XMM-Newton* Science Archive (https://nxsa.esac.esa.int/nxsa-web/) storages and distributes the RGS data analysed in this work. All figures in this thesis, excluding Figs. 1, 4, 5, 6, and 8, were generated using VEUSZ (https://veusz.github.io/) or PYTHON (https://www.python.org/). The entire manuscript of this dissertation was typeset using the LaTeX template prepared by Dr. S.B.K.

Here, I would like to conclude acknowledgement by expressing the special gratitude for the aid I have received from my family, who are the greatest supporters of a boy having looked up at the starlit sky from the early days.